Correlation between homogenisation parameters and property evolution of AA3104 CBS after hot finish rolling

Prepared by:

Khethisa Lebakeng

LBKKHE001

Centre for Materials Engineering

Department of Mechanical Engineering

University of Cape Town

Supervisor:

Dr Sarah George

February 2025

Submitted to the Centre for Materials Engineering, Department of Mechanical Engineering at the University of Cape Town in partial fulfilment of the academic requirements for a Masters of Science degree in Materials Engineering

Key Words: Homogenisation, AA3104, CBS, Dispersoids

Abstract

AA3104 can-body stock (CBS) is produced through a series of thermomechanical processing stages, including direct chill (DC) casting, homogenisation, hot rough rolling, hot finish rolling, and cold rolling. Homogenisation is an important phase that controls the growth of intermetallic particles (IMPs) and dispersoids, affecting mechanical performance and texture evolution in following rolling stages. This study investigates the impact of different homogenisation procedures on the microstructure and mechanical properties of AA3104 during lab-scale hot rough rolling and plane strain compression (PSC) testing, which simulates hot finish rolling.

Industry supplied DC-cast AA3104 ingot material was exposed to various homogenisation procedures at temperatures ranging from 500°C to 610°C to produce differences in IMP morphology and dispersoid dispersion within the structures. The homogenised samples were subjected to lab-scale hot rough rolling to achieve strain and IMP breakdown in line with that of industrial rough rolling. PSC testing on a Gleeble 3800 was utilised to simulate industrial hot finish rolling conditions. The microstructural evolution was investigated using light microscopy, scanning electron microscopy (SEM) in conjunction with energy-dispersive spectroscopy (EDS) and electron backscatter diffraction (EBSD) for grain and texture characterisation.

The findings show that homogenisation temperature has a significant influence on IMP fragmentation, dispersoid refinement, which then has a marked effect on recrystallisation behaviour and texture development. The findings show that the 600°C/520°C condition resulted in coarse dispersoids (127 nm) with low number density (8.93 particles/µm²), the 560°C/520°C condition produced intermediate-sized dispersoids (104 nm, 19.85 particles/µm²), and the 520°C condition generated fine, closely spaced dispersoids (56 nm, 55.92 particles/µm²). The cube texture intensity was found to increase with dispersoid density, with the 520°C sample displaying the strongest cube texture (~9.04), followed by 560°C/520°C (~7.5) and 600°C/520°C (~4.8). the 560°C/520°C homogenisation resulted in the largest recrystallised grains. While the 520°C homogenisation contained the finest dispersoids, the EBSD maps showed a fully recrystallised structure with recrystallised grains being smaller than the 560°C/520°C homogenisation. This is attributed to a combination of insufficient pinning pressure to fully retard recrystallisation as well as IMP topology effects on particle stimulated nucleation (PSN) and the overall recrystallisation kinetics, resulting in a smaller grain size than anticipated. There was no recrystallisation in the as-cast protocol, demonstrating that the dispersoids play an essential role in recrystallisation. None of the high temperature homogenisation practices resulted in sufficiently fine dispersoids to retard recrystallisation.

These findings emphasise the significance of adjusting homogenisation parameters to alter microstructural features, such as IMPs and dispersoids for microstructural development, better hot rolling performance and final property. The findings do illustrate the importance of a more detailed interrogation of the role of these critical features in the rolling process. This should be achieved on a laboratory scale initially. The experimental protocol for this work used a fully lab scale simulation approach, which showed successful alignment with initial partial industrial samples.

The microstructures of the 560°C/520°C material were compared to samples where only the finish rolling was simulated (on industrially supplied transfer bar after industrial homogenisation and rough rolling). The grain size and cube texture intensity of the two approach showed similarities in grain size and cube texture intensities. This indicates an equivalent thermomechanical processing route to achieve these similar microstructures. This is a successful first step in the validation of a full through process simulation of processing on a laboratory scale.

Plagiarism Declaration

1. "I know the meaning of plagiarism and declare that all the work in the document, save for that which is properly acknowledged, is my own. This thesis/dissertation has been submitted to the Turnitin module (or equivalent similarity and originality checking software) and I confirm that my supervisor has seen my report and any concerns revealed by such have been resolved with my supervisor."

2. Each significant contribution to, and quotation in, this project from the work, or works of other people has been attributed and has cited and referenced.

3. This project is my own work.

4. I have not allowed, and will not allow anyone to copy my work with the intention of passing it off as his or her own work.

5. I acknowledge that copying someone else's assignment or project, or part of it, is wrong, and declare that this is my own work.

Khethisa Eric Lebakeng

Signature:

Signed by candidate

Date:

17/02/2025

Acknowledgements

Foremost, I would like to express my sincere gratitude to my supervisor Dr Sarah George for the continued support and guide in my masters research, their patience, their motivation, enthusiasm and their impeccable knowledge. They were a mother to me when I approached them with my life problems and will forever cherish that. I really would not ask for any other supervisor for my master thesis.

I would like to show great acknowledgement to:

Hulamin with their financial support and supply of the samples.

Centre for Material Engineering and the staff (Penny Louw, Maxwell Vos, Ernesto Ismail and Mike Shirran). With their help, I was able to learn to operate numerous machines, interpret and analyse date which helped me massively with my research.

Mintek, specifically Joseph Moema and Mbavhalelo Maumela, for permitting and guiding us when using their rolling machines and furnaces.

UCT Electron Microscope Unit, naming Soraya Von Willingh in particular. Their assistance with SEM, SEM-EDS and EBSD is highly appreciated.

Nkopo Chaole and Tshepo Maluleka for their academic support through the masters degree.

The Department of Mechanical Engineering workshop for their technical support.

Family for their all-round support (Ntate Nts'ala, 'M'e 'Makhethisa, Abuti Tokelo, the Lebakeng family, close friends and Ausi Precious)

Table of Contents

List of abbreviations

UCT	University of Cape Town
CME	Centre for Materials Engineering
CBS	Can body stock
DC	Direct chill
IMPs	Intermetallic particles
PSN	Particle stimulated nucleation
SEM	Scanning Electron Microscopy
EDS	Energy-dispersive spectroscopy
EBSD	Electron backscatter diffraction
TMP	Thermomechanical processing
D&I	Drawing and wall ironing
PSC	Plane strain compression
TEM	Transmission Electron Microscopy
UTS	Ultimate tensile strength
YS	Yield strength
PZ	Zener pinning pressure
PD	Driving pressure for recrystallization
SDAS	Secondary dendrite arm spacing
SFE	Stacking fault energy
NPL	National Physical Laboratory
DSI	Dynamic Systems Inc.
ODFs	Orientation distribution functions
HAGBs	High angle grain boundaries
LAGBs	Low angle grain boundaries

List of Figures

List of Tables

1. Introduction

1.1 Background and motivation

AA3104 can body stock (CBS) is commonly used for the bodies of beverage cans, because of the combination of formability and strength properties. The production of CBS sheet involves multiple steps, including direct chill (DC) casting, followed by homogenisation for the reduction of segregation and the critical phase transformations and particle nucleation and growth processes. The homogenised slab then undergoes a series of hot deformation passes to reduce the slab thickness. This can be divided into two processes, namely, the hot rough rolling process followed by the finish rolling process. Thereafter the sheet is coiled and transferred to cold rolling to final gauge. The sequential roll passes of hot rolling occur at reducing temperatures. These rolling processes are managed using a rolling schedule that specifies, including but is not limited to, the number of passes of the slab through the rolling mill, the strain per pass, the strain rate, the roll speed, and the rolling temperatures. Close control of these complex process parameters during rolling is required to achieve the desired microstructure and property demands of the final sheet. The thermomechanical processing (TMP) history determines the final microstructure, which ultimately determines the final mechanical properties of the rolled sheet. TMP is a combination of plastic deformation, which results in strain accumulation, and the annealing mechanisms, which include recovery, recrystallization, and grain growth. The plastic strain and annealing occur simultaneous at high temperatures, and are the controlling factors driving microstructure evolution, which ultimately determines the sheet properties of the AA3104 CBS [1].

In the CBS production, alloy and processing conditions are chosen to provide sufficient strength, low earing, and galling resistance. This is to permit the fabrication of a can body by drawing and wall ironing (D&I) processes as well as sufficient strength retention following paint baking to ensure that the finished can is sufficiently strong [2]. Earing in aluminium beverage can manufacturing occurs during the deep drawing process when the material does not stretch evenly, leading to the formation of raised edges or 'ears' on the rim of the formed can. The extent of earing is related to the amount of cube texture created and retained throughout processing [3]. The strength is the result of contributions from several strengthening mechanisms, such as solid solution strengthening, particle strengthening and work hardening retained from the final cold rolling stage of sheet production. The microstructural features that form during homogenisation of a DC cast AA3104 ingot are critical to the microstructure development throughout the rolling processes. These features include the phase transformations and evolution of the constituent intermetallic particles (IMPs) that form during the solidification of eutectic phases during DC casting. These

evolutions included the transformation of the dominant β-Al_6(Mn,Fe) particles into the harder α-Al_{12}(Mn,Fe)$_3$Si particles, which facilitate a breaking up and a reduction in size of the constituent particles. Additionally, the homogenisation process facilitates the formation of dispersoids within the grain centres. The size and distribution of these dispersoids is linked with the motion of dislocations through the structure and Zener drag, which is critical for the dominance of recovery or recrystallisation during later processing [4].

Notwithstanding the importance of the fundamental understanding of the link between homogenisation and the underlying microstructure evolution on property development, the ability to simulate the complex series of steps that are representative of industrial processing on a small, laboratory scale is an essential competency to investigate process parameters for hot rolling. Typically, expensive and disruptive industrial trials would be performed to investigate critical processing parameter changes and their downstream effects, but there is a need for a lab scale technical approach that successfully simulates the full process. A lab scale protocol would need to be validated through comparisons at critical points in the process. Lab scale simulation of finish rolling is typically performed using plane strain compression (PSC) testing, but this does not include the incorporation of the rough rolling stage as well. Therefore, the full protocol should include PSC as the final step but must address both homogenisation and hot rough rolling as well.

The aim of this research is to use a laboratory-scale experimental investigation to simulate the full process route for producing hot rolled sheet for CBS. The efficacy of the lab-scale simulation will be measured through investigating the effect of three distinct homogenisation practices, and the resultant IMP and dispersoid structures that form, on the mechanical properties during finish rolling of AA3104 CBS. This is achieved by imposing varied homogenisation practices on industry supplied DC cast AA3104 ingot material in a temperature range of 500°C - 610°C. The hot rough rolling stage and the finish rolling stage will occur on a lab scale and the parameters will be equivalent to industry standards. The microstructure evolution and property development will be tracked, and a final validation will be achieved through flow stress analysis and a texture evaluation in the final material.

1.2 Objectives of research

The objectives of the study are to:

- Impose three homogenisation practices that represent the extremes of the standard industrial approaches in order to create samples with varied IMP and dispersoid structures in the material prior to hot rough rolling.

- Perform lab-scale hot rough rolling on homogenised material, followed by lab-scale plain strain compression (PSC) testing to simulate hot finish rolling.
- Investigate the mechanical response of the material during the lab-scale simulation of hot finish rolling using PSC and correlate the final microstructure with the underlying microstructural features developed during the distinct homogenisation processes.

1.3 Scope and limitations

The study focuses on how homogenisation techniques affect the distribution of IMPs and dispersoids in AA3104 aluminium alloy. The investigation is limited to samples obtained in the DC cast condition from industry. The study used light microscopy, SEM-EDS analysis, and high temperature plane strain compression testing. The temperature and time of homogenisation are studied, as well as their effects on IMPs and dispersoids.

Due to time constraints, the study was limited to four starting conditions. The results are particular to AA3104 and may not apply to other aluminium alloys. Additionally, the opportunity to repeat the trial was limited by time and thus no repeat experiments were done. Therefore, the results speak to individual batches of homogenisations and rough rolling. Multiple samples were tested for finish rolling, all extracted from the single batch for each condition.

The study did not include Transmission Electron Microscopy (TEM) analysis, owing to scheduling constraints. This limitation implies that some finer features, particularly those at the nanoscale may not have been fully resolved, potentially affecting the depth of information about particle-phase interactions and property evolution during homogenisation and rolling.

Future studies using TEM analysis could expand on these findings by addressing these nanoscale events, resulting in a more complete knowledge of the alloy's microstructural history.

1.4 Plan of development

This study document begins with a review of other authors' works on the AA3104 aluminium alloy, the effects of homogenisation, and plain strain compression. It next details the experimental methodologies, which comprise three AA3104 samples undergoing different homogenisation protocols before being hot-rolled and annealed. SEM-EDS is used to analyse microstructure and composition, with a focus on IMPs and dispersoids. The findings are presented in sections focused on the evolution of dispersoids' size and distribution, followed by connections with mechanical

properties. The findings will be evaluated by comparing them to industry results before concluding by relating homogenisation factors to property evolution and making recommendations for process optimisation in manufacturing.

2. Literature Review

2.1 Material

2.1.1 Aluminium alloy – AA3104

Pure aluminium is not suitable for applications requiring resistance to deformation and fracture owing to its high ductility and low strength. Pure aluminium typically exhibits elongation at break values around 40% or higher, indicating its ability to undergo significant plastic deformation before fracture [5] while the tensile strength of commercially pure aluminium is approximately 90 MPa [6]. Other elements are added to pure aluminium to create an alloy with improved strength. Alloying is often used to increase strength, hardness, and resistance to wear, creep, stress relaxation, or fatigue [7]. The impacts on these properties vary depending on the alloying elements and combinations utilised. They are related to their alloy phase diagrams as well as the microstructures and substructures created because of solidification, thermomechanical history, heat treatment, and/or cold working.

The classification of aluminium follows a four-digit numbering system (1xxx to 8xxx) based on the alloyed elements as shown in Table 1 below. Copper (Cu), magnesium (Mg), manganese (Mn), silicon (Si), and zinc (Zn) are frequently added substances to form the aluminium alloys. These alloy compositions have an impact on aesthetics and fabrication as they enhance strength, workability, corrosion resistance, electrical conductivity, and density of the pure aluminium [8].

Table 1. Main alloying elements in the wrought alloy designation system [7]

Alloy	**Main Alloying element**
1xxx	Mostly pure aluminium; no major alloying additions
2xxx	Copper
3xxx	Manganese
4xxx	Silicon
5xxx	Magnesium
6xxx	Magnesium and Silicon
7xxx	Zinc
8xxx	Other elements (e.g., iron or tin)
9xxx	Unassigned

AA3104 is a 3xxx series alloy, with Mn as the major alloying element, as seen in Table 1. The 3xxx series alloys can be strain hardened, have excellent corrosion resistance, and can be easily welded, brazed, and soldered. These alloys are non-heat treatable, meaning they gain strength by solid solution or dispersion hardening and are further strengthened by strain hardening [9].

The weight percent of each alloying element varies for every material even if they are from the same alloy series. For the AA3104 alloy, the composition of the elements is shown in Table 2.

Table 2. AA3104 Element composition [10]

Element	Al	Cu	Ga	Fe	Mg	Mn	Si	Ti	V	Zn
wt% in AA3104	95-98.4	0.05-0.25	≤0.05	≤0.8	0.8-1.3	0.8-1.4	≤0.6	≤0.1	≤0.05	≤0.25

The alloying element should have significant solubility at higher temperatures and a decrease in solubility as the temperature is lowered in order to offer solid solution strengthening.

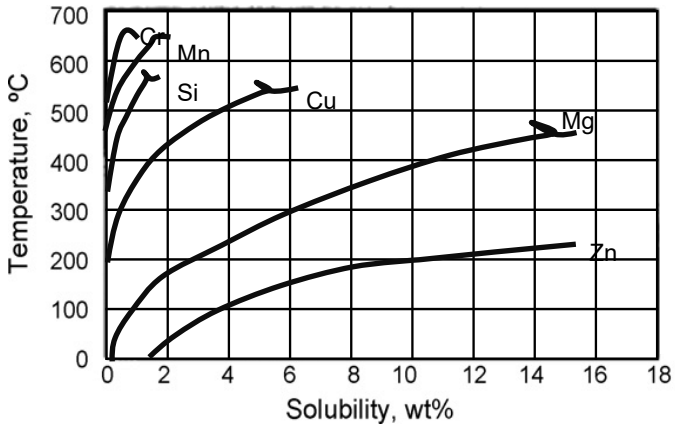

Figure 2.1. The solid solubility of different alloying elements in aluminium as a function. Image adapted from [11].

2.1.2 Microstructural features in AA3104

An alloy that is strengthened by dispersion has a continuous phase, which is called the matrix. In the case of AA3104 there is an aluminium matrix. The alloying elements will form a second phase when the solubility of the alloying elements within the matrix is exceeded. A grain boundary separating the two phases is therefore created resulting in a strengthened material because of the interference with the slip of dislocations [12]. The second phase exists in small and numerous amounts within the matrix and can be in the form of intermetallic compounds, dispersoid and/or precipitates. These second phase particles are dispersed within the matrix and play a role in microstructure evolution and strengthening. A second phase that has its composition, crystal structure, and properties resulting from compounds formed by two or more elements and forms during the initial ingot solidification process is referred to as a constituent intermetallic compound or phase [12]. Other second phase particles form through a nucleation and growth process during homogenisation and downstream processing owing to diffusion. While these particles may have

the same phase constitution, they are not constituent particles. They nucleate and grow within the matrix and are referred to as dispersoids owing to their shape, size and distribution.

During casting of an aluminium ingot in the 3xxx series, the constituent IMPs are formed, which are the eutectic phases formed during solidification. During homogenisation these IMPs undergo various diffusion-based changes and dispersoids form within the structure [13]. The IMPs and the dispersoids are critical microstructural features that affect the microstructure evolution and property development during downstream processing.

2.1.2.1 Intermetallic particles

The composition of the alloy and the rate of solidification determine the relative volume fractions of the intermetallic phases. The two common intermetallic phases found in the 3xxx series is the β-Al_6(Fe,Mn) and α-Al(Fe,Mn)Si [14]. The orthorhombic β-Al_6(Fe,Mn) phase forms more readily than the cubic α-Al(Fe,Mn,Si) phase due to faster solidification rates. The distribution, size and phase of the IMPs are guided by the solidification kinetics experienced in DC casting of the ingots [15]. During solidification, the IMPs show a eutectic second phase morphology, which solidifies around the aluminium matrix cells. When the ingot is exposed to homogenisation heat treatment, if the Si content in the alloy is high enough, the β-Al_6(Fe,Mn) phase may change to the bcc α-Al(Fe,Mn)Si phase during homogenisation heat treatments, as shown in Figure 2.2. The morphological changes and size decrease of the IMPs associated with homogenisation practices is facilitated through the particle break-up due to duplex phase transformations, (as shown in Figure 2.2), where the α-Al(Fe,Mn)Si particles form through diffusion based transformations on existing β-Al_6(Mn,Fe) particles [16]. During homogenisation, the precipitation of α-Al(Fe,Mn)Si dispersoids begins at roughly 340°C [17]. Li [18] determined that the α-Al(Fe,Mn)Si dispersoids were partially coherent with the Al matrix and thermally stable at high temperatures.

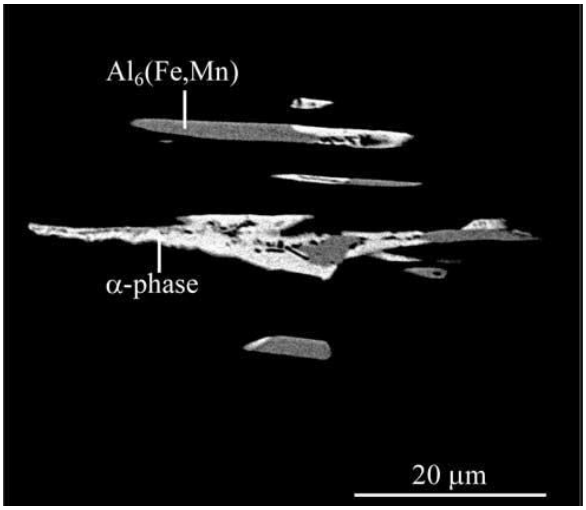

Figure 2.2. A BSE SEM image of a polished specimen made from alloy heat-treated for 1 hr at 500°C. The α-Al-(Fe,Mn)-Si phase is brighter than $Al_6(Fe,Mn)$ due to its higher average atomic number. The α-phase has grown through particles from the particle-matrix interfaces, producing duplex particles [19].

The transition from β to α is a desirable transformation since it maximises the resistance of the material to galling during the drawing and ironing process. On the other hand, an excessive volume percentage of the harder α-Al(Fe,Mn)Si phase could cause die surfaces to wear down more quickly making a balanced volume fraction preferable [20].

2.1.2.2 Dispersoids

When aluminium combines with other alloying elements, it forms a second phase, which has little or no solubility with aluminium. Small precipitates called dispersoids form because of diffusion of solute atoms during homogenisation heat treatments of the as-cast ingot. These dispersoids act to block grain boundary migration through the Zener drag mechanism, in contrast to the IMPs that aid in recrystallisation by particle stimulated nucleation [20]. The type, size, and distribution of dispersoids formed during homogenisation significantly affect the deformation behaviour, recrystallisation characteristics, and mechanical properties of non-heat-treatable 3xxx series (Al–Mn–Fe–Si) aluminium alloys [18]. Li et al. used TEM to quantify the evolution of the size, number density and volume fraction of dispersoids in a 3xxx alloy and results indicated that the number density of dispersoids that precipitated during the heat-up stage of homogenisation can reach up to $10^{21} m^{-3}$ [18]. However, this density decreased as the temperature rose. Lodgaard and Ryum [21] showed that at temperatures greater than 550°C, dispersoids begin to dissolve as Mn solubility increases. This was illustrated through the measure of conductivity. Figure 2.3 shows the line for C-A ,which represents an aluminium alloy containing Mn-rich dispersoids, and shows the point where conductivity decreases owing to dispersoid dissolution.

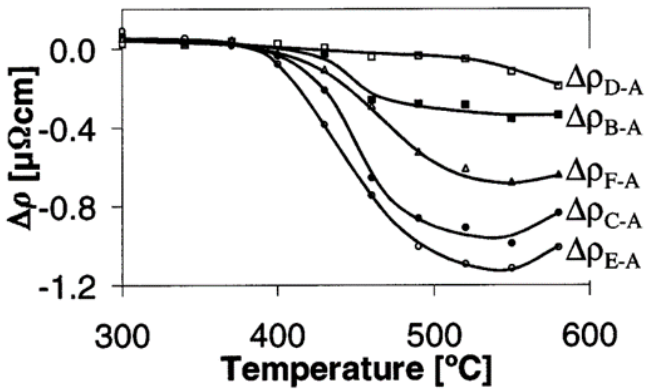

Figure 2.3. Electrical resistivity change in all the alloys. The change is only due to the precipitation and dissolution of dispersoid-forming elements [21].

Prolonged holding at temperatures between 450 – 600°C leads to the dissolution of most dispersoids as the solubility of Mn is increased at such temperatures [22]. Hsin-Wen Huang et al. [23] performed an EDS analysis that revealed that the dispersoids that primarily develop at low temperatures are $Al_6(Mn,Fe)$, which can dissolve in an aluminium matrix via the Ostwald ripening mechanism at higher temperatures, promoting the development of the α-$Al_x(Fe,Mn)_3Si_x$ dispersoids. Composition is also important for dispersoid evolution, as additions of Fe and Si lower the Mn solubility in the aluminium matrix, accelerating the precipitation of Mn-containing dispersoids. Si promotes the formation of dispersoids from the cubic α-$Al_x(Fe,Mn)_3Si_x$ phase, while Fe can replace Mn in both the Al_6Mn and α-$Al_x(Fe,Mn)_3Si_x$ phases [20].

2.1.3 Roles of main alloying elements

Manganese (Mn)

Mn is added to aluminium as it increases strength when in solid solution or as a finely precipitated intermetallic phase, as illustrated in Figure 2.4. However, solubility of Mn in aluminium is limited to 1.82wt% at the eutectic temperature [24]. This provides considerable gains in strengths at room temperature and especially at high temperatures [25]. The addition of Mn or its combinations with other transition elements can introduce a large number of thermally stable nano-sized dispersoids, such as α-$Al_x(Fe,Mn)_3Si_x$, β-$Al_6(Mn,Fe)$ or Al_6Mn in 3xxx alloys. Mn within the specified range ensures enough strength in the finished product after stoving. If Mn exceeds the upper limit, too many dispersoids form during the processing of the cast strip to re-roll gauge, preventing adequate recrystallization during the annealing steps and resulting in excessive earing in the finished product [2]. Apart from that, Mn in can body stock produces big, hard particles that are useful in die-cleaning during drawing operations. It also adds strength to the final gauge sheet by solution hardening and has beneficial corrosion resistance [26].

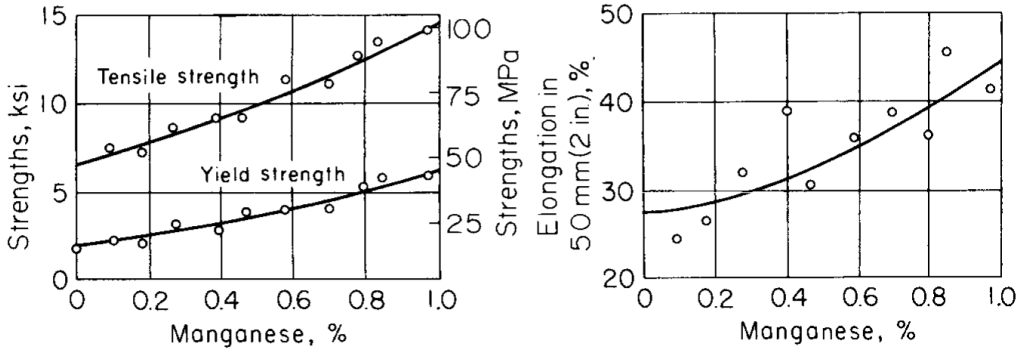

Figure 2.4. Effect of Mn on tensile properties of wrought 99.95% aluminium, 1.6-mm (O.064-in.) thick specimens, quenched in cold water from 565°C (1050 OF). (Courtesy of Alcoa Research Laboratories) [27].

Magnesium (Mg)

Mg_2Si particles are critical in the nucleation of alpha dispersoids during heat treatment of aluminium alloys. During non-equilibrium solidification, these particles are created as metastable eutectic phase that promotes the creation of α-Al(Mn,Fe)Si dispersoids [28] . Mg contributes to the total strength of the alloy by solid solution hardening and work hardening. The Mg addition into 3xxx alloys improves the strength due to the synergistic effect of solute and strain hardening [29]. The finished product will experience excessive work hardening during drawing and ironing and be more susceptible to scoring if the Mg content is too high. Mg deficiency results in inadequate strength in the finished product [2].

Silicon (Si)

It is anticipated that Mg_2Si intermetallic will form if the Si content rises over 0.3 wt%, hence reducing the amount of Mg that can be used to reinforce the material. For materials that are readily available on a commercial basis, the lower limit for Si is a practical restriction [2]. Si has the greatest influence on the microstructure due to the ability to create intermetallic compounds with AI, Fe, Mg, and Mn [30]. Mg_2Si and α-AI_{12}(Fe,Mn)Si are the two most common Si-containing precipitates. The α-precipitates are generated mostly following the solidification, during homogenisation and are facilitated by the transformation of β-particles by Si diffusion. As a result, the amount of Si has a large influence on the ratio of α- to β-particles [31].

Iron (Fe)

Fe decreases the solubility of Mn in 3xxx alloys as Fe and Mn can readily replace one another in α-Al(Mn,Fe)Si dispersoids [32]. Previous research [33] indicates that the Fe content has a considerable effect on the IMPs, dispersoids, and mechanical properties at both ambient and increased temperatures. The results demonstrate that, despite the presence of 0.1 wt% Fe, the main IMPs are α-Al(Mn,Fe)Si. When the Fe concentration rises to 0.3 wt% - 0.6 wt%, the main IMPs shift from α-Al(Mn,Fe)Si to Al_6(Mn Fe) on solidification. They will partially transform to the α-phase in the presence of Si during homogenisation. Alloys with 0.3 wt% Fe have the finest and greatest volume proportion of dispersoids.

Copper (Cu)

Cu serves as a strengthening agent via precipitation hardening mechanisms. Minor additions (0.2 to 0.3 wt% Cu) have been demonstrated to greatly increase the ultimate tensile strength (UTS) and yield strength (YS) of AA3104-H19 sheets [34]. The inclusion of Cu causes a finer microstructure, which improves mechanical properties. Interestingly, higher Cu content has been linked to improved corrosion resistance under specific conditions, this is due to the finer microstructure that occurs with higher Cu levels. This reduces the size and proportion of harmful ferrous intermetallic phases that can impair corrosion behaviour [35]. Cu increases strength and hardness, but it can also reduce ductility, especially when big ferrous particles are present in the alloy matrix. This brittleness can impact performance under tensile stress [36].

2.2 Fabrication of rolled sheet

The can body is made from a cold-rolled AA3104 sheet with a gauge of approximately 0.24-0.27 mm. The can body is formed through a standard forming technique known as drawing and ironing, which involves drawing the blank into a cup and then passing it through a series of dies to achieve the desired elongated cylindrical body configuration, with a side wall of reduced thickness relative to the bottom end [1]. The forming technique used in the manufacture of drawn-and-ironed can body stock demands a distinctive combination of alloy properties which include strength, yield strength, elongation, and earing among the list of properties. This is in addition to ensuring that the thickness of the can wall can withstand internal and exterior stresses when in operation. The acquisition of these properties is determined by the alloy composition and the processing conditions of the sheet. The process for the fabrication of the rolled sheet is illustrated in Figure 2.5.

The fabrication process starts with a direct chill (DC) cast ingot with a thickness of between 500mm and 750mm, at temperatures ranging from 660°C to 700°C. Following casting, the slabs are scalped to remove the surface of the cast slab to remove impurities and defects. Scalping is performed at ambient temperatures.

Following scalping, the slabs are homogenised, which is critical for the reduction of segregation and the formation of a desirable IMP and dispersoid structure. The slabs are heated to temperatures ranging from 520°C to 600°C during homogenisation. The ingot undergoes a homogenisation process for periods of 2 to 12 hours. Following that, the slab thickness is substantially reduced through rolling in the break-down rolling step, also known as rough rolling, with rolling temperatures ranging from 420°C to 520°C. This entails a large degree of deformation over several passes to a gauge of approximately 25 mm [37].

The finish rolling process is the final stage of hot rolling. The transfer bar is further elongated and its thickness reduced to approximately 2.5 – 2 mm, typically at temperatures from 360°C to 300°C. The sheet is coiled and then ready for cold rolling. The cold rolling stage is crucial for achieving the desired thickness, strength and surface finish for can body stock material. The aluminium is cold rolled at temperatures between room temperature and 180°C [37].

Finally, some aluminium alloys may be heat treated to improve their mechanical properties. Specific heat treatment temperatures might range from 150°C to 500°C depending on the alloy and desired qualities. Following the completion of these stages, the metal can be utilized to manufacture aluminium cans for beverages, ensuring that the material fulfils the required standards and requirements for can manufacturing.

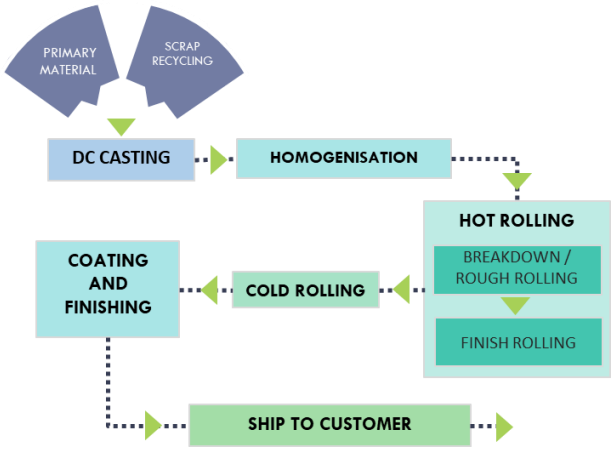

Figure 2.5. Schematic of production of rolled sheet.

2.3 Zener drag and Particle Stimulated Nucleation (PSN)

Zener drag is a retarding force caused by primary and newly formed particles that slow down grain boundary motion during recrystallisation [38]. Particles can hinder grain boundary motion, slow down recrystallisation and increase average grain size after recrystallisation. However, the amplitude of the retarding force is determined by the particle concentration and size. In materials with a high density of second-phase particles, IMPs and dispersoids, the retarding force is often higher [4]. This is due to fine and numerous (measured in nanometres) dispersoids formed during homogenisation pinning grain boundaries and dislocations hence inhibiting their movement, making nucleation and growth of recrystallised grains difficult. The distribution of dispersoids within the matrix affects the Zener drag pressure. Eivani et al. [39] demonstrated that two AA7xxx alloy structures with identical parameters but differing nanoscale dispersed particle size distributions produce different Zener drag pressures. The structure with a distribution of dispersoids with a

variation of sizes (inhomogeneous sizes) enhances the Zener drag pressure more effectively than structure with the same distribution of uniformly sized dispersoids.

During thermomechanical processing, the dispersoids are crucial because they apply a pressure known as the Zener pinning pressure (*PZ*) on grain and subgrain borders [40]. The driving pressure for recrystallization (*PD)* is in direct competition with this PZ pressure. When *PZ* < *PD*, recrystallization will take place, which is represented as:

$$\frac{3V_f\gamma_H}{2r} < \frac{3\gamma_S}{D} \qquad (1)$$

where V_f is the particle volume fraction, r is the radius of the particle, and γ_H is the high angle grain boundary energy, which for Al 0.324 mJ m^{-2} [41]. The driving pressure PD in a well recovered structure, is dependent on the subgrain boundary energy γ_S and mean subgrain diameter D, and assumes a uniform stored energy in the grain, γ_S can be estimated as ≈0.2 of the high angle grain boundary energy [41]. According to this calculation, there are areas toward the grain centre where the pinning effect of dispersoids is insufficient to stop boundary migration at the beginning of the annealing phase following cold rolling. Therefore, the absence of appropriate nucleation sites for new grains can be explained by the finding that recrystallization is not typically initiated in such places.

Fewer recrystallisation nuclei corresponds to larger recrystallised grain sizes. Doherty and Martin [42] demonstrated that precipitate dispersions, coarse dispersion and broad scattered precipitates, can accelerate recrystallisation but the fine dispersion of small, close precipitates can slow down recrystallisation. It is during annealing after hot and cold rolling that the large (≳1 μm) second-phase particles can promote recrystallisation by particle stimulated nucleation (PSN) [43]. PSN is a mechanism whereby large second-phase particles generate deformation zones, localized areas of high dislocation density and lattice rotations, during plastic deformation. These deformation zones serve as favourable sites for the nucleation of newly recrystallised grains with orientations distinct from those of the surrounding deformed matrix.

2.4 As-cast microstructure

In AA3104 aluminium alloy formed by traditional direct chill (DC) casting at an estimated solidification rate of 1°C/s, only 25-30 wt% of the Mn is present in the eutectics in the as-cast condition, while 70-75 wt% remains in a supersaturated metastable solid solution [44]. Si in the alloy creates three intermetallic phases: α-$Al_{12}(Mn,Fe)_3Si$, α-$Al_{20}Fe_5Si_2$, and $Al_6(Mn,Fe)$. The majority

(approximately 85%) of the IMPs constitute the orthorhombic $Al_6(Mn,Fe)$ phase, while the remaining 15% are cubic α and α' phases, which predominantly consist of α-$Al_{12}(Mn,Fe)_3Si$ [44].

The as-cast microstructure of 3xxx alloy shows a solidification cell structure, with intermetallic phases such $Al_6(Mn,Fe)$ and α-$Al_{12}(Mn,Fe)_3Si$ separated at cell borders. These intermetallics are important because they act as nucleation sites for recrystallization after subsequent annealing. The solidification kinetics dictate the as-cast structure's distinguishing properties, which include solidification cell size, degree of solute supersaturation, and shape of the border intermetallics [45].

Faster cooling rates during solidification produce finer microstructural characteristics, such as smaller cell sizes. DC-cast material has an average cell size of 50 µm. Furthermore, Chan and Das [44] explain that the solute supersaturation of Mn in solid solution increases with cooling rate, ranging between 0.75 wt% and 0.90 wt% Mn, depending on the solidification circumstances. There is an inverse relationship between cooling rate and volume fraction of solute partitioned to intermetallic phases, with Mn-rich intermetallics dropping to as low as 0.50 wt% in slowly solidified DC-cast material.

Increased cooling rates reduce the volume percentage of boundary intermetallic phases while simultaneously refining their shape, resulting in thinner and more distinct eutectic structures [45]. This refinement has a direct effect on the evolution of IMPs during subsequent homogenisation, assisting in their transformation and redistribution.

The starting as-cast microstructure consists of primary aluminium dendrites and a small amount of interdendritic eutectic. Segregation in an as-cast structure is observed to occur at two levels: (i) macrosegregation from the surface to the centre of the billet, over the length scale of hundreds of millimetres and (ii) microsegregation over the length scale of the average secondary dendrite arm spacing (SDAS), typically in micrometres. The interdendritic primary eutectic phases are a mixture of $Al_6(Mn,Fe)$ and α-$Al_{12}(Mn,Fe)_3Si$ in the form of rod- or plate-like particles with a size of ~ 1-5 µm referred to as constituent particles [22]. The primary aluminium dendrites are typically supersaturated, particularly in Mn, which has a low diffusivity in aluminium.

A study by Li and Arnberg [46] on the solidification structure of an AA3103 (1.02 wt% Mn, 0.54 wt% Fe, 0.05 wt% Si, 0.002 wt% Cu) showed an average SDAS of approximately 50 µm and had solidification structure and concentration profiles of Mn and Fe, as shown in Figure 2.6. Figure 2.6 (a) illustrates the plate-like eutectic primary particles dispersed across grain boundaries and in interdendritic areas, whereas Figure 2.6 (b) illustrates the concentration profiles of the alloying elements Mn and Fe over the dendrite arm displayed. Much of the Mn in the alloy remains in the solid solution after solidification, whereas the concentration of Fe in the solid solution is quite low. Li and Arnberg showed that for DC-cast AA3103 presented with segregation of the Mn in the

dendrite arms. TEM diffraction patterns and microprobe composition measurements revealed that the parent particles were orthorhombic $Al_6(Mn,Fe)$ phase.

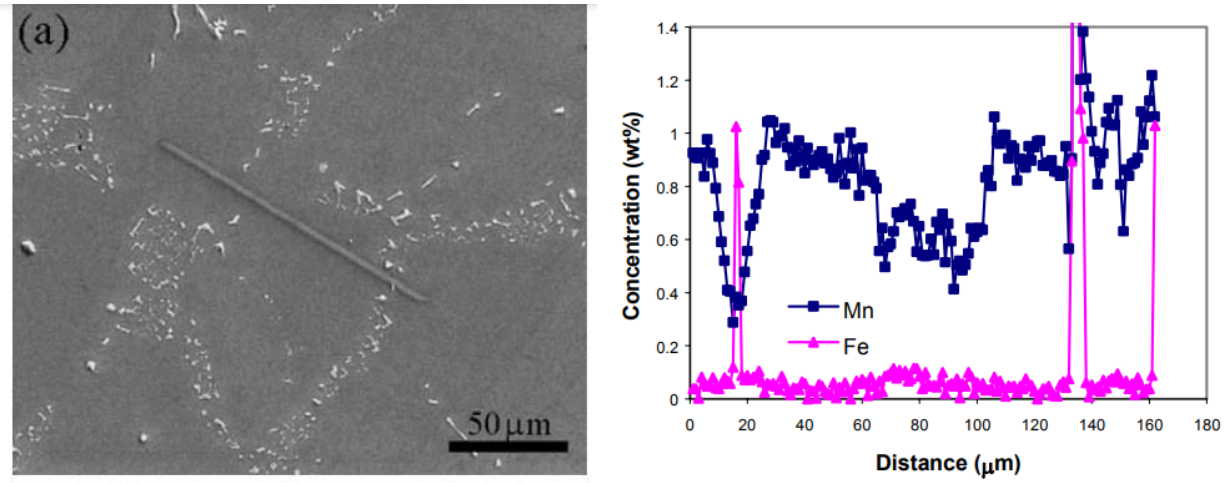

Figure 2.6. Solidification structure of AA3103 alloy (a) and concentration profiles of Mn and Fe in the dendrite along the track shown in (a) [46].

2.5 Homogenised microstructure

Most Mn atoms can be in solid solution in the aluminium matrix after non-equilibrium solidification during DC casting, producing a supersaturated solid solution. The precipitation of dispersed particles during the homogenisation process breaks down this supersaturated solid solution. Thus, during homogenisation, it is crucial to regulate the amount of Mn atoms in the solid solution as well as the size, density, and dispersion of the precipitated particles [23]. The goal of the homogenisation heat treatment is to eliminate microsegregation and provide an optimum microstructure for processing. Two important microstructural changes occur during homogenisation; the first involves the growth and alteration of constituent particles. Their growth was thoroughly investigated using TEM by Ånes et al. [43], where the diffusional transfer of Si from the primary aluminium dendrites to the interdendritic area was responsible for the alterations in the constituent particles. Precipitation within the main aluminium dendrites is the second microstructural alteration that takes place in the as-cast material during homogenisation to achieve local equilibrium of the slow diffusers, Mn and Fe. This is the important driving force for precipitation of dispersoids. This happens through the nucleation, growth, and coarsening of tiny particles known as dispersoids that include Fe, Mn, and Si and typically have a diameter of between 50 and 200 nm. The degree of super-saturation in the primary aluminium dendrites is decreased because of this precipitation reaction. Diffusion of these dispersoids at the inter-dispersoid spacing scale (~100 nm) controls their growth and coarsening

[22]. Du et al. [47] mention that the composition and alloy chemistry affect the dispersoids' crystal structure and content. The dispersoids were found to be of the α-Al(Mn, Fe)Si phase in an experimental investigation of an AA3003 alloy. It was noted that the peak number density might surpass 1000 μm^{-3} and that the dispersoids could expand or coarsen to sizes of 100–200 nm [47].

Li and Arnberg [22] studied the morphology and crystal structure of dispersoids' precipitation during the heating of AA3003. The observed precipitation of very fine dispersoids with sizes of several nanometres when as-cast AA3003 was heated to 300°C. This indicated the initiation of decomposition of the supersaturated solid solution. They also observed that the precipitated dispersoids had a nearly equiaxed shape as shown in Figure 2.7 (a). They also observed an increase in temperature resulted in the development of plate-like dispersoids located in dislocations, as shown in Figure 2.7 (b). They suggested that the dislocations acted as nucleation sites for the dispersoids.

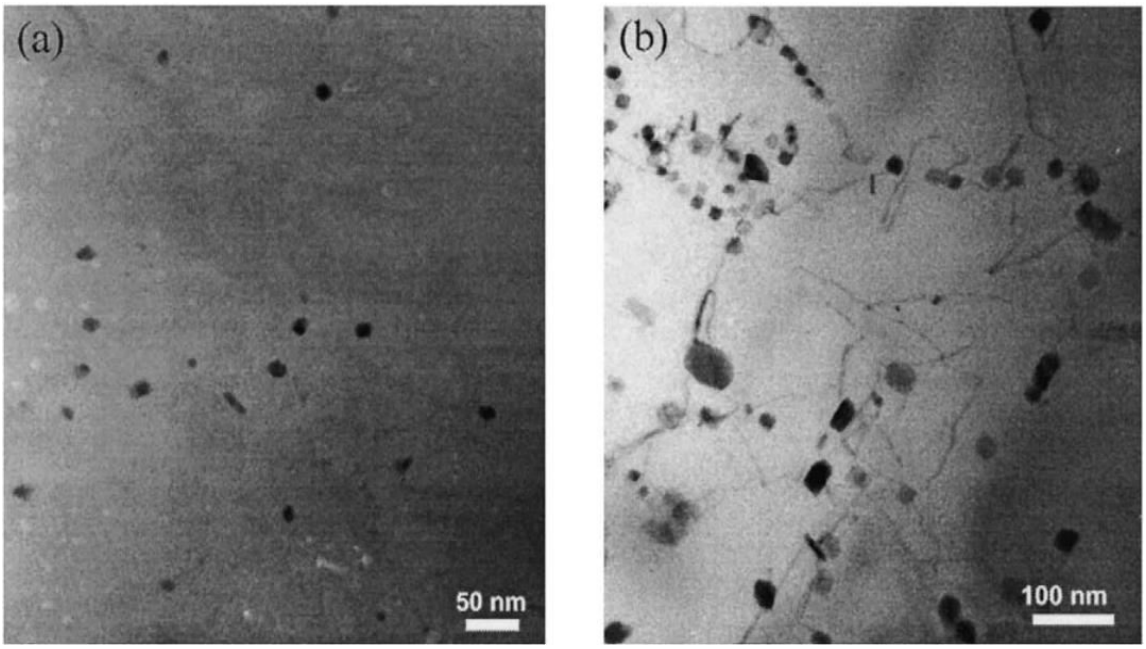

Figure 2.7. TEM micrographs of dispersoids precipitated during heating. (a) 300°C, (b) 400°C [22].

Li and Arnberg [22] also showed that, an increase in homogenisation temperature affected the size and density of the dispersoids developing within the matrix. The authors compared the minimum feret diameter, f_{min}, and maximum feret diameter, f_{max}, of the dispersoids, as shown in Figure 2.8. An increase in the aspect ratio of dispersoids with an increase in homogenisation temperature was observed. The number density similarly increased with temperature during heating but quickly dropped after the 400 – 450°C range. The size of the dispersoids on the other hand continued to grow with the increasing homogenisation temperature. They established from the dispersoids' size

and number density evolution that nucleation and growth at low temperatures primarily drive precipitation [22].

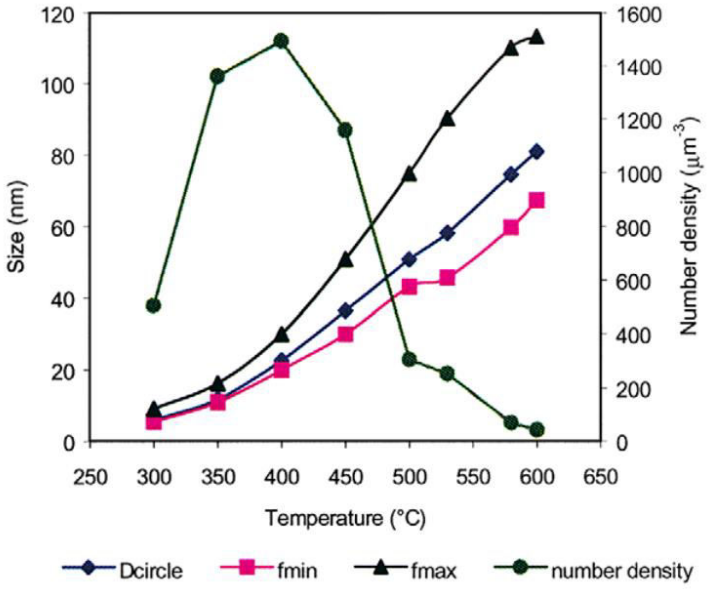

Figure 2.8. Size and number density evolution of dispersoids during heating [22].

2.6 Microstructure deformation

Aluminium is a crystalline material with a high stacking fault energy, so its plastic deformation is carried out mainly by dislocation slip in the lattice structure [9]. Aluminum has a high stacking fault energy, typically in the range of 160 to 250 mJ/m², which is significantly higher than many other metals, especially those like brass and stainless steel with very low SFE (<10 mJ/m²) [48]. Deformation results in defects that act as obstacles to the dislocation movement. These defects include point defects (vacancies, interstitials), line defects (dislocations), two-dimensional defects (grain boundaries, twin boundaries), three-dimensional defects (second phase particles, inclusions, voids), and planar defects in coherent interfaces (stacking faults) [9]. The fundamental microstructural properties that describe a hot deformed structure are (a) the size and shape of the deformed grains and (b) the substructure inside the deformed grains. The final microstructure created after rolling is determined by the initial microstructure, alloy chemistry, and the thermomechanical history (strain, strain rate, and temperature). The primary processes influencing these changes are recovery, recrystallization, and grain growth, which ultimately define the sheet characteristics [1]. During plastic deformation of aluminium, the lattice stores energy required to create the deformation in the form of strain energy. Strain energy measures the internal work performed by the material to accommodate the deformation caused by dislocations.

2.7 Annealing

Annealing is a heat treatment that is used to restore the physical and chemical properties of a material after deformation and strain hardening. The main mechanisms of annealing involve the release of internal stored energy through the reorganisation or removal of dislocations and dislocation structures within deformed grains. The driving force for annealing is related to the level of stored energy or strain accumulation, and the annealing processes needs heat to activate them. At moderate to high temperatures, dislocation movement and grain boundary migration within the lattice occurs to progress towards a state of greater equilibrium of the material. Annealing is commonly used on deformed material to relieve stress, enhance softness, ductility, toughness, and/or develop a specific microstructure [49].

2.7.1 Recovery

When a polycrystalline metal is deformed at a temperature that is relatively lower than its absolute melting temperature, it results in metal with altered microstructure and properties. In a metal with a low stacking fault energy, dislocation motion is comparatively difficult, leading to a mainly random dislocation distribution after deformation. On the other hand, metals with moderate to high stacking fault energy, like aluminium, typically form cellular structures with rough tangles of dislocations making up the cell walls [50]. The microstructure and properties change result from change in the metal's grain shape, multiplication of the dislocation density and strain hardening. To restore these properties and crystal structure to the pre-cold worked state, recovery is the initial process of annealing treatment that occurs at elevated temperatures, typically below one-third of the absolute melting point.

During recovery, some of the stored internal strain energy is released by dislocation motion (in the absence of an externally imposed stress) where the main mechanism is annihilation of point defects and rearrangement of dislocations into sub-grains [51]. At elevated temperatures, the dislocations become mobile and move around by cross-slip, glide or climb. The dislocations rearrange themselves into low energy configurations, known as sub-grains, resulting in reduction in stored energy. This happens by polygonization where same sign dislocations rearrange to into low-angle grain boundaries being the tilt boundaries. The screw dislocations will rearrange into twist boundaries [52]. Climb and slip are the dislocation movements required during polygonization. Polygonization is temperature dependant making dislocation motion by climb not possible as it

depends on vacancy motion which is a thermally activated process. Dislocation movement by slip is also difficult at low temperatures. In Figure 2.9, the reduction and rearrangement of dislocation within the deformed parent grains is illustrated. Figure 2.9 (a) depicts the high dislocation density of the deformed state; while Figure 2.9 (b) represents the restored state after recovery where the low-angle grain boundaries are created by the rearranging of dislocations, which results in sub-grains.

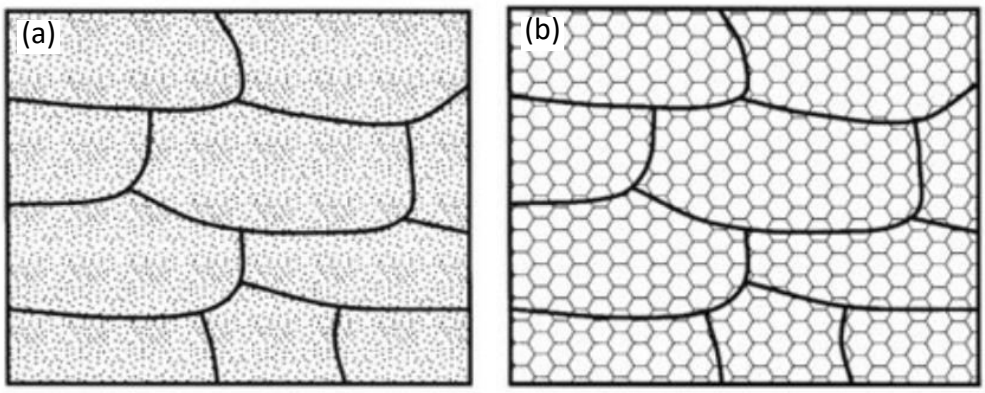

Figure 2.9. Schematic illustration of the effect of annealing on the microstructure of a cold worked metal: (a) cold-worked condition, (b) after recovery [53].

2.7.2 Recrystallisation

Recrystallisation of the material entails the nucleation and initial growth of a resolvable new strain-free grain within the deformed structure. Recrystallisation occurs through the formation and migration of high-angle grain boundaries driven by the stored energy owing to the deformation. High-angle boundaries have a misorientation angle of greater than 15° [54]. Recrystallisation takes place during post-deformation heat treatment. The driving force for recrystallisation is the difference between the energy of the deformed and the recrystallised state of the material. Recrystallization is impeded or severely retarded by the dispersion of small, closely spaced particles caused by Zener pinning on both low- and high-angle grain boundaries [55].This pinning pressure directly opposes the driving force caused by dislocation density and influences both nucleation and growth kinetics.

Recrystallisation is a discontinuous or continuous process. Discontinuous recrystallisation, common in low stalking-fault energy material, involves nucleation and growth of distinct new grains. Grain boundaries are the easiest places for it to happen, which reduces grain sizes and increases nucleation sites. Continuous recrystallisation refers to the gradual evolution of a deformed

microstructure into a recrystallised microstructure. There is no nucleation and grains with a lower dislocation density grow at the expense of more deformed grains [55].

2.8 Texture

Texture is the term used to describe the preferred crystallographic orientation of a large number of crystallites seen in many materials [56]. An ideal polycrystal has p, grain oriented randomly with no dominant direction, however processes, including rolling, drawing, and annealing, particular orientations dominant due to the mechanical deformation and recrystallisation resulting in preferred orientation texture.

Earing, which is the development of wavy edges on deep-drawn aluminium cans, is a direct result of crystallographic texture, which affects the anisotropic deformation behaviour of the material. Hirsch et al. [57] explain that the strength of the cube texture in the hot strip and the quantity of subsequent cold rolling has a crucial role in the production of the suitable texture with the least amount of earing at the final gauge. The recrystallization processes that take place after hot rolling have a major role in controlling the evolution of microstructure and texture. These processes are influenced by the temperature at which deformation occurs, the rate of strain, the degree of recovery, and possibly the amount of recrystallization that occurs between the independent hot rolling passes [58].

2.8.1 Effects of dispersoids on recrystallised grains and texture

Dispersoids play a crucial role of determining the recrystallised grain sizes and distribution in aluminium alloys. These particles regulate recrystallisation by boundary pinning effect, controlling the grain growth and texture evolution. Higginson et al. [59] demonstrated that decreasing the annealing temperature while increasing the dispersoid concentration results in increase in recrystallized grain size and aspect ratio. They also studied the effect of dispersoids on primary recrystallisation texture and discovered that the particle content in alloys has a significant influence on the crystallographic texture created during primary recrystallisation. Additionally, increasing numbers of dispersoids were connected to increased cube texture formation at the expense of other texture components. Dispersoids influence grain boundary mobility via the Zener pinning mechanism. Pinning has an effect on recrystallization textures, especially when it inhibits nucleation [59].

2.9 Earing

A beverage can is manufactured using a series of drawing and ironing operations. In a press operation, 12-14 circular blanks are stamped out in parallel from 0.25-0.30 mm thick extremely cold-rolled sheet, followed by deep drawing into a cup. The plastic flow parameters of cups deep drawn from circular blanks cut from a textured sheet change with the angle α around the sheet relative to the rolling direction. Earing arises from the anisotropy of the plastic stain ratio "r" in sheet with a preferred orientation. In sheet metal subjected to uniaxial tension, the plastic-strain ratio (r) is the ratio of the true strain in the width direction (ε_w), which is perpendicular to the applied stress, to the true strain in the thickness direction (ε_t). Therefore, r is given by the equation $r = \frac{\varepsilon_w}{\varepsilon_t}$ [60]. Orientations with a high r value resist wall thickening caused by compressive hoop strain, resulting in the formation of an "ear" on the drawn cup. Conversely, orientations with a low r value thicken more, leading to the formation of a trough [3]. The critical factors for earing have been attributed to the initial texture and the spatial distributions among different texture components, which are defined by the re-roll texture after hot rolling and the following cold rolling reduction. Earing is also termed "plastic anisotropy".

Thomas [61] explains that plastic anisotropy in metal sheeting is mostly caused by preferred grain orientations or crystallographic textures that emerge during the rolling process. Thomas adds that mechanical anisotropy in AA3004 alloys is controlled in principle by balancing the cube texture developed during annealing (recrystallisation) with the rolling texture produced during subsequent cold rolling. A recrystallized hot band's characteristic cube texture produces four ears at 0° and 90° to the former rolling direction, but a cold-rolled sheet with the typical β fibre rolling texture produces four ears at 45° to the rolling direction [62] [63]. For cup drawing it is critical to achieve a balanced {001}<100> cube texture and β-fibre texture (Bs {011}<211>, S {123}<634> and Cu {112}<111>) in AA3104 [3].

2.10 Effects of homogenisation parameters

The industry uses different homogenisation profiles for a material with the same structure and chemical composition. The profiles differ from the heating rate to the soaking temperature to the cooling rate. The thermal profile (temperature and duration) of an as-cast affects the microstructure it retains during homogenisation [26].

2.10.1 Heating rate

Gandi and Tech [26] explain that the industry uses a range of heating rates from around 45°C/hr to around 70°C/hr on their ingots during homogenisation. Their study showed that to create fewer dispersoids and a little greater volume fraction of α-$Al_{12}(Fe,Mn)_3Si$, a faster heat-up rate is preferable. They further observed a delay in the lowering of Mg and Mn micro segregation throughout the cell due to an increase in heat-up rate.

IMPs' dynamics are also affected by the heating rate. Homogenisation of the AA3104 results in fragmentation of large β-$Al_6(Mn,Fe)$ phase and precipitation of the $Al_x(Fe,Mn)_3Si_x$ dispersoids. The rate of heating affects the degree of this transformation; whereby a higher heating rates may result in a less even dispersion of these phases [20].

2.10.2 Homogenisation temperature

Microstructural characteristics and mechanical properties of AA3104 alloy are determined by the homogenisation temperature. Elevated solute supersaturation, especially of Mn, in solid solution is observed at high homogenisation temperatures at the range of 600°C to 610°C [44]. This is crucial as high Mn content provides stronger pinning effect against the dislocation movement during the deformation resulting in improved mechanical properties. The peak Mn precipitation temperature, where the equilibrium Mn in solid solution rises with increase in temperature, is 480°C [26]. At high homogenisation temperature, there is an increase in volume fraction of α-phase to β-phase. The β-$Al_6(Fe,Mn)$ particles undergo a eutectoid reaction which transforms them to α-$Al_{12}(Fe,Mn)_3Si$ at elevated temperatures [64]. Gandhi and Tech [26] found that as temperature increased during heat up, the size of dispersoids, $Al_{12}(Fe,Mn)_3Si$, increased, as illustrated in Table 3. This asserts that the coarsening of the dispersoids is a direct consequence of temperature.

Table 3. Change in $Al_{12}(Fe,Mn)_3Si$ dispersoid mean size during preheat heat-up and soak [26].

Preheat treatment	**Average α-$Al_{12}(Fe,Mn)_3Si$ precipitate size (nm)**
As-cast	-
Heat-up to 400°C	35
Heat-up to 450°C	47
Heat-up to 500°C	66
Heat-up to 600°C	108

Heat-up to 600°C, cooled to 500°C at 30°C/hr	136
Heat-up to 600°C, soaked for 8 hrs and cooled to 500°C at 30°C/hr	150

2.10.3 Soaking time

High homogenisation temperatures, ≥ 600°C, facilitate faster diffusion and that coupled with long soaking time allows for dispersoids coarsening [65]. The soaking time also impacts the transformation and spheroidisation of intermetallic phases such as α-$Al_{12}(Fe,Mn)_3Si$. As soaking time increases, these phases can become more refined based on the homogenisation temperature and soaking time [65]. Kamat [65] explained that increased soaking time allows precipitate coarsening and also results in increased dispersoids sizes.

2.10.4 Two-step homogenisation

The two-step homogenisation process begins with a high-temperature soak and is followed by a lower-temperature treatment. The two-step homogenisation process for AA3104 aluminium alloy in can manufacturing typically involves an initial high-temperature soak between 560–580°C followed by a lower-temperature treatment at 520°C, each held for 4 hours. This contrasts with single-stage homogenisation practices, which often use a higher temperature of ~600°C [20]. This technique aids in reducing the ingot temperature to the required rolling temperature for transfer to rough rolling. However, the Mn solubility is usually reduced at this homogenisation temperature and as a result, there is a further Mn precipitation on existing dispersoids, and on Mg_2Si particles during heat-up to the homogenisation temperature. The nucleation of these new dispersoids will have a finer and more uniform distribution.

2.11 Microstructural changes in AA3104 during hot rough rolling and inter-pass

Work hardening and dynamic restoration are the microstructural changes that occur during the hot deformation stage. The applied strain during the rolling process increases dislocation density inside the grains. This accumulation of dislocations contributes to work hardening whereas the softening occurs because of competing recovery and recrystallisation restoration procedures[66]. Because of its high stacking fault energy (SFE), AA3104's major softening process is dynamic recovery. It

stabilises the microstructure and slows the rate of recrystallisation. Static recovery is comparable to dynamic recovery but does not involve continuous deformation. During the brief inter-pass time between rolling passes, dislocations can rearrange themselves via recovery mechanisms, resulting in a softer material. Static recrystallisation happens during inter-pass intervals when the temperature and time are sufficient to nucleate and develop new grains to replace deformed ones. In AA3104, thermally stable dispersoids create a strong barrier to grain boundary movement, which is required for static recrystallisation [40].

2.12 Plane Strain Compression (PSC) testing

Plane strain compression (PSC) testing is a thermomechanical procedure intended to simulate industrial rolling deformation. PSC is used to measure mechanical properties and investigate microstructure development during thermomechanical treatment. Microstructural evolution is influenced by thermomechanical processing (TMP) parameters such as strain amount, strain rate, and temperature. PSC testing involves deforming a rectangular test sample across its breadth with a pair of narrow anvils that are longer in length than the breadth of the testing sample. This results in a thin rectangular deformation band spanning the sample. Figure 2.10 shows the typical PSC testing configuration and layout.

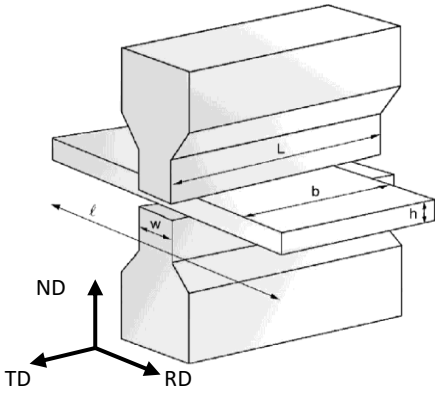

Figure 2.10. A schematic of plane strain compression illustrating the anvil and test sample in relation to their orientation, along with key variables relevant to the testing procedure [67].

PSC testing was originally intended to simulate plate or strip rolling since the imposed deformation is closely related to the plane strain condition [68]. Hot PSC testing is one of the most frequently employed tests for generating flow stress data for use in material TMP simulation. This method of testing is beneficial for testing conditions requiring high strains, where the axisymmetric compression test is ineffective due to strain limits caused by barrelling at high strains. Furthermore,

PSC testing is appealing due to the compression of a relatively large volume of material, allowing for appropriate microstructural examinations [69].

PSC testing will be performed on a Gleeble 3800 system, which is a fully integrated device capable of heating at speeds of 10,000°C/s and keeping material at a steady temperature within a 1°C interval. Gleeble 3800 incorporates water-cooled grips that provide quick cooling. The mechanical system is completely integrated and capable of exerting up to 20 tonnes of static compression force. The apparatus has displacement rates of up to 2,000 mm/s, which allows for strain rates of 100 s^{-1}, which are in line with industrial finish rolling parameters, making this an ideal tool for lab-scale simulation of hot finish rolling of aluminium alloys[70].

3. Methodology

3.1 Material preparation

Local industry supplied the Centre for Materials Engineering at the University of Cape Town with four samples extracted from the centre of a slice from a DC cast ingot. The ingot material samples, as shown in Figure 3.1, had dimensions of 140mm x 48mm x 100 mm (Length x Height x Width). These samples formed the “ingots” for the laboratory scale rough rolling process that was part of the experimental plan. The ingot samples were examined for their composition at Mintek using the spark optical emission spectrometer, shown in Figure 3.2. The composition of the ingots was found as shown in Table 4 .

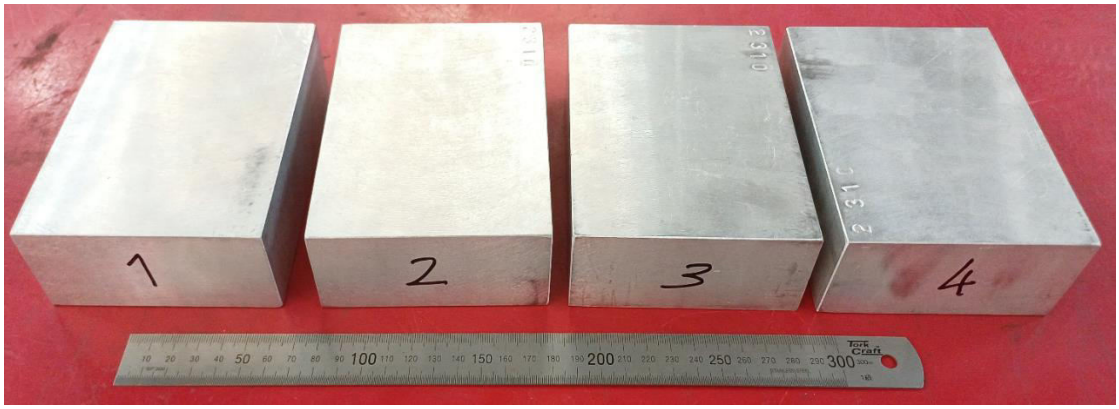

Figure 3.1. Four (4) AA3104 ingots from Hulamin.

Figure 3.2. Spark spectrometer at Mintek.

Table 4. Hulamin AA33104 material composition

Hulamin AA3104	Si	Fe	Cu	Mn	Mg	Cr	Zn	Ti	Al
	%	%	%	%	%	%	%	%	%
	0,233	0,468	0,215	1,237	1,157	0,021	0,024	0,014	96,6

3.2 Homogenisation

During the casting processes of aluminium ingots, an aluminium alloy may develop non-uniform microstructures or concentrations of alloying elements due to partitioning of eutectic elements during solidification. To correct the non-uniformity and uneven concentration, the ingots are then homogenised. This involves exposure of the ingot to elevated temperatures below the melting point of the material for a certain duration. This will allow for the diffusion of the alloying elements to approach a more uniform distribution and the evolution of IMPs and dispersoids within the structure.

The ingots were homogenised on a programmable furnace, as shown in Figure 3.3. To increase accuracy in the measured temperature of the ingot, a thermocouple was placed on the ingot to measure the direct temperature of the ingot and not of the furnace. A dummy block was used to hold down the thermocouples, as shown in Figure 3.4, and would later be used to warm up the milling machine.

Figure 3.3. Programmable furnace with a thermocouple connected to a data logger.

Figure 3.4. The inside of a programmable furnace with an ingot (bottom) and dummy (top) sandwiching thermocouples.

In a one-step homogenisation, the cast ingot is heated to a specific temperature for a set duration before being cooled below the homogenisation temperature range or immediately hot-rolled, whereas, in a two-step homogenisation, the ingot is heated sequentially to two distinct temperatures, each for a specified time. For the four ingot samples shown in Figure 3.1, each ingot was assigned a homogenisation practice as indicated in Table 5. Ingot labelled "4" was not homogenised and left with as-cast microstructure.

For homogenisation practice 1 in Table 5, the sample was heat treated using two-step homogenisation. In the first step, the sample was heated to 600°C in a furnace with a heating rate of 50°C/hr. The sample was held at that temperature for 8 hours. The furnace was then cooled to 520°C where the second homogenisation step was initiated. The soaking time for this step was 4 hours. The sample was then allowed to cool to room temperature at a rate of approximately 50°C/hr. In homogenisation practice 2, the heating profile was also a two-step heat treatment. The heat-up and cooling rates were consistent with those of homogenisation practice 1. In this heat treatment, the first-step homogenisation temperature was 560°C with a 4-hour soaking time. The second step was at 520°C with a 4-hour soaking time. Homogenisation practice 3 was a one-step heat treatment with a homogenisation temperature of 520°C. The soaking time was 4 hours. A presentation of the three homogenisation protocols which includes their heating and cooling rates is shown in Figure 3.5.

Table 5. Experimental homogenisation matrix

Experiment Number	Temperature 1 (°C)	Time (Hours)		Temperature 2 (°C)	Time (Hours)
		4	8		4
1	600		x	520	x
2	560	x		520	x
3	520	x			

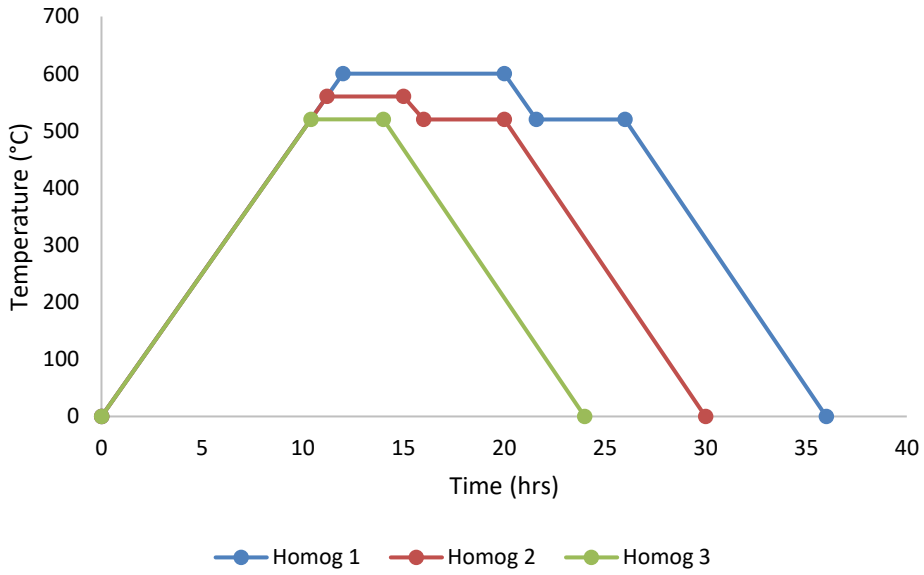

Figure 3.5. Homogenisation profiles imposed on the ingots with 50°C/hr heating and cooling rate.

3.3 Rationale for chosen homogenisation protocols

The homogenisation protocols were chosen to generate a range on dispersoid structures, but to still be representative of typical industrial protocols. The temperature of the first step was chosen for its effect on IMP phase transformation and dispersoid development, while the lower second step was chosen primarily as industry will include a step to reduce the ingot temperature to the required rolling temperature. Additionally, there is reduced Mn solubility at this temperature, resulting in further Mn precipitation on existing dispersoids, and the formation of new dispersoids that are a lot smaller, which may result in a bimodal dispersoid distribution in the two-step homogenisation practices.

3.3.1 Homogenisation 1: 600°C/520°C

The temperature for the first step of homogenisation practice 1 is in line with the standard temperature used for AA3104 alloys in the rolling of sheet using a tandem mill. As described in 2.10.2, high homogenisation temperatures, ≥ 600°C, facilitate faster diffusion and that coupled with long soaking time allows for dispersoids coarsening [65]. This temperature protocol was chosen to result in coarse dispersoid within the structure, which are associated with the acceleration of recrystallisation by Doherty and Martin [42].

Based on the work by Gandhi and Tech, a treatment within this temperature range should result in $Al_{12}(Fe,Mn)_3Si$ dispersoid mean sizes in the range of 108-150 nm in the first stage [26].

3.3.2 Homogenisation 2: 560°C/520°C

The temperature for the first step of homogenisation practice 2 is slightly below the commonly used temperature used for AA3104 alloys in the rolling of sheet using a reversing mill. As described in 2.10.2, Lodgaard and Ryum [21] showed that at temperatures greater than 550°C, dispersoids begin to dissolve as Mn solubility increases, and as such this temperature was chosen to result in smaller dispersoids with a close distribution, before diffusion of Mn resulted in a more sparse distribution.

Based on the work by Gandhi and Tech, a treatment within this temperature range should result in $Al_{12}(Fe,Mn)_3Si$ dispersoid mean sizes in the range of 66-108 nm in the first stage [26].

3.3.3 Homogenisation 3: 520°C

The temperature for the single step of homogenisation practice 3 is that of the first step of the first two homogenisation practices. Owing to the relatively low temperature, there is reduced Mn solubility at this temperature, it is predicted that this protocol will result in the formation of very small dispersoids. These small, closely located dispersoids will results in greatly increased Zener drag, which is a retarding force caused by primary and newly formed particles that slow down grain boundary motion during recrystallisation [38]. The effect of small dispersoids is insufficient to stop boundary migration creating the absence of appropriate nucleation sites for new grains, and as such fewer recrystallisation nuclei, thus resulting in larger recrystallised grain sizes. If dispersoid sizes are small enough there may be no recrystallisation.

Based on the work by Gandhi and Tech, a treatment within this temperature range should result in $Al_{12}(Fe,Mn)_3Si$ dispersoid mean sizes in approximately 66 nm [26].

There may also be reduced diffusion of solute atoms overall to facilitate the phase transformation from the β IMPs to the α IMPs at this low temperature, but owing to the relatively fast diffusion of Si at low homogenisation temperatures, some β to α transformation of the IMPs will occur as this transformation process is dependent on the Si diffusion. However, neither extensive particle break-up due to duplex phase transformation, nor spheroidisation of the IMPs is not.

3.4 Hot rolling mill

3.4.1 Rolling mill

The rolling of the samples was conducted at Mintek on the Carl Wezel rolling machine shown in Figure 3.6. The machine has a roll diameter of 340 mm, a maximum rolling width of 300 mm and a maximum roll gap of 37 mm. The maximum rolling speed of the machine is 46 rpm. For the proposed rolling schedule, the machine' roll gap was set to be within the ±0.1 mm tolerance. The rolling speed was set to 8 rpm.

Figure 3.6. Carl Wezel rolling machine at Mintek

3.4.2 The rolling schedule

The planned rolling schedule to be performed at Mintek for this investigation is as shown in Figure 3.7. The diagram shows the planned entry and exit gauges, the true strain and the total reduction of the material. The true strain of the material in the normal direction was calculated as:

$$\varepsilon_t = \ln\left(\frac{Exit\ height}{Entry\ height}\right) \qquad (1)$$

In the schematic in Figure 3.7, the as-cast or homogenised sample is imposed to 75% reduction in four procedure blocks (4 passes). In the first rolling block, the starting gauge is 48 mm and is heated up to a temperature gauge of 480-500°C using a programmable furnace. The sample is rolled to achieve a 26.5 mm gauge which results in a 0.5941 strain. The 26.5 mm gauge sample is taken back to the programmable furnace and heated up to a temperature in the 460 – 475°C gauge. For the second block, the sample is then rolled to a 21.6 mm gauge, attaining a 0.2051 strain in the process. The sample is taken back into the furnace to heat it to a 440 – 450°C temperature range. This is followed by rolling from a 21.6 mm gauge down to 16.6 mm to impose a 0.2624 strain on the sample. Before the third block rolling, the sample is heated up to a 410 – 415°C temperature gauge. The sample is then put on the mill to roll it down from 16.6 mm to 12.0 mm gauge. This results in 0.3233 strain accumulation by the sample.

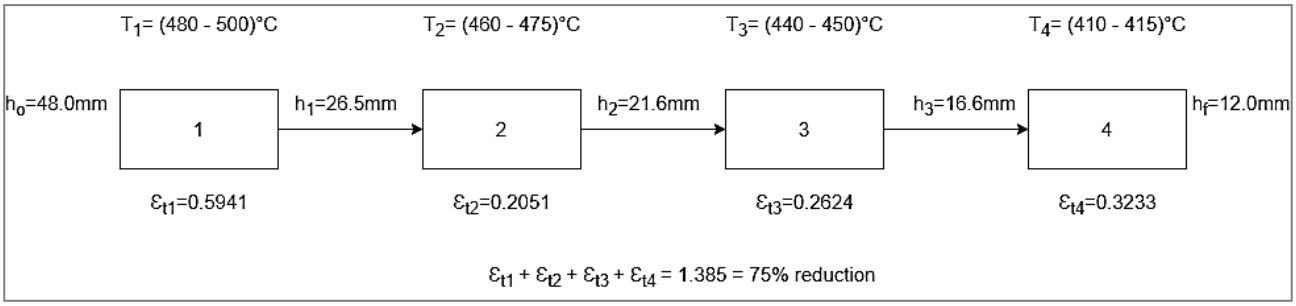

Figure 3.7. Schematic diagram of rolling procedure.

However, Mintek revised the rolling procedure. For gauges above 5mm, it is advisable to have approximately 27% reduction between passes to avoid cracks and getting the samples stuck in bite roll. The revised procedure was used to roll the samples and consisted of nine passes. The total strain for the nine passes remained to be 1.385. The total reduction is also 75% the initial gauge is 48 mm and the gauge after nine passes is 12 mm according to the equation (1). The rolling schedule reported in the Table 6.

Table 6. Revised Mintek rolling schedule

	$h_o(mm)$	$h_f(mm)$	Δh	$reduction\ (\%)$	ε_t
Pass 1	48	35	13.0	27.08	0.316
Pass 2	35	26.5	8.5	24.29	0.278
Pass 3	26.5	22.5	4.0	15.09	0.164
Pass 4	22.5	21.6	0.9	4.00	0.041
Pass 5	21.6	18.4	3.2	14.81	0.160
Pass 6	18.4	16.5	1.9	10.33	0.109
Pass 7	16.5	15	1.5	9.09	0.095
Pass 8	15	13	2.0	13.33	0.143
Pass 9	13	12	1.0	7.69	0.080

3.5 Optical Microscopy Procedure

The grain structure of the as-cast and the homogenised bars from the Hulamin were studied under a Nikon Eclipse MA200 light microscope.

3.5.1 Sample Preparation

Sample preparation for the investigation of samples under a light microscope involved extracting a sample from each bar. Cubical samples were extracted with the use of a hand-cutting saw. The rough dimensions of the samples were 10mm x 10mm x 5mm (LxWxD). The samples were then hot-mounted in clear acrylic resin, ClaroFast, for polishing and grinding. Struers Labopress-3 hot mounting machine was used to mount the samples with settings of heating cycle of 150°C at 20kN for seven (7) minutes and a cooling cycle of seven (7) minutes. The hot mounting is regarded to be relatively low to have any significant effects on the microstructure of the sample being mounted.

3.5.2 Grinding and polishing

The hot-mounted samples were all grinded down until a smooth planar finish was attained using a waterproof 1200 grit SiC on a manual Struers LaboPol-25 grinding machine. The polishing protocol used on the samples is summarised in Table 7. Polishing was performed on a Struers Tegramin-25 machine. Lubricants used in the polishing process were the 3 µm water-based diamond suspension and an OP colloidal silica suspension. The 3µm suspension was used in the initial polishing step and the OP suspension was used to achieve a mirror-like surface.

Table 7. Grinding and polishing procedure on AA3104 samples

Step	Force	Speed	Pad	Lubricant	Time (min)		Comments
					Automatic	Manual	
Grinding	-	300 rpm	1200 grit SiC	Water		3	Should be even and planar
Polishing	15N	150 rpm	Mol pad	3µm suspension	10		
Polishing	10N	150rpm	Nap pad	OP suspension	2		
Polishing	10N	150 rpm	Nap pad	Water	1		If has scratches, repeat previous steps

3.6 Plane strain compression (PSC) testing

The plane strain compression testing was investigated on the samples using Gleeble 3800 commissioned and calibrated at UCT CME. This is a multipurpose thermomechanical testing machine.

3.6.1 Sample preparation

The test piece should be obtained by cutting or machining to minimise residual stresses and changes in local microstructure close to the surface [67]. The preparation of the PSC samples was initiated with 12 mm gauge plates rolled down from 48 mm gauge. After the ingot blocks shown in Figure 3.1 were heat treated according to the homogenisation protocols and rolled into plates, the plates shown in Figure 3.8 (a) were milled into strips into 20 mm strips shown in Figure 3.8 (b). The strips were then skimmed down to dimensions shown in Figure 3.8 (c). Lastly, the test piece samples were extracted from the skimmed strip in Figure 3.8 (c) using the dimensions demonstrated by Figure 3.8 (d).

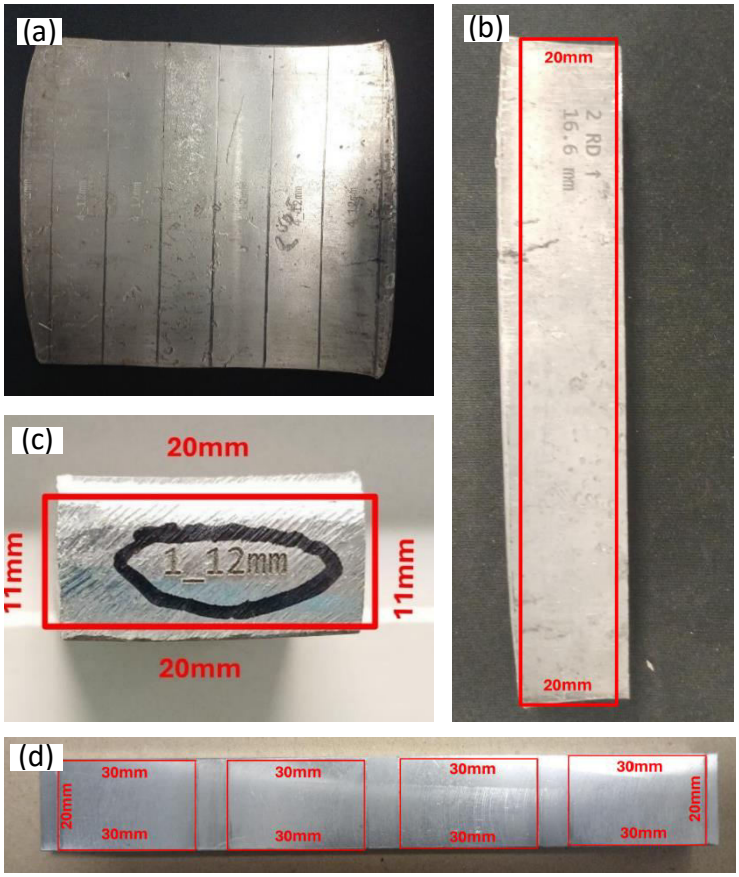

Figure 3.8. (a) 12 mm gauge rolled plate with 20 mm strips marked out. (b) 20mm strip cut off the rolle3d plate in (a). (c) 20 mm strip marked for skimming

The physical initial geometric dimensions of the sample and anvil have a considerable impact on the PSC testing technique and outcomes, particularly the strain distribution within the sample and the degree of width spreading of the deformed sample. Table 8 describes the appropriate geometric ratios for hot PSC tests, as per the NPL Good Practice Guide.

Table 8. Test piece Aspect Ratios [71]

Symbol	Title	Relationship	Preferred values	Permissible values
B_R	Breadth ratio	$B_R = \frac{b_o}{w}$	5	≥ 2
H_R	Height ratio	$H_R = \frac{h_o}{w}$	0.67	≤ 0.67
l_R	Length ratio	$l_R = \frac{l}{w}$	3	≥ 3

where b = testpiece breadth, h = testpiece height (thickness), l = testpiece length and w = platen width.

The sample's height dimensions were measured before and after deformation using a micrometre at various points, as shown in Figure 3.9. The sample's initial (h_o)and final (h_f) heights were computed by averaging the five height readings taken before and after deformation shown in Figure 3.9 (a) and Figure 3.9 (b) respectively. The sample's initial breadth value (b_o) was computed similarly using vernier callipers at the three indicated sites, as shown in Figure 3.9 (a). The width spread (b_f) value after deformation is only measured once, as illustrated in Figure 3.9 (b).

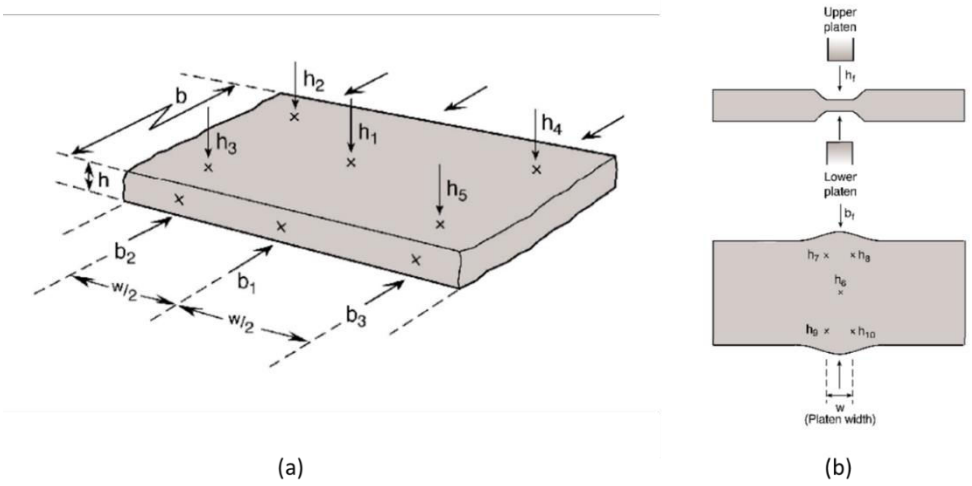

Figure 3.9. (a) Test piece geometry before testing and approximate dimensional. (b) schematic diagram of test piece after testing and approximate dimensional measurement positions [71]

The Gleeble 3800's anvil set was used for the PSC tests, as per DSI's standard sample geometric dimensions. Table 9 describes the DSI's suggested nominal geometric dimensions for the anvil and sample. Samples were machined to precise orientations in regard to the rolled strip, with the RD measured along the l (20 mm) direction, the ND measured along the h (11 mm) direction, and the strip's TD measured along the b (30 mm) direction is shown in Figure 3.10.

Table 9. Nominal dimensions recommended by DSI for PSC testing. [71]

Title	Symbol	Value
Anvil length	L	42 mm
Anvil face width	w	10 mm
Sample length	l	20 mm
Sample breadth	b	30 mm
Sample height	h	10 mm
Breadth ratio	B_R	3
Height ratio	H_R	1

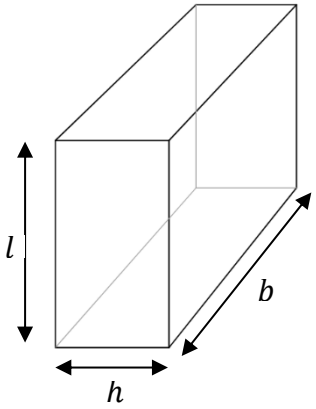

Figure 3.10. PSC testing sample geometry.

K-type thermocouples were used to measure and monitor the samples' temperatures. The thermocouples were surface welded to the deformation zone's surface, which is located in the middle of the sample's side. The control thermocouple (TC1) was placed nearest to the test chamber entrance, whereas the thermocouple (TC2) was symmetrically opposite in the centre of the ND and RD planes. TC1and TC2 measure the deformation zone temperatures of the sample, as well as monitor the thermal gradient across the sample's breadth.

Logging of the details of the test pieces was necessary. Table 10 describes in detail the test piece used in the Gleeble 3800's plane strain compression (PSC) testing. The material examined was an aluminium alloy AA3104, obtained from Hulamin. The test pieces were extracted from hot rolled strips. Test piece preparation followed conventional methods, including Good Practice Guide No. 27, and the geometry was classed as large PSC. The test piece was carefully cut with dimensions of 20 mm breadth, 11.044 mm height, and 30 mm length, resulting in an initial cross-sectional area of 200 mm² under the 10 mm platens. The surface polish was obtained with 1200-grit machining for uniformity and milling for precision shaping. The strict preparations guaranteed that the test findings were consistent and reliable.

Table 10. Test piece description format used throughout the experiment samples

Reference	Description	
Material	Source (industry document link)	Hulamin
	Identifier	ID 011 K.E.L 2024
	Composition	AA3104
	Note	-
	Condition	Rolled strip
	Location	-
	Heat treatment	Homog 2
Test piece preparation	Orientation (relative) and location from source mat	-
	Geometry	Large PSC
	Breadth Ratio (B_R)	2.00
	Length Ratio (L_R)	3.00
	Height Ratio (H_R)	1.10
	Applicable standard(s)	Good practice guide N0 27 and other appropriate documents
Test piece information	Test piece breadth b0 (mm)	20
	Test piece Height h0 (mm)	11.044
	Test piece length ℓ (mm)	30
	Initial cross-sectional area under platens (mm^2)	200
	Surface finish (Ra)	1200 grit from machined surface
	Method of machining	Milling

3.6.2 Testing details

Table 11 contains key facts about the testing method and environment on the Gleeble 3800 system. The PSC tests were conducted in a rough vacuum to reduce external impacts, with a temperature uncertainty of 1°C. To ensure uniform contact, the test pieces were subjected to a maximum programmed temperature while using hardened H13 anvils with a surface finish of 1200-grit. The heating was achieved through induction heating. There were no lubricants utilised, and cooling was achieved through air quenching. Sampling rates were kept at 10 Hz for the base and 50,000 Hz for impacts to ensure high-resolution data collection during deformation. The calibrated Gleeble setup and careful adherence to testing standards ensured that the results were reliable and repeatable, bridging both the technique and results sections.

Table 11. Test details of the Gleeble 3800 system

Description	Value	Units/notes
Type of test	Large PSC	
Anvil Width (w)	10	mm
Strain coefficient A	0.866	
Stress coefficient B	0.866	
Base sampling rate	10	Hz
Hit sampling rate	50000	Hz
Applicable standard(s)		
Test machine	Gleeble 3800	
Test environment	Rough Vacuum	
Temperature uncertainty	±1	°C
Anvil material	Hardened H13	
Anvil surface finish	1200 Grit	
Lubricant type	None	
Lubricant application method	NA	
Cooling method	Air Quench	
Anvil alignment	-	
Test calibration document name		
Last Gleeble calibration date	01/12/2023	

3.6.3 Hot rolling simulation

It should be noted that the system was calibrated for load, displacement and temperature, and the calibration procedure was documented. Also, the raw load displacement data was corrected for zero offset, machine compliance, increase in test piece breadth and friction to determine true stress- strain data as per Good Practice Guide No 27. The PSC sample was subjected to three hits occurring at 360°C, 330°C and 300°C respectively. The summary of the process parameters for the simulation of the 3-pass finish rolling simulation is shown in Table 12.

Table 12: summary of processing parameters for Gleeble testing.

Pass	Initial h (mm)	Temp (°C)	True strain	Delta h (mm)	Final h (mm)	Strain rate (/s)	Interpass (secs)
1	11	360	0.58	4.84	6.16	30	276
2	6.16	330	0.61	2.81	3.35	50	576
3	3.35	300	0.8	1.84	1.50	100	
Final h	**1.50**						

The temperature profile in Figure 3.11 demonstrates that the full hot rolling simulation was initiated with a 3°C/sec heating rate from room temperature to 360°C in 120 seconds. The sample is soaked for 90 seconds to ensure a uniform temperature distribution inside it. The sample was then subjected to a deformation hit of 0.58ε (true strain) at a strain rate of 30 s^{-1}. The sample is allowed to cool to second deformation temperature of 330°C at a rate of 0.109°C/sec over an inter-pass time of 276 seconds. The subject was then subjected to second deformation hit of 0.61ε (true strain) at a strain rate of 50 s^{-1}. The sample is further allowed to cool to third deformation temperature of 300°C at a rate of 0.052°C/sec over an inter-pass time of 576 seconds. The last and third deformation hit that the sample was subjected to was at 0.8ε (true strain) at a strain rate of 100 s^{-1}. The cooling rate of the sample after the third hit to 35°C was at 1.104°C/sec.

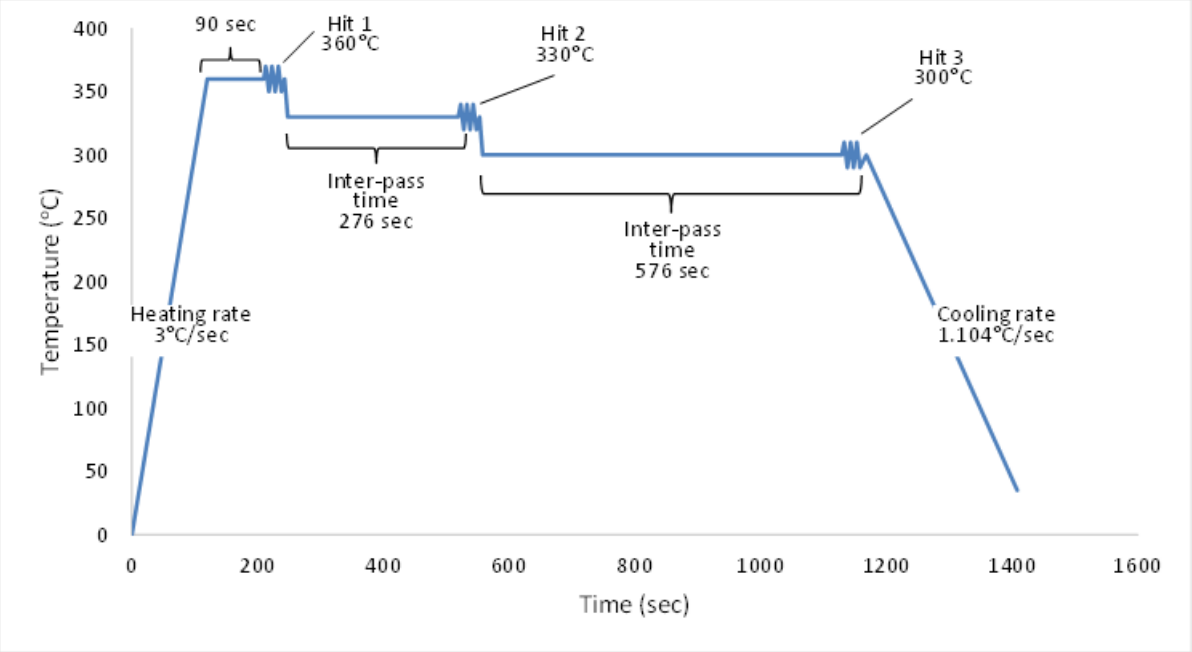

Figure 3.11. Graphical representation of the simulation 3 pass hot finish rolling

Tests where temperature, strain and strain rate values were outside of the target range were disregarded and excluded from the sample set.

3.7 Microstructure characterisation

The sample preparation for microstructure characterisation using electron backscatter diffraction (EBSD) initiated by cutting a 2-3 mm thick sample from the hot finish rolling simulation in Figure 3.12 (c). A low-speed precision saw which uses a coolant to reduce mechanical deformation, was used to cut the piece of interest from the sample. The samples were then hot mounted in clear acrylic resin, ClaroFast, for polishing and grinding. Struers Labopress-3 hot mounting machine was

used to mount the samples with settings of a heating cycle of 150°C at 20kN for seven (7) minutes and a cooling cycle of seven (7) minutes.

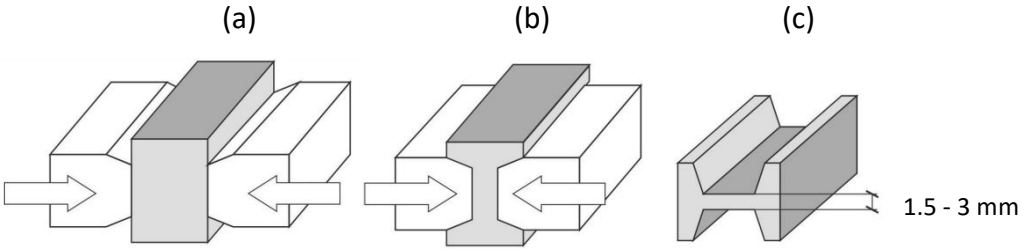

Figure 3.12. Schematic of a sample hot finish rolling simulation. (a) show the sample before hot finish rolling with the anvils just touching the sample. (b) shows the sample in hot finish rolling simulation. (c) shows the hot finish rolling simulated sample [72].

3.7.1 Grinding and polishing

The hot mounted samples were all grinded down to a clean planar finish using a waterproof 1200 grit SiC on a manual Struers LaboPol-25 grinder. The polishing process utilised on the samples is summarised in Table 13. Polishing was performed with a Struers Tegramin-25 machine. Lubricants used in the polishing process included a 3 µm water-based diamond solution and an OP colloidal silica suspension. The 3µm suspension was used for initial polishing, while the OP suspension was employed to obtain a mirror-like surface.

Table 13. Grinding and polishing procedure on EBSD AA3104 samples

Step	Force	Speed	Pad	Lubricant	Time (min)		Comments
					Automatic	Manual	
Grinding	-	300 rpm	1200 grit SiC	Water		3	Should be even and planar
Polishing	10N	150 rpm	Mol pad	3µm suspension	8		
Polishing	10N	150 rpm	Nap pad	OP suspension	1-2		

3.7.2 Ion polishing

After the grinding and polishing, the sample is unmounted from the acrylic resin and mounted on a stub. A conductive adhesive, silver paint, was applied to ensure the sample's proper electrical grounding while polishing. The mounted samples were then polished using a precision ion polishing system under the 5 kV accelerated voltage and 2 mA beam current. The polishing was completed

under a controlled environment using pure argon gas. The argon pressure was maintained within the chamber to produce an inert atmosphere and avoid oxidation during polishing. The sample was subjected to ion polishing for 40 minutes.

3.7.3 Annealing

Following ion polishing, the samples underwent annealing as follows: The furnace was preheated to a target temperature of 365°C, and the heating process was extended for an hour or more to guarantee that the temperature was stabilised and uniformly maintained at that level. Once the furnace reached a constant 365°C, the polished samples were carefully placed inside and heated for one hour to initiate the annealing process. Following the annealing process, the samples were removed from the furnace and allowed to cool naturally to room temperature. This technique guaranteed that the samples received controlled thermal treatment, allowing for the desired microstructural changes.

3.7.4 Data acquisition and analysis

The EBSD measurements were carried out using an MIRA3 SEM with an EBSD detector, and acquisition was achieved using the Aztec Crystal software. The sample was positioned on a holder with a tilt angle of 70° relative to the incident electron beam, ensuring optimal geometry for detecting backscattered electrons and producing distinct Kikuchi patterns. The SEM operating settings included an accelerating voltage of 15 keV, a beam current of 14 nA, and a working distance of 10 mm ± 0.2 mm.

The EBSD mapping was conducted over two defined areas: a large area measuring 1.2 mm × 2 mm to capture overall texture and a smaller study area of 300 µm × 300 µm to examine localised microstructural features in detail. A step size of 1 µm was selected to balance spatial resolution and data acquisition time. During indexing, 7 out of 10 detected Kikuchi bands were utilised to ensure high accuracy and reliability in crystallographic orientation determination.

The acquired EBSD data was examined using the ATEX software suite. Orientation distribution functions (ODFs) were created in three specific regions of Euler space: φ_2 = 0°, 45°, and 65°. These sections gave important information about the sample's crystallographic texture. The texture components of interest included the Cube and Goss (Gs) components, which are indicative of recrystallization phenomena, as well as the S, brass (Bs), and Cu components, which are indicative of deformation-induced textures.

3.8 Quantitative analysis

High-resolution images from SEM of the samples were used examine size and distribution of dispersoids in the AA3104 alloy. ImageJ software was used for image analysis, allowing extraction of quantitative data on the size and distribution of the dispersoids.

To standardise the analysis procedure, all micrographs were at a 15000x magnification according to SEM calibration with a scale bar of 5 µm. The micrographs were transformed to an 8-bit grayscale format to allow consistent particle analysis. Thresholding was applied to isolate the dispersoids from the matrix. The micrographs dimensions were calibrated for analysis using the 5 µm scale bar. There are varying software parameters that had to be set for each sample as the micrographs were captured at different settings based on how the particles appeared. Using homogenisation 1 samples as an example, the pixel saturation threshold was applied at 0.35% to minimize the impact of noise and exclude irrelevant particles. A global threshold of 1.99% was set to separate the dispersoids from background. The particles size was limited to a minimum of 0.004 µm² and no upper limit as the images only display dispersoids as large particles. The criterion was to exclude noise particles which could be misinterpreted as dispersoids. Table 14 summarises the parameters for all the homogenisation categories processed in ImageJ.

Table 14. Summary of the ImageJ analysis parameters for all samples.

	Image type	**Saturated pixel (%)**	**Threshold (%)**	**Particle size lower limit (µm²)**	**Particle size upper limit (µm²)**
Homogenisation 1	8 bit	0.35	1.99	0.004	Infinity
Homogenisation 2	8 bit	1.1	4.94	0.004	Infinity
Homogenisation 3	8 bit	1.1	5.04	0.004	Infinity

4. Results and Discussion

4.1 Characterisation of dispersoids

4.1.1 Identification of dispersoids

Scanning electron microscopy (SEM) with backscatter imaging was used to methodically examine the effects of various homogenisation procedures on the size and distribution of dispersoids within the aluminium alloy matrix. Figure 4.1 shows representative SEM micrographs of the homogenised and as-cast samples, highlighting the spatial and morphological variations in dispersoid properties under the different processing conditions. For these results, the dispersoids are roughly divided into circular and long bars. Circular dispersoids have an approximately spherical or circular shape when viewed in two dimensions, whereas long bars dispersoids are elongated dispersoids that resemble rods or bars, frequently with an aspect ratio (length/width) greater than one.

The backscatter image of the as-cast sample shown in Figure 4.1 (a), is distinguished by the presence of irregular IMPs, which appear as bright patches. It should be noted that SEM micrographs reveal the α-phase particles as bright whereas the β-phase particles are darker. Backscatter imaging reveals that these particles belong to the α-$Al_x(Fe,Mn)_3Si_2$ phase due to their increased brightness compared to β-$Al_6(Fe,Mn)$ particles. Notably, there are no dispersoids in the as-cast microstructure. This absence is consistent with the concept that dispersoid nucleation and subsequent growth are thermodynamic processes that require the high temperatures associated with homogenisation procedures [13].

The SEM image of the sample homogenised using the two-step homogenisation protocol 1, shown in Figure 4.1 (b), shows the existence of relatively large and coarse dispersoids scattered throughout the matrix. These dispersoids are significantly larger than those observed in samples homogenised using alternative protocols. The coarse character of the dispersoids shows that the elevated temperatures used in the first stage of protocol 1 promote particle coarsening through increased atomic mobility and diffusivity which promotes Ostwald ripening [22], [23]. This is an established consequence of prolonged exposure to higher temperatures during homogenisation, which promotes particle growth. Dispersoids' elongated shape is consistent with Zhao et al. [13] findings that high temperatures promote directed particle growth and coalescence.

In contrast, the microstructure of the sample processed using two-step homogenisation protocol 2 is shown in Figure 4.1 (c). Compared to those in Figure 4.1 (b), the dispersoids in this sample are notably finer and more evenly distributed across the matrix. This finding implies that the second step in protocol 2's lower temperature and shorter soaking period successfully restrict the diffusivity

of atomic species, preventing the formation of excessive particles. A more refined dispersoid structure is the end product, which is beneficial for properties which include grain boundary stabilization and Zener pinning, as noted by Ånes et al. [43].

Figure 4.1 (d) illustrates the microstructure of a sample subjected to the single-step homogenisation protocol 3, which used a lower homogenisation temperature than the initial phases of protocols 1 and 2. The dispersoids in this sample are smaller and have minimal coarsening. The smaller dispersoid size and restricted growth observed in this sample can be due to the lower homogenisation temperature, as lower homogenisation temperatures promote a high density of small dispersoids. Protocol 3 results support the notion that homogenisation temperature has an important role in determining the size and distribution of dispersoids inside the matrix. These smaller and dense dispersoids should be more effective at pinning grain boundaries up to the Zener limit.

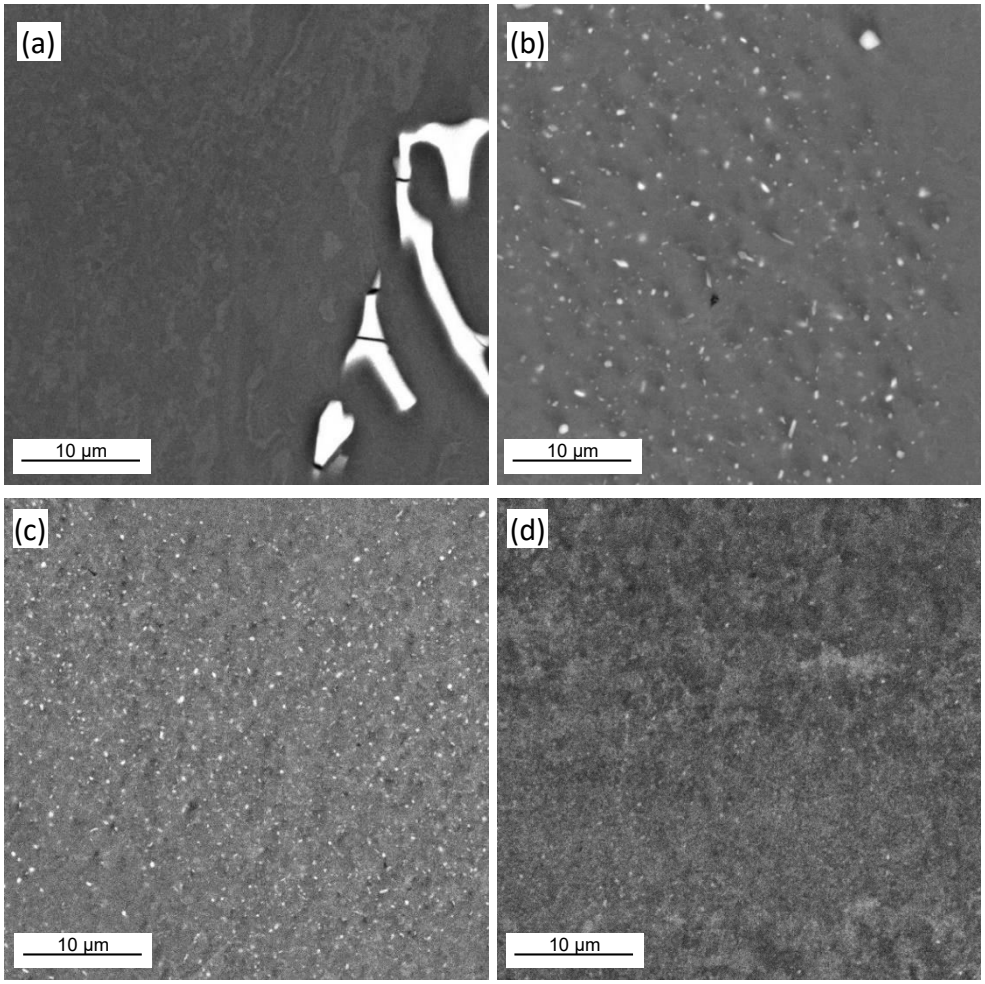

Figure 4.1. SEM images studying the presence of dispersoids in as-cast and homogenised samples. (a)As-cast sample, (b) homogenisation protocol 1 sample, (c) homogenisation protocol 2 sample, and (d) homogenisation protocol 3 sample.

Overall, the SEM micrograph analysis shows that homogenisation parameters such as temperature and soaking time are critical in determining dispersoid characteristics. Higher homogenisation temperatures, as used in protocol 1, tend to produce larger, coarser dispersoids due to higher atomic mobility and longer coarsening. Lower temperatures, as demonstrated in protocols 2 and 3, promote the creation of finer, more uniformly dispersed dispersoids by reducing diffusivity and limiting particle development. This investigation emphasizes the precise balance necessary in homogenisation methods to obtain the desired microstructural features.

4.1.2 Composition of dispersoids

The investigation of dispersoid composition was started to better understand the effects of different homogenisation techniques on elements distribution inside the particles. Homogenisation encourages the formation of dispersoids, and temperature and soaking duration determine their composition.

The results from homogenisation protocol 1 are presented in detail to demonstrate the methodology used to analyse dispersoid composition. This method enables a step-by-step illustration of how the linescan analysis was performed, adding clarity to the process. The same methodology was used on samples from all homogenisation processes to ensure consistency in the analysis.

To find locations containing dispersoids, the microstructure was first imaged using SEM. Figure 4.2 are SEM images of the protocol 1 sample, highlighting locations where dispersoids were clearly visible and abundant. These regions were chosen for their distinct morphology and visibility within the microstructure.

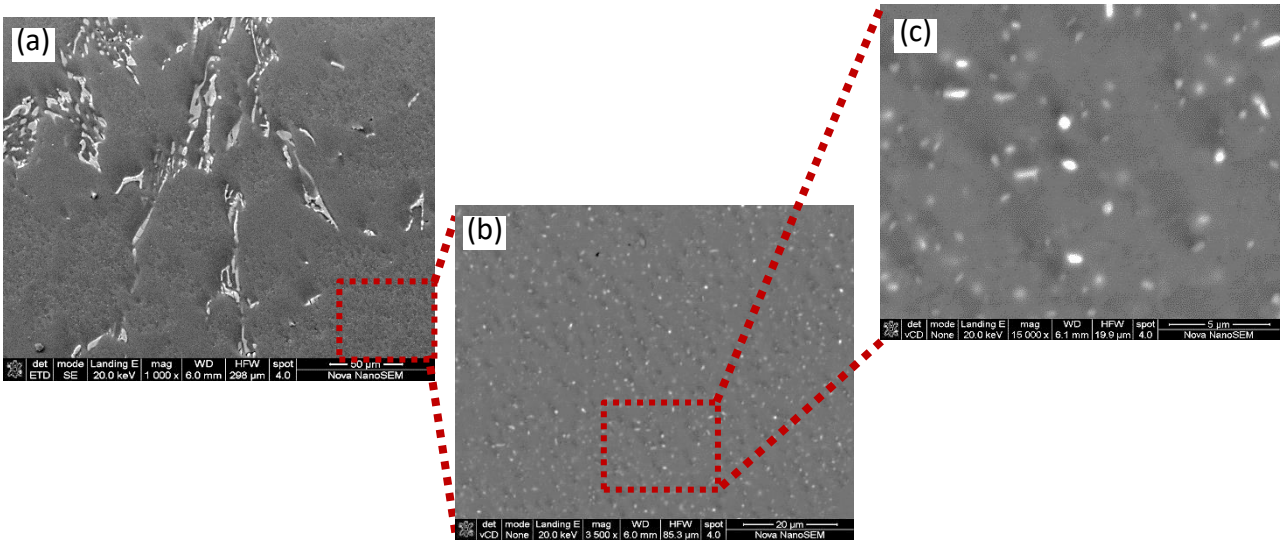

Figure 4.2. SEM micrographs of homogenisation protocol 1 sample. (a) Secondary electron image showing IMPs and area with dispersoids highlighted. (b) Backscatter image of projection of the area highlighted in (a). (c) Backscatter image projecting highlighted area in (b).

Elemental mapping was then performed with SEM-EDS to validate the presence of essential elements in the dispersoids. Figure 4.3 shows the elemental maps of Mn and Si overlaid over the dispersoids to establish their elemental composition. Figure 4.3 (b) and (c) demonstrate the presence of Si and Mn in the highlighted dispersoids in Figure 4.3 (a). This mapping step indicated the poor resolution of the mapping approach for this work, owing to the small dispersoid sizes and the limited resolution of the equipment. Additionally there are no quantitative aspects to this approach. Thus, a linescan approach was necessary.

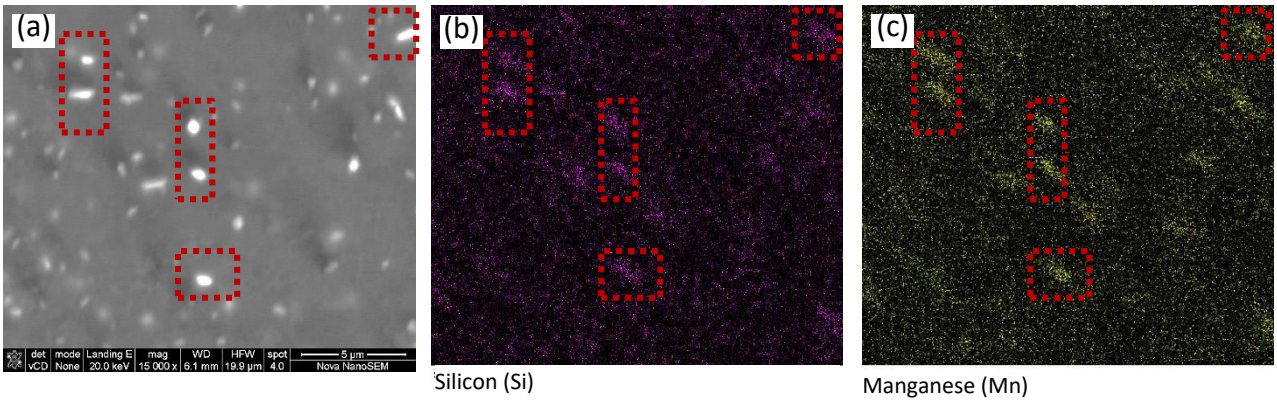

Figure 4.3. (a) SEM Backscatter micrograph showing dispersoids. (b) SEM-EDS elemental analysis map of Si in map area in (a). SEM-EDS elemental analysis map of Mn in map area in (a).

A EDS linescan was then performed to investigate the variances in elemental composition along a line through the matrix and across individual dispersoids. Figure 4.4 shows the results for

homogenisation practice 1, which is the highest temperature homogenisation. Figure 4.4 (a) shows a backscatter image (BSE), with the linescan route highlighted as a red dotted line that crosses the dispersoids.. Figure 4.4 (b) shows the resulting elemental profile, which includes peaks for Mn, Si, and Fe. For a clearer visualisation, the curves of the element's composition were superimposed onto the BSE image. The trace illustrates changes in composition linked to the location of the crossed over dispersoids. The intensity of counts is interpreted as an indication of relative ratio of solute elements within the dispersoid, supporting the phase identification as α-Al(Mn,Fe)Si. The Mn and Si dominance, together with little Fe, is consistent with expected phase development under the given conditions with reference to the trends discussed by Alexander and Greer [19]. The compositional gradients indicated in the trace may result from resolution and interaction volume errors from the technique. TEM analysis would allow for a more quantitative assessment but was outside the scope of this work.

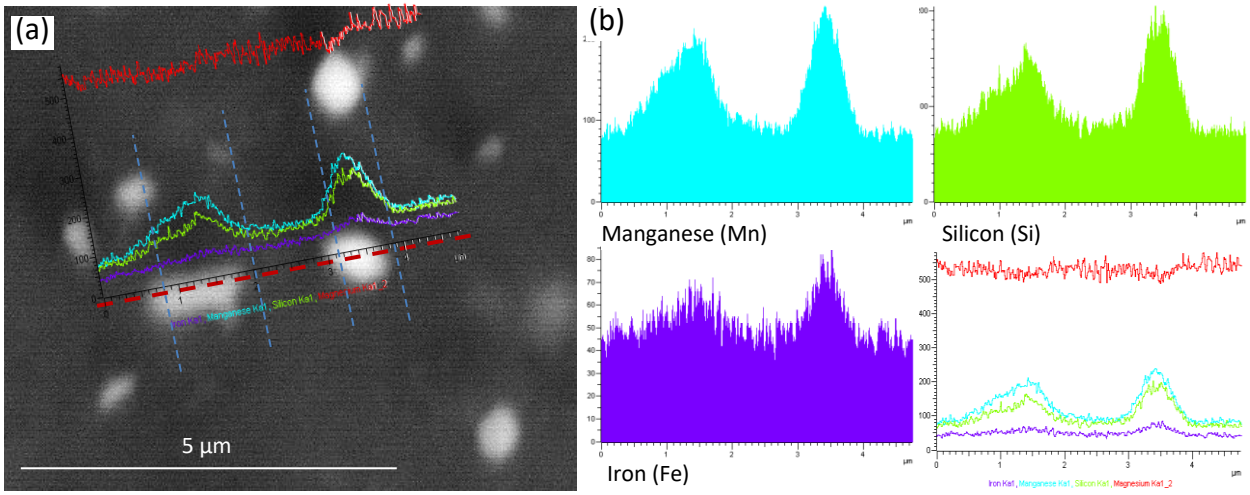

*Figure 4.4. SEM-EDS (a) linescan over dispersoids of a **homogenisation protocol 1** sample and (b) the elemental analysis of Mn, Si and Fe in crossed over dispersoids.*

In the linescan in Figure 4.5 for homogenisation practice 2, there is an observation of distinct peaks for Mn and Si, as well as a modest counts of Fe. These findings suggest that the dispersoids contain considerable amounts of Mn and Si consistent with the creation of α-Al(Mn,Fe)Si-type dispersoids. The dispersoid sizes are smaller than those in Figure 4.4 for homogenisation practice 1, which is the highest temperature practice. These smaller dispersoids are more difficult to resolve using the SEM and thus the clarity and indexing of the EDS is reduced.

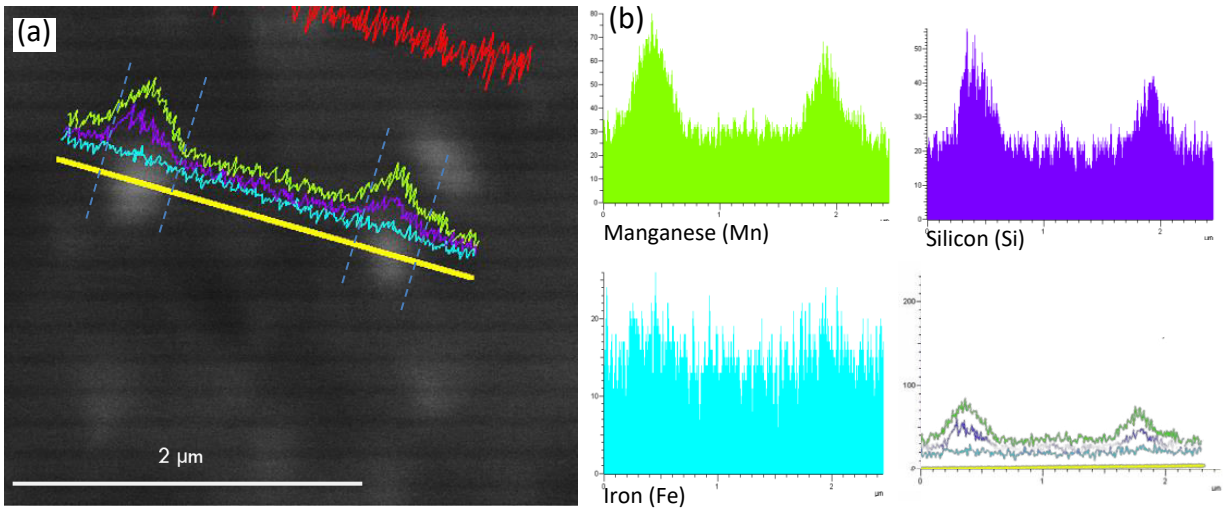

*Figure 4.5. SEM-EDS (a) linescan over dispersoids of a **homogenisation protocol 2** sample and (b) the elemental analysis of Mn, Si and Fe in crossed over dispersoids.*

In Figure 4.6, the linescan profiles for homogenisation practice 3, the lowest temperature homogenisation. The linescan traces show peaks for Mn and Si, as well as a relatively weaker presence of Fe. The dispersoids in this image appear smaller and the resolution of the dispersoids is limited owing to their size. However, they are large enough that they can be identified. The intensity profiles exhibit less marked compositional gradients, which may suggests a greater matrix influence due to smaller size of dispersoids. The very uniform distribution of Mn and Si inside these dispersoids suggests a stable α-Al(Mn,Fe)Si phase.

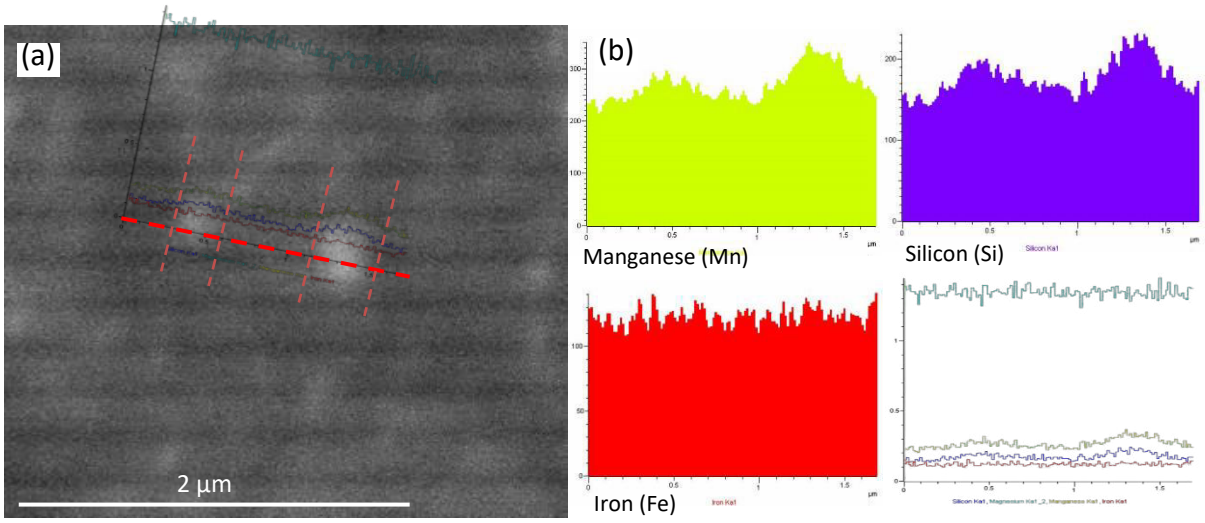

*Figure 4.6. SEM-EDS (a) linescan over dispersoids of a **homogenisation protocol 3** sample and (b) the elemental analysis of Mn, Si and Fe in crossed over dispersoids.*

4.1.3 Size and distribution

The effect varying homogenisation temperatures on the size and distribution of dispersoids within the matrix was studied on the samples prior to the hot rough rolling process. Dispersoids pay an important role in impeding the grain boundary migration by the Zener drag mechanism. Three micrographs for each homogenisation process were taken for investigation of the size and distribution. Effect of 520°C homogenisation in Figure 4.7 (c) indicates the highest number density distribution of dispersoids than 600°C/520°C and 560°C/520°C homogenisation shown in Figure 4.7 (b) and (c) respectively. This is summarised in Table 15. The particle size analysis based on their radii shows the highest mean particle radius in 600°C/520°C homogenisation at 0.127 µm, with a right-skewed distribution in the 0.035 – 0.43 µm shown in Figure 4.9 (a). The average particle radius in 560°C/520°C homogenisation was 0.104 µm within a right-skewed distribution 0.035 – 0.335 µm radius range as demonstrated by Figure 4.9 (b). 520°C homogenisation had the highest number density of particle per μm^2 of 55.92 but the smallest average particle radius of 0.056 µm. This average particle size is within in the 0.035 – 0.21 µm range.

The high number density of the 520°C homogenisation proves that the dispersoids nucleation was dominant at a temperature where the Mn solubility was low. The 600°C/520°C and 560°C/520°C homogenisations showed promotion of particle coarsening and Ostwald ripening resulting smaller number densities as the smaller particles dissolved or grew into larger particles [22]. The right-skewed distributions of the particle sizes across all the homogenisation indicates that most particles were small, but a subset of the particles coarsened during the initial higher homogenisation temperatures. The wide size range and greater average particle size observed in 600°C/520°C homogenisation suggests accelerated coarsening mechanism due to improved atomic diffusion at elevated temperatures [65]. The bimodal size distribution supports the formation of smaller dispersoids from the decrease in temperature in the second step of the homogenisation where there is reduced Mn solubility at this temperature, resulting in further Mn precipitation on existing dispersoids (adding to their size), and additionally forming new dispersoids that are a lot smaller within the structure.

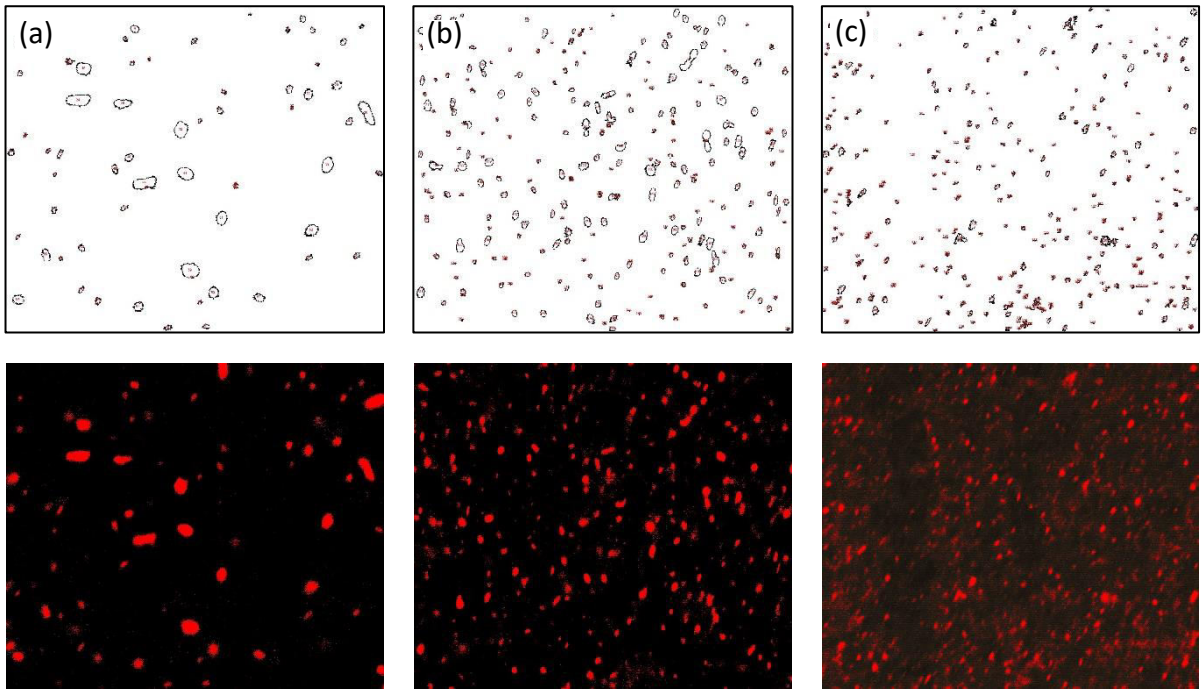

Figure 4.7. Particle analysis (top) and threshold images (bottom) of dispersoids at 15000X magnification (a) homogenisation 1 (b) homogenisation 2 (c) homogenisation 3.

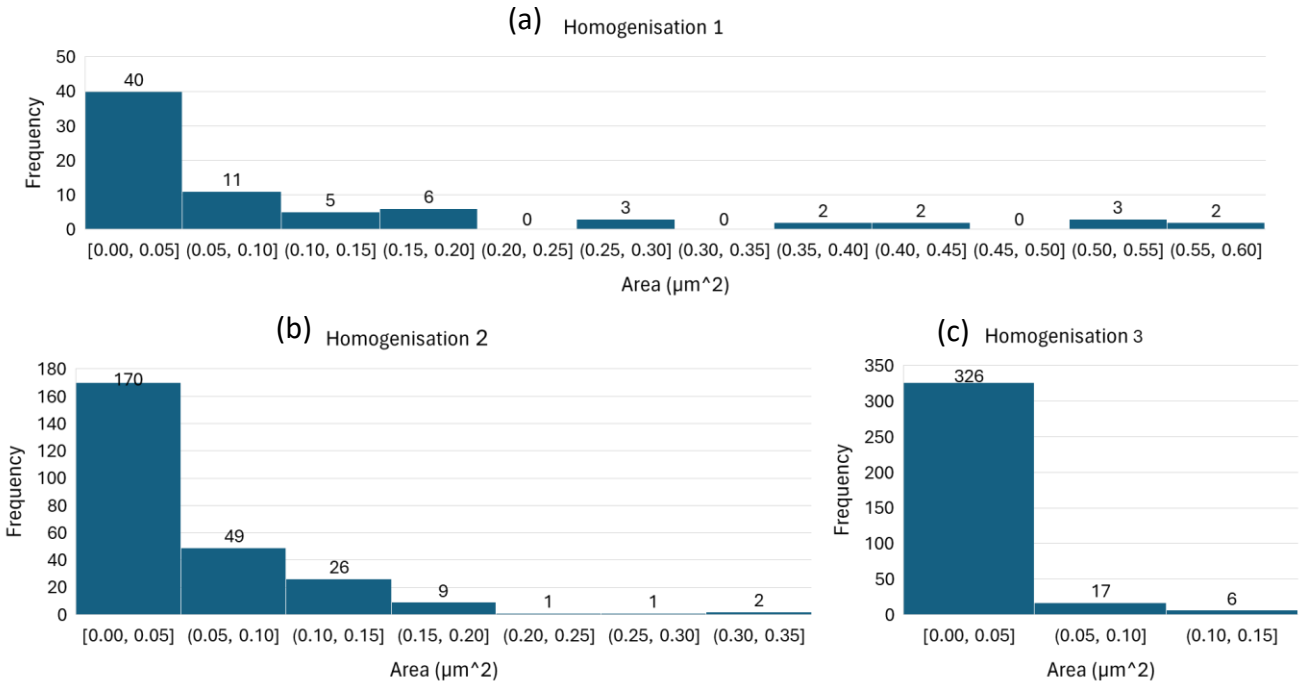

Figure 4.8. Area histograms of dispersoids at 15000X magnification (a) homogenisation 1 (b) homogenisation 2 (c) homogenisation 3.

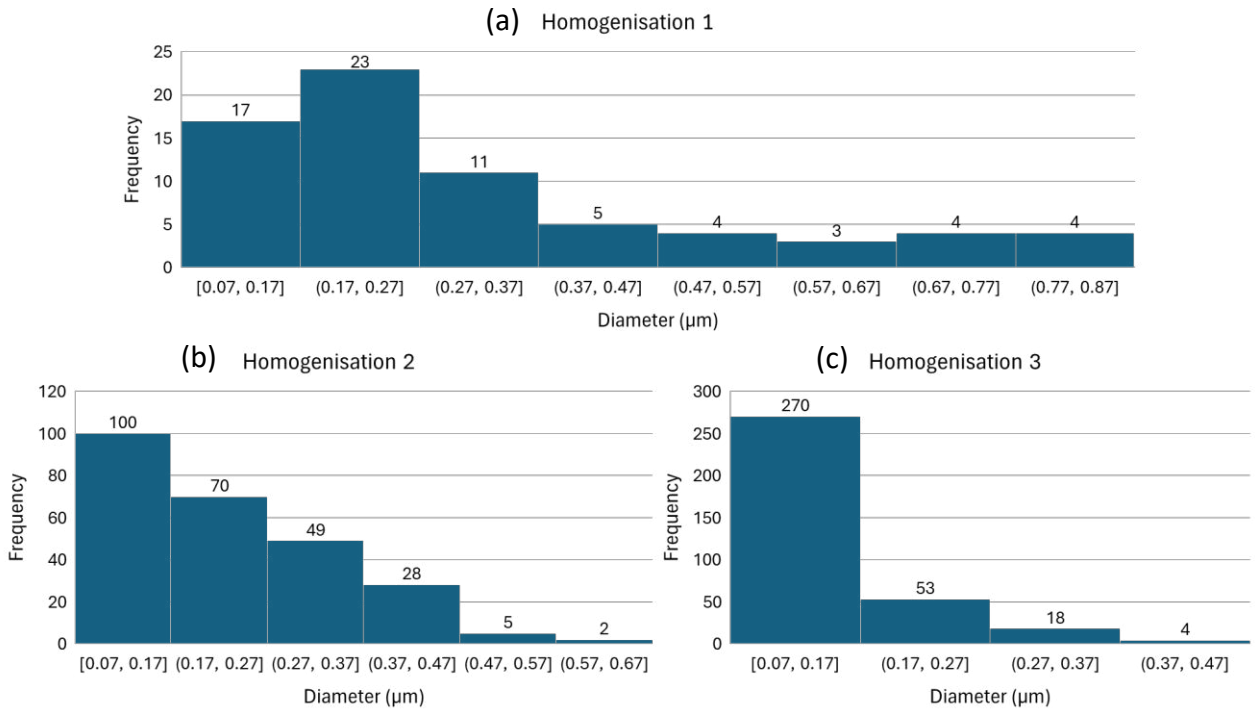

Figure 4.9. Diameter histograms of dispersoids at 15000X magnification (a) homogenisation 1 (b) homogenisation 2 (c) homogenisation 3.

The characteristics of dispersoids are important because they affect Zener pinning potential. Smaller dispersoids increase the Zener pinning pressure, which prevents recrystallisation when it is meant to happen later in the process. As a result, high Zener pinning pressure suppresses both recrystallisation and grain expansion by counteracting the driving force for recrystallisation and impeding grain boundary migration.

A simple Zener drag or pinning pressure expression:

$$P_z = \frac{3\gamma F_v}{2r} \qquad (2)$$

was manipulate to:

$$\frac{P_z}{\gamma} = \frac{3F_v}{2r} \qquad (3)$$

to determine the normalised pinning pressure associated with the homogenisations where F_v is the volume fraction of dispersed particles, r is the particle radius and γ is the energy of the grain boundary that the dispersed particles are pinning.

Smaller size particles are expected to provide higher pinning pressure and an increase in area fraction is related to more pinning meaning higher resistance to recrystallisation. Homogenisation 3 had smaller average particle size than homogenisation 1 which resulted in higher normalised

pinning pressure and the high number density of homogenisation 1 meant higher Zener drag as studied by [4]. However, lower pinning pressure despite the higher area fraction value of homogenisation 1 when compared to homogenisation 3, indicates particles coarsening, resulting in reduced number density.

On the contrary, homogenisation 2 has larger particle size, lower number density, higher area fraction than homogenisation 3 but the resulting pinning pressure is greater for homogenisation 2. This indicates that homogenisation 2 had coarsened particles, possibly because of Ostwald ripening, which provided effective pining of the grain boundaries due to their size and coverage [23].

Table 15. Particle radii and area fractions, and normalised Zener pinning pressure values for the homogenised samples.

	Average particle radius (um)	**Number density of particles per um^2**	**Area fraction of particles**	**Normalised pinning pressure ($\frac{P_z}{\gamma}$) (%)**
Homogenisation 1 600°C /520°C	0.127	8.93	0.023	0.0272
Homogenisation 2 560°C /520°C	0.104	19.85	0.039	0.0558
Homogenisation 3 520°C	0.056	55.92	0.019	0.0493

4.2 Characterisation of Intermetallic particles

Heat-treating AA3104 material results in the modification of the particle morphology by breaking up the networks between the IMPs. In Figure 4.10 (a), the as-cast matrix exhibits elongated, coarse, irregular, highly interconnected IMPs. The continuous networks indicate an absence of heat treatment to promote phase change on the particles. Figure 4.10 (b) displays partial spheroidization and coarsening of the IMPs. Compared to as-cast, there is evidence of fragmentation of the larger intermetallic phases leading to smaller and more uniformly distributed particles. However, the elongated morphology and interconnectivity are still retained by some particles. In Figure 4.10 (c), there is a noticeable reduction in the interconnectivity of the IMPs. Figure 4.10 (c) reveals refined, isolated, well-dispersed particles with slight variation in their sizes which could be motivated by the incomplete dissolution at lower soaking times and homogenisation temperatures compared to Figure 4.10 (b). The clustering of the IMPs is seen to have reduced when compared to the as-cast morphology. Figure 4.10 (d) also displays reduced clustering of the IMPs and a reduction in the interconnectivity between them. The observation of interconnected networks in the as-cast condition being broken down into refined and isolated particles in the homogenised samples is

consistent with research by Zhao et al. [13] and Kamat [65]. There is a profound refinement of the particles when compared to the as-cast. Spheroidization is limited when compared to Figure 4.10 (b) where the driving force is the low homogenisation temperature and shorter soaking time.

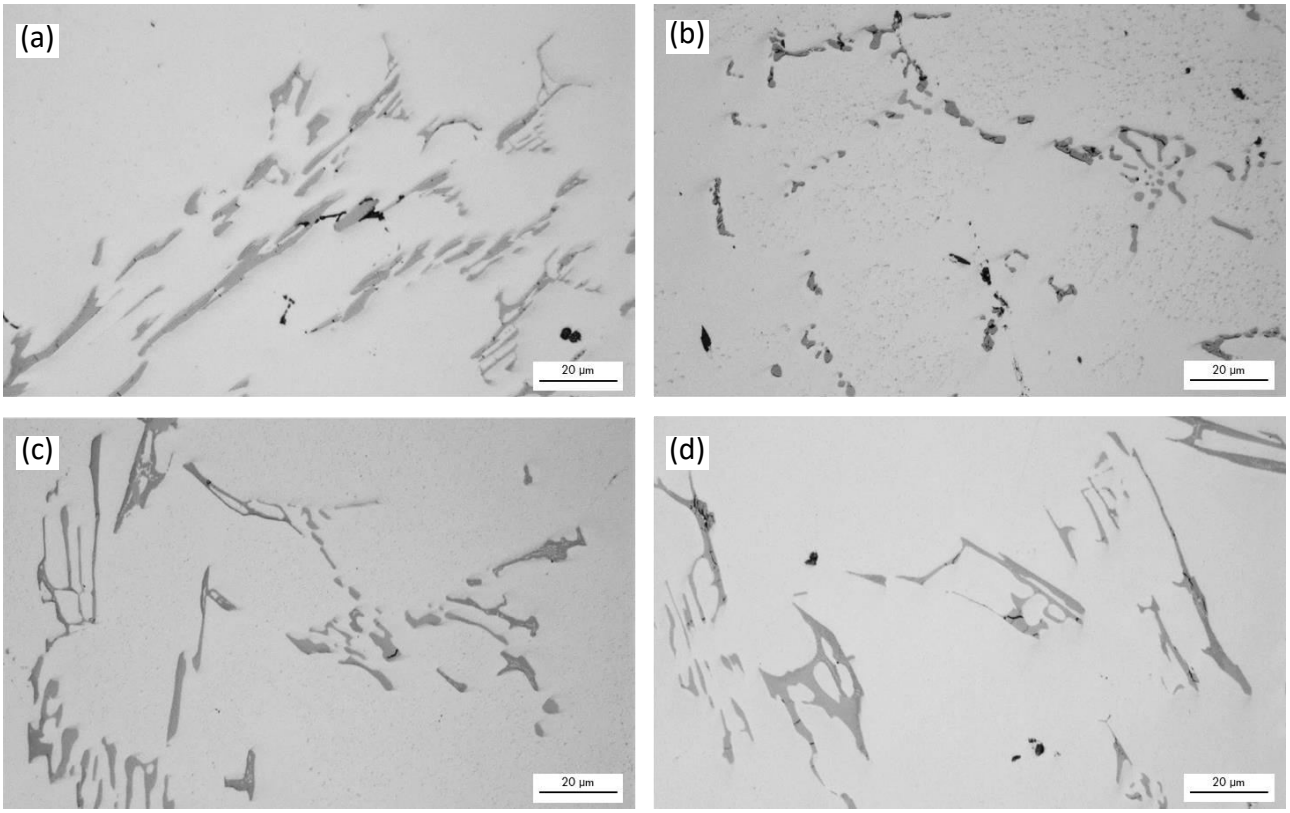

Figure 4.10. Light microscopy images showing the IMPs of as-cast and different homogenisation samples. (a) IMPs in an as-cast sample. (b) IMPs of homogenisation 1 sample. (c) IMPs in homogenisation 2 sample. (d) IMPs in homogenisation 3 sample.

4.2.1 Composition of intermetallic particles

The main components found in the IMPs of the as-cast sample are displayed in Figure 4.11. Figure 4.11 (b), (c), and (e) of the EDS maps demonstrate the high concentration of Fe, Mn, and aluminium in the IMPs indicating their significant role in their formation. However, at this point, there is not much Si present in the IMPs, as seen in Figure 4.11 (d). This implies that the particles are primarily composed of the Si-free β-Al_6(Fe,Mn) phase. Therefore, the most common phase that forms during casting is β. The EDS maps also reveal a concentration of Mg, which is not included in the results since it is widely distributed in the matrix, implying that the presence of Mg_2Si intermetallic compound was difficult to detect inside the microstructure of homogenised samples [73]. It was easier to resolve Mg_2Si intermetallic compound in as-cast and is shwon in Appendix A. The EDS maps of all the studied elements including Mg are in Appendix A.

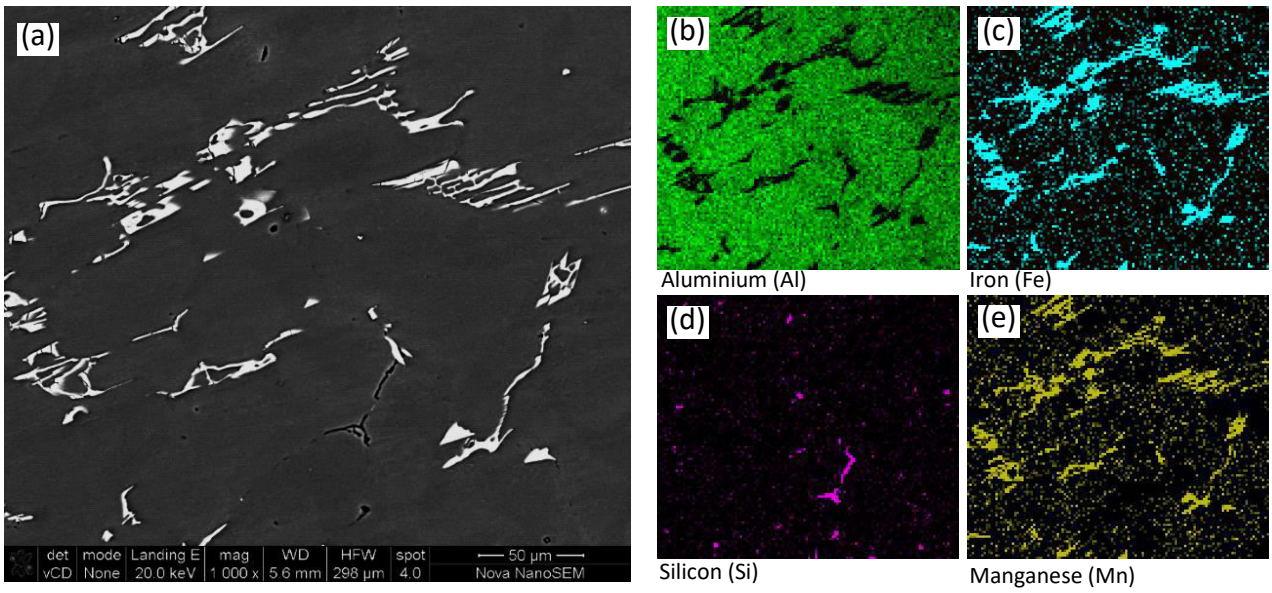

Figure 4.11. SEM Secondary electron micrograph, coupled with EDS maps, highlighting the major elements present in the IMPs for as-cast sample. (a) Secondary electron image. (b) Aluminium elemental composition map. (c) Fe elemental composition map. (d) Si elemental composition map. (e) Mn elemental composition map.

Several microstructural changes occur during the homogenisation process of AA3104, including phase transitions, reduced microsegregation, and redistribution of Mn from the solid solution to coarse particles and dispersoids. Additionally, Mg_2Si particles are dissolved. Homogenisation converts some of the β-Al_6(Fe,Mn) phase, depending on temperature and Si content, to the harder α-Al_x(Fe,Mn)$_3Si_2$ phase. After homogenisation, the AA3104 microstructure comprises primarily of α-Al_x(Fe,Mn)$_3Si_2$ and β-Al_6(Fe,Mn) particles. As the homogenisation temperature rises, Mg_2Si particles dissolve and release Si. Si from particles and as-cast solution diffuses into β-phase particles and promotes further phase transition.

Figure 4.11 showed no apparent evidence of Si within the IMPs, implying a low presence in the as-cast condition. However, Figure 4.12 shows Si inclusion into the particles, as demonstrated by the yellow highlighting in Figure 4.12 (a) and Figure 4.12 (d). This observation confirms the presence of the α-Al_x(Fe,Mn)$_3Si_2$ phase following 600°C/520°C homogenisation.

Furthermore, the areas shown in red in Figure 4.12 denote Si rich zones or solitary Si spots inside the microstructure. In contrast, the blue-highlighted zones are IMPs made up of aluminium, Mn, and Fe but not Si. The blue zones show the β-Al_6(Fe,Mn) phase, which is Si-deficient. When homogenised samples have a higher Si concentration, the β-to-α phase transition occurs, and this transition to α-Al_x(Fe,Mn)$_3Si_2$ phase development is consistent with previous research [23] [22].

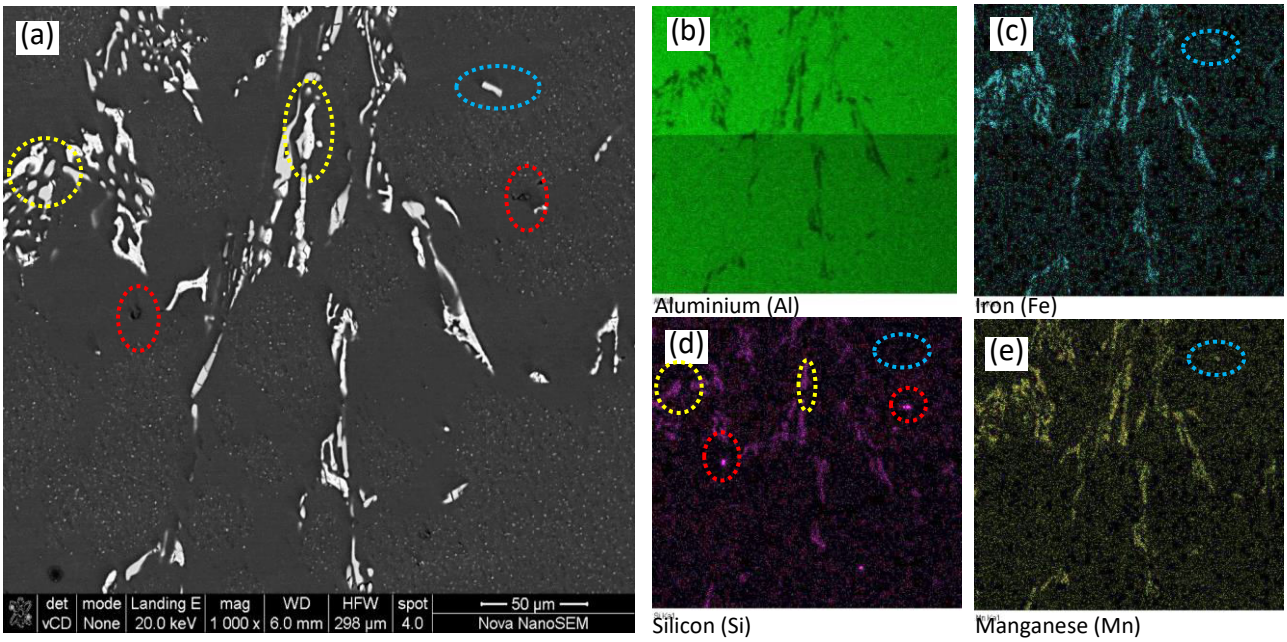

Figure 4.12. SEM Secondary electron micrograph, coupled with EDS maps, highlighting the major elements present in the IMPs for homogenisation 1 sample. (a) Secondary electron image. (b) Aluminium elemental composition map. (c) Fe elemental composition map. (d) Si elemental composition map. (e) Mn elemental composition map.

Figure 4.13 (d) shows a rise in Si concentration within IMPs, indicating a phase transition from the β-phase to the α-phase following homogenisation at 560°C/520°C. This transition is clearly seen by the more intense magenta shading in the Si element map, as opposed to the as-cast condition shown in Figure 4.11 (d), which only shows faint traces of magenta. The increased magenta colouring reveals the redistribution and enrichment of Si after homogenisation.

Figure 4.13 (a) and Figure 4.13 (d) show how β-phase particles, indicated in blue, become less prominent as homogenisation continues. At the same time, the increased Si incorporation makes the yellow-highlighted IMPs that belong to the α-phase more visible. The presence of these yellow-shaded α-phase particles highlights the importance of high temperatures in facilitating Si dispersion and phase development by reflecting the transformation caused by homogenisation.

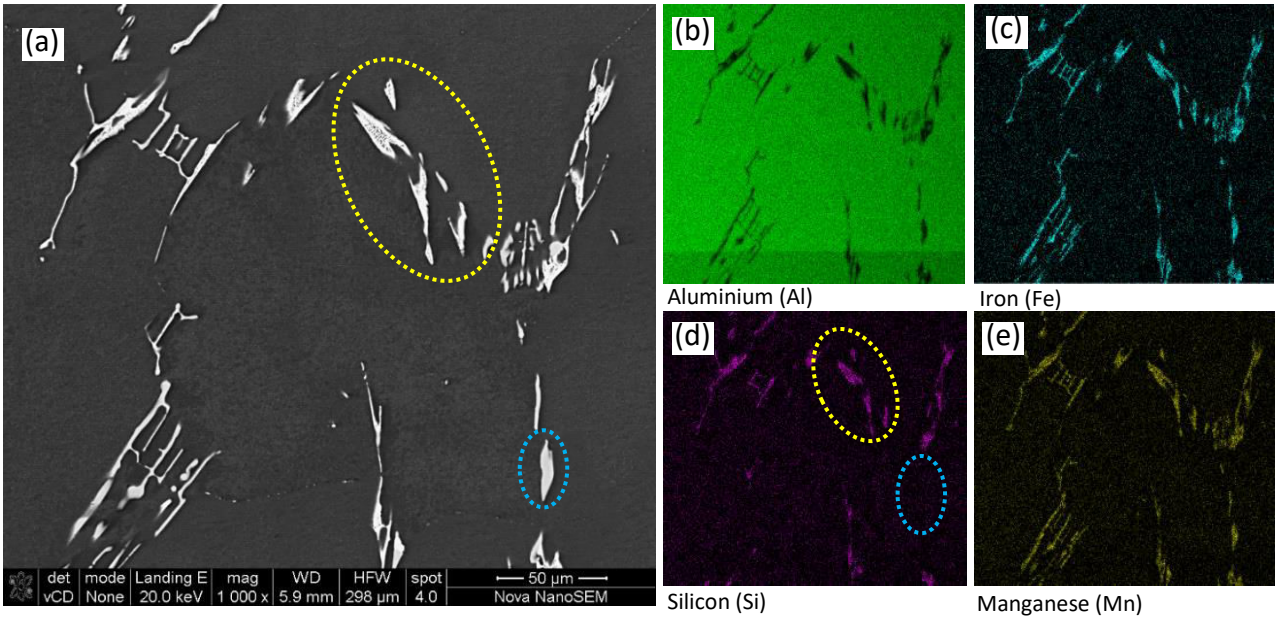

Figure 4.13. SEM Secondary electron micrograph, coupled with EDS maps, highlighting the major elements present in the IMPs for homogenisation 2 sample. (a) Secondary electron image. (b) Aluminium elemental composition map. (c) Fe elemental composition map. (d) Si elemental composition map. (e) Mn elemental composition map.

Figure 4.14 (d) shows a considerable rise in Si concentration within IMPs during homogenisation at 520°C, indicating a distinct phase transition from the β-phase to the α-phase. The enhanced magenta hue in the Si element map supports this transition, as it contrasts sharply with the as-cast condition map shown in Figure 4.11 (d), which shows just minor traces of magenta. The increased magenta colouring suggests that Si has been redistributed and incorporated inside the IMPs because of the homogenisation process.

In Figure 4.14 (a) and Figure 4.14 (d), where β-phase particles are indicated in blue and seem to decrease as the homogenisation process advances. At the same time, the Si-rich α-phase forms, which is represented by the IMPs that are highlighted in yellow, highlighting the chemical change within the microstructure. This transition highlights how homogenisation at 520°C aids in Si diffusion and the formation of the α-phase, which significantly changes the phase composition of the alloy.

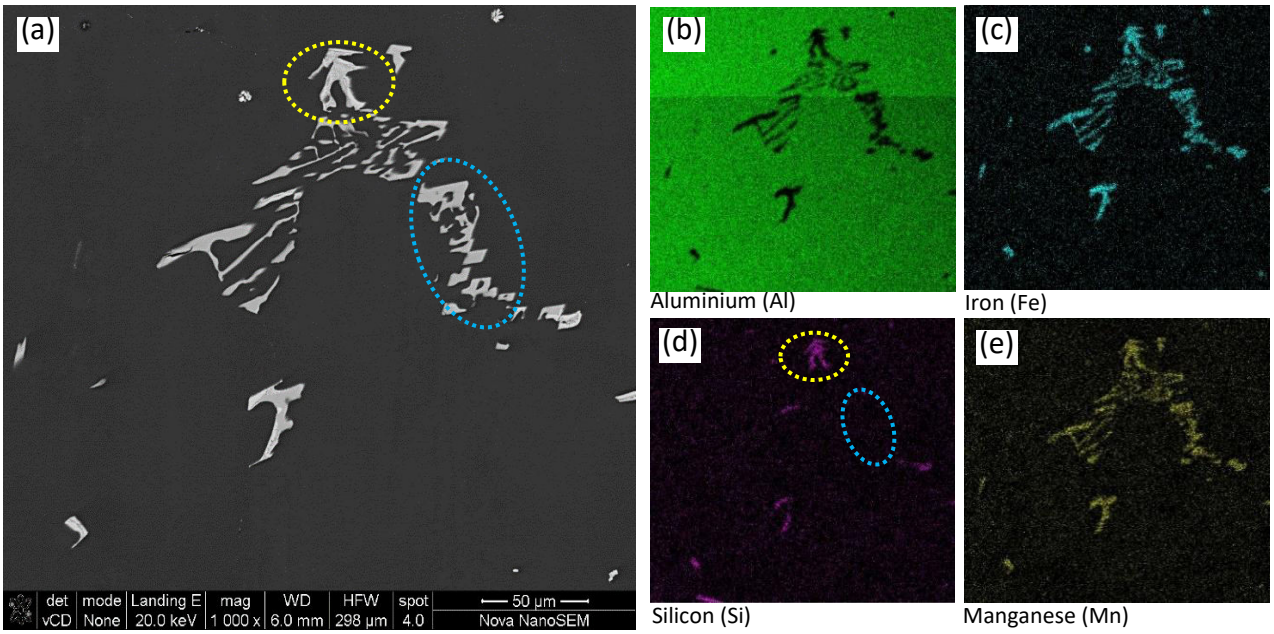

Figure 4.14. SEM Secondary electron micrograph, coupled with EDS maps, highlighting the major elements present in the IMPs for homogenisation 3 sample. (a) Secondary electron image. (b) Aluminium elemental composition map. (c) Fe elemental composition map. (d) Si elemental composition map. (e) Mn elemental composition map.

4.3 Plane strain compression

The raw data recorded for each PSC test includes time, force, jaw displacement, thermocouple temperatures, stroke and wedge positions, heat power, stress, and strain. While not all data was required for analysis, it provided insights into test performance and helped troubleshoot when tests varied from expectations. The raw data was processed using a Python package for parameterising materials test data, Paramaterial [74]. The testing parameters are shown in Table 12 in the previous chapter.

Throughout the PSC tests, the sample's heating rate and holding temperature for deformation were effectively maintained at the nominal input values. Figure 4.15 shows an example of a temperature curve from one of the PSC tests. This profile follows the hot rolling simulation in Figure 3.11. Appendix B shows the temperature profiles for all of the PSC testing.

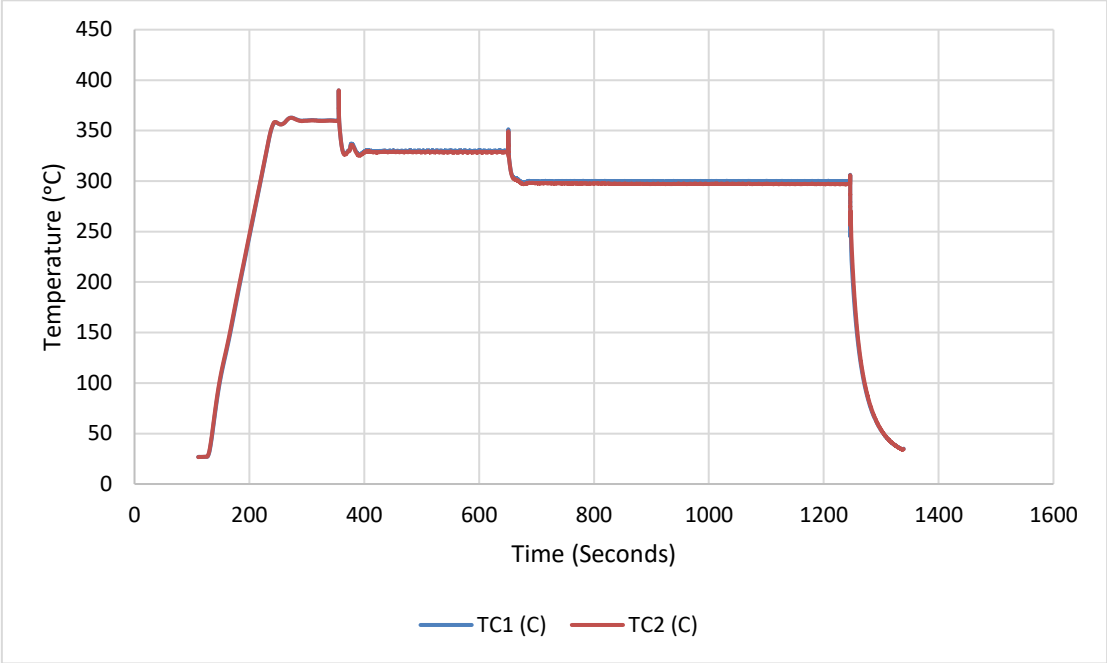

Figure 4.15. Temperature profile of a sample exposed to full hot finish rolling simulation.

4.3.1 Stress-strain analysis

Figure 4.16 shows the stress-strain curves for AA3104 samples exposed to various homogenisation methods as well as the as-cast condition. The individual hits are projected in Figure 4.16 (b), Figure 4.16 (c), and Figure 4.16 (d). The flow stress curves have not been corrected for friction, and as such the shape of the curves shows in increasing gradient after yielding, where there should be a steady state flow stress. The individual hits' error bars are shown in Figure 4.17 to highlight the variability in the results. Stress-strain curves produced during PSC tests revealed several phases of deformation, including the initial elastic zone followed by significant plastic deformation. The highest stress reported on the first hit step ranged from 136 to 148 MPa. The second hit produced stress in the 201-210 MPa range. The third hit was found to be within the 337-358 MPa stress range. The use of error bars emphasises the significance of variability in material testing but also highlight the similarity in the ranges of the flow stress for the successive passes, regardless of homogenisation practice.

The flow stress values for homogenisation practice 3, where the dispersoids are very small and the IMPs are large and show some phase transformation from the β to α phases, consistently has the lowest value. While the as-cast sample has a slightly higher value in pass 2 and 3. There is minimal difference in IMP structures between the two, and minimal flow stress difference, indicating that the dispersoids are offering minimal strengthening contributions during high temperature

deformation. When looking at the flow stress of homogenisation practice 1 and 2, where the IMP structures exhibit greater changes, after pass 3 the strain accumulation is higher, and the strengthening contribution is larger. If the premise that dispersoids do not offer strengthening contributions is correct here, then the strength is attributed to the topology (morphology and distribution) of the IMPs as the major contributor. While this may be true, the results show very little difference between them, and as such further testing should be performed to achieve statistically meaningful results upon which to interrogate differences.

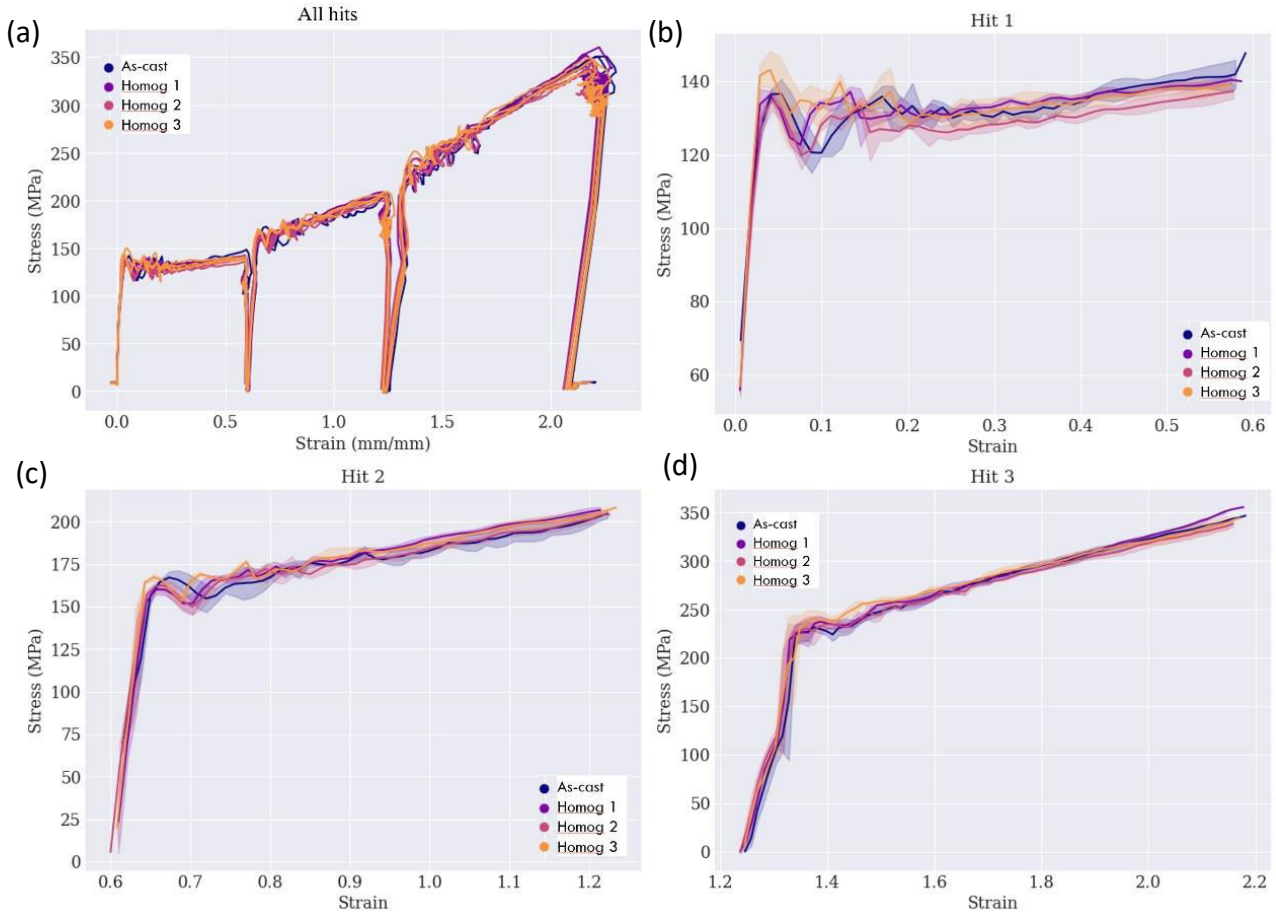

Figure 4.16. Stress-strain diagram from the PSC simulation of the four samples showing (a) all hits imposed on the samples (b) projected hit 1 (c) projected hit 2 (d) projected hit 3

Legend	Temp 1 (Soak time)	Temp 2 (Soak time)
Homog 1	600°C (8hrs)	520°C (4hrs)
Homog 2	560°C (4hrs)	520°C (4hrs)
Homog 3	520°C (4hrs)	-
As-cast	-	-

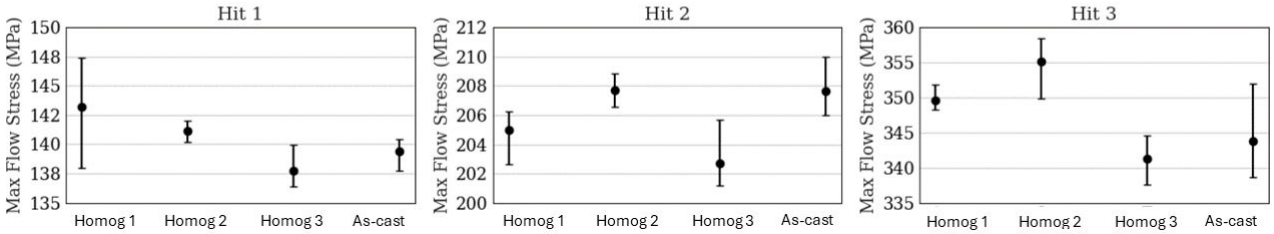

Figure 4.17. Individual hits of the PSC simulation with error bars

4.4 Recrystallised grain size and Texture

The EBSD analysis was performed , using ATEX software, on the variation of recrystallised grain sizes of differently homogenised AA3104 samples after recrystallisation annealing. The microstructural evolution during homogenisation significantly affects grain size and recrystallised fraction during subsequent deformation and heat treatment process. The EBSD maps are shown in Figure 4.18. The maps illustrate the high angle grain boundaries (HAGBs) in solid black lines, which are associated with recrystallised grains in cases where no internal low angle grain boundaries (LAGBs), which are shown in grey, are located. The grains are coloured according to grain size, with the smallest grains coloured as light blue and the largest coloured through yellow and orange, up to red. The grain sizes in Figure 4.18 (a) for the 600°C/520°C homogenisation, show bi-modal grain size distribution, with the larger average grains being approximately 15-20 µm in diameter. While in Figure 4.18 (b) for 560°C/520°C homogenisation has the largest recrystallised grain sizes present within the structure when compared to the others. The distribution shows a wide range of grains, but there are many grains of the order of 25-35 µm in diameter, and some up to 45 µm in diameter. In Figure 4.1 (b), the coarsest dispersoids were observed in 600°C/520°C homogenisation, which corresponds to the smallest recrystallised grain in this study. Again, in Figure 4.1 (c), fine, small and closely spaced dispersoids were observed for 560°C/520°C homogenisation and the resulting recrystallised grains in Figure 4.18 (b) are the largest of the three homogenisation protocols. This confirms the study by Doherty and Martin [42] who demonstrated that coarse, broadly scattered precipitates can accelerate recrystallisation but the fine, closely spaced precipitates can slow down recrystallisation.

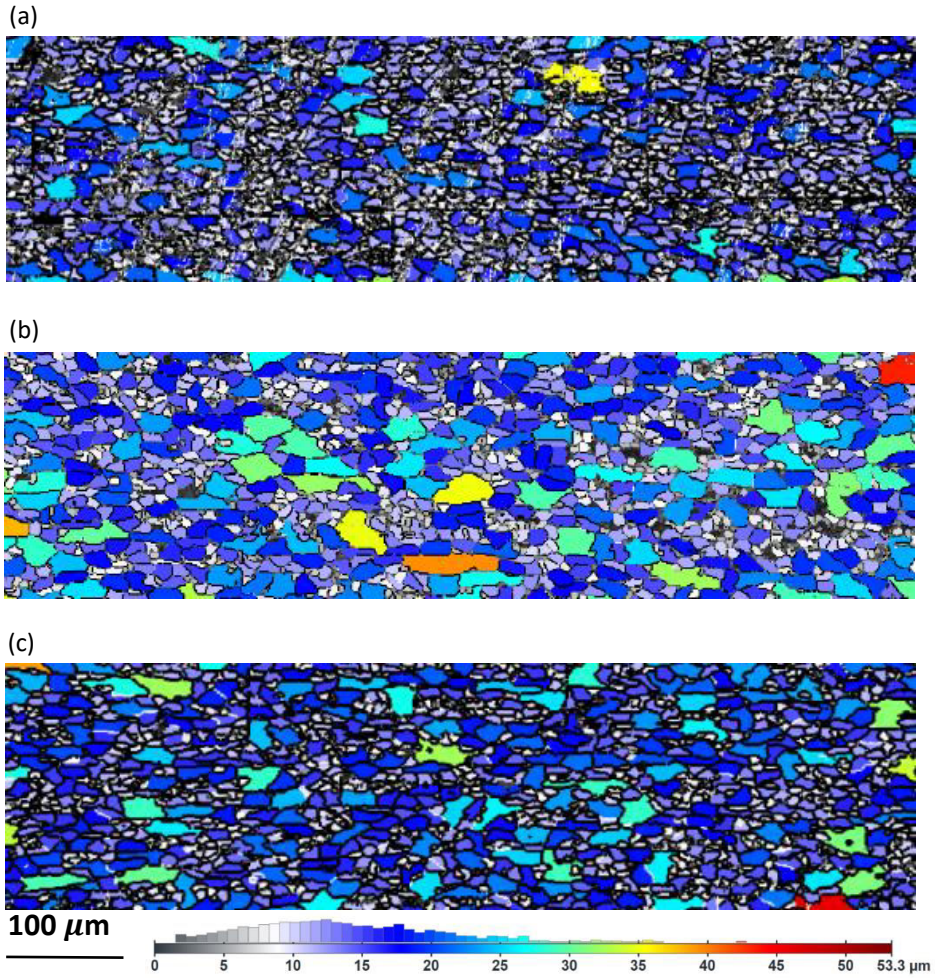

Figure 4.18. EBSD images of grain structures of samples (a)homogenisation 1: 600°C/520°C (b)homogenisation 2: 560°C/520°C (c) homogenisation 3: 520°C after PSC and recrystallisation annealing.

As demonstrated by Table 16, Figure 4.19, Figure 4.20, and Figure 4.21, the as-cast sample after PSC and recrystallisation annealing has the most significant deformation textures, which are characterised by Brass (Bs), Copper (Cu), and Shear (S) components, with intensities of Bs (8.62), Cu (9.17), and S (21.00) reflecting the extensively deformed microstructure. These components result from high stacking fault energy (SFE), which favours dislocation slip as the predominant deformation process. These high values suggest a strong rolling texture in the absence of annealing or recrystallisation, which is indicative of a strained microstructure [75].

Higginson et al. [59] demonstrated that increasing amounts of the dispersoids were connected to increased cube texture formation at the expense of other texture components. This is consistent with this research as Figure 4.22 (a) shows the least development of the cube component within 600°C/520°C homogenised sample, approximately 4.8, which had the lowest amounts of dispersoids as demonstrated in Figure 4.7 (a) and Figure 4.8 (a). 560°C/520°C homogenised sample showed moderate dispersoids coarsening with relatively uniform distribution. Consequently, the ODF sections in Figure 4.22 (b) shows approximately 7.5 intensity of cube component present within a

560°C/520°C homogenised sample. Large particles typically accelerate recrystallization through PSN, where recrystallisation nuclei form within the deformation zones surrounding these particles. This process leads to a reduced amount of the cube recrystallisation texture, most likely due to the formation of random texture orientations which are typically associated with PSN. However, a detailed assessment of texture mechanisms is outside the scope of this work.

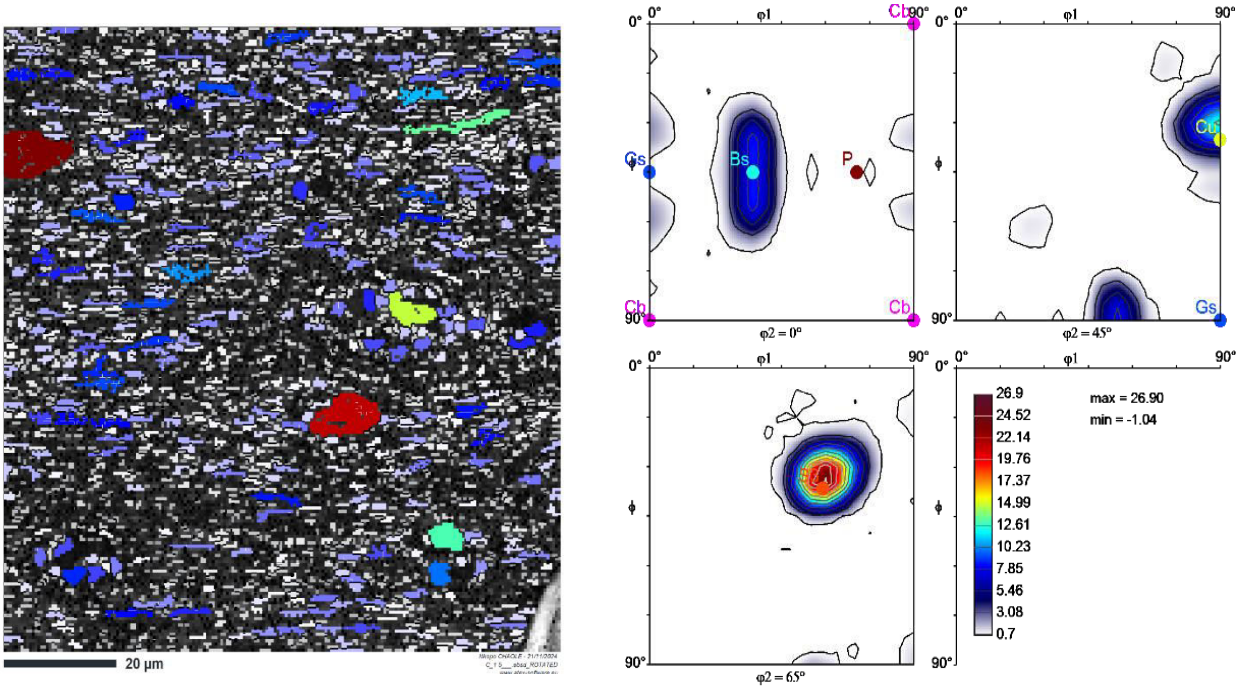

Figure 4.19. EBSD grain size and representative ODF sections of as-cast sample after PSC and recrystallisation annealing, where the structure is partially recrystallised.

Homogenised samples exhibit a significant reduction in deformation texture, emphasising the recrystallisation process [76]. Homogenisation 1 still has moderate deformation texture values (Cu: 1.68, S: 0.25), indicating residual strains from the higher-temperature treatment. Homogenisation 2 has somewhat higher deformation texture components (Cu: 1.86, S: 0.51), which balances strain recovery and recrystallisation. Homogenisation 3 shows reduced deformation textures (Cu: 1.22, S: 0.30), indicating effective strain recovery and due to an increase in random texture, some of which will correspond with deformation textures. However, a detailed assessment of texture mechanisms is outside the scope of this work.

Table 16. Table of intensity of texture components in different samples after recrystallisation anneal.

	Recrystallisation texture components	**Deformation texture components**

	Cb	Gs	P	Cu	S3	Bs
Homogenisation 1	4.86	3.15	1.28	1.68	0.25	0.32
Homogenisation 2	7.50	2.06	1.23	1.86	0.51	0.00
Homogenisation 3	9.04	3.15	1.56	1.22	0.30	0.16
As-cast	0.34	0.09	0.45	9.17	21.00	8.62

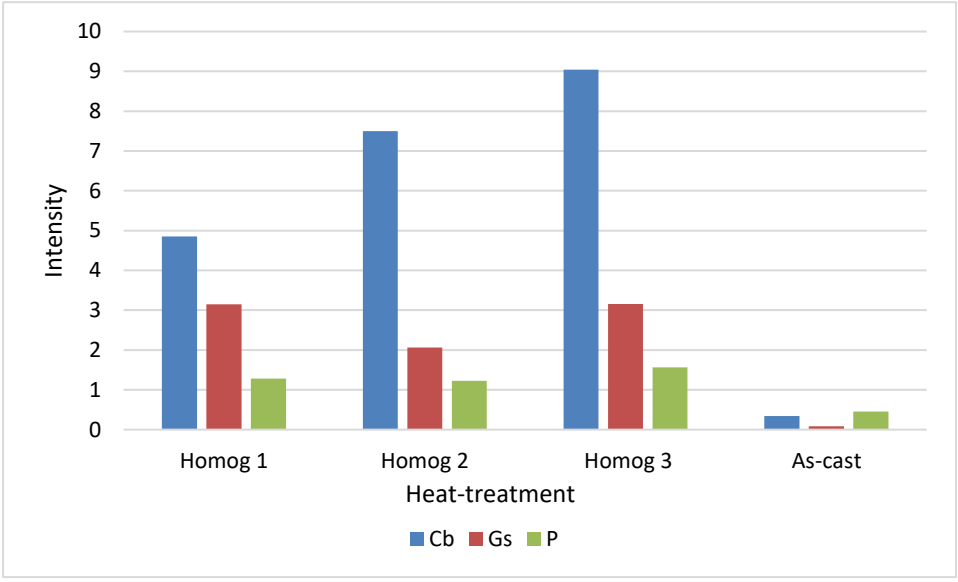

Figure 4.20. Presentation of recrystallisation texture intensities present after recrystallisation annealing, showing the intensity of cube, goss and P components in the different samples

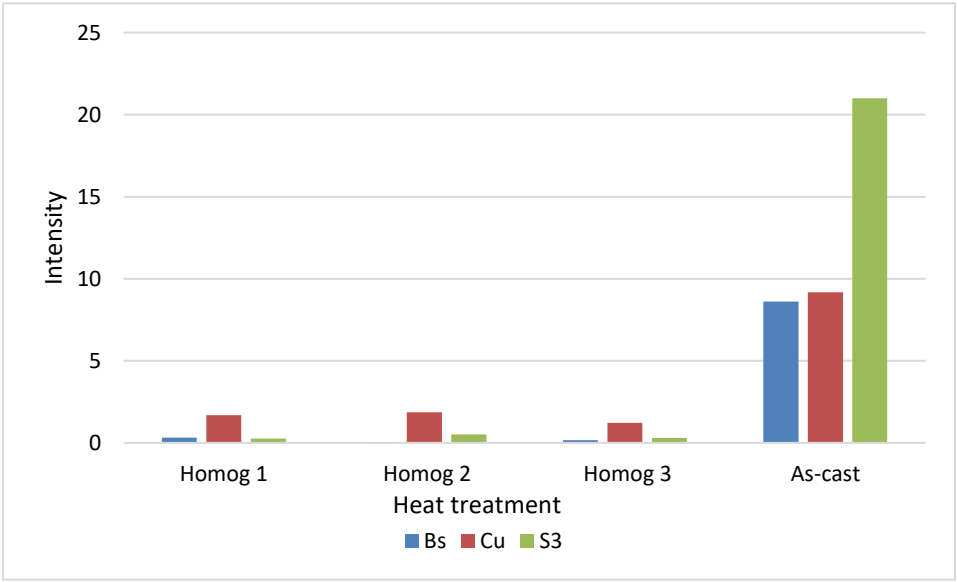

Figure 4.21. Presentation of deformation textures intensities present after recrystallisation annealing, showing the intensity of brass, Cu and S3 components in the different samples.

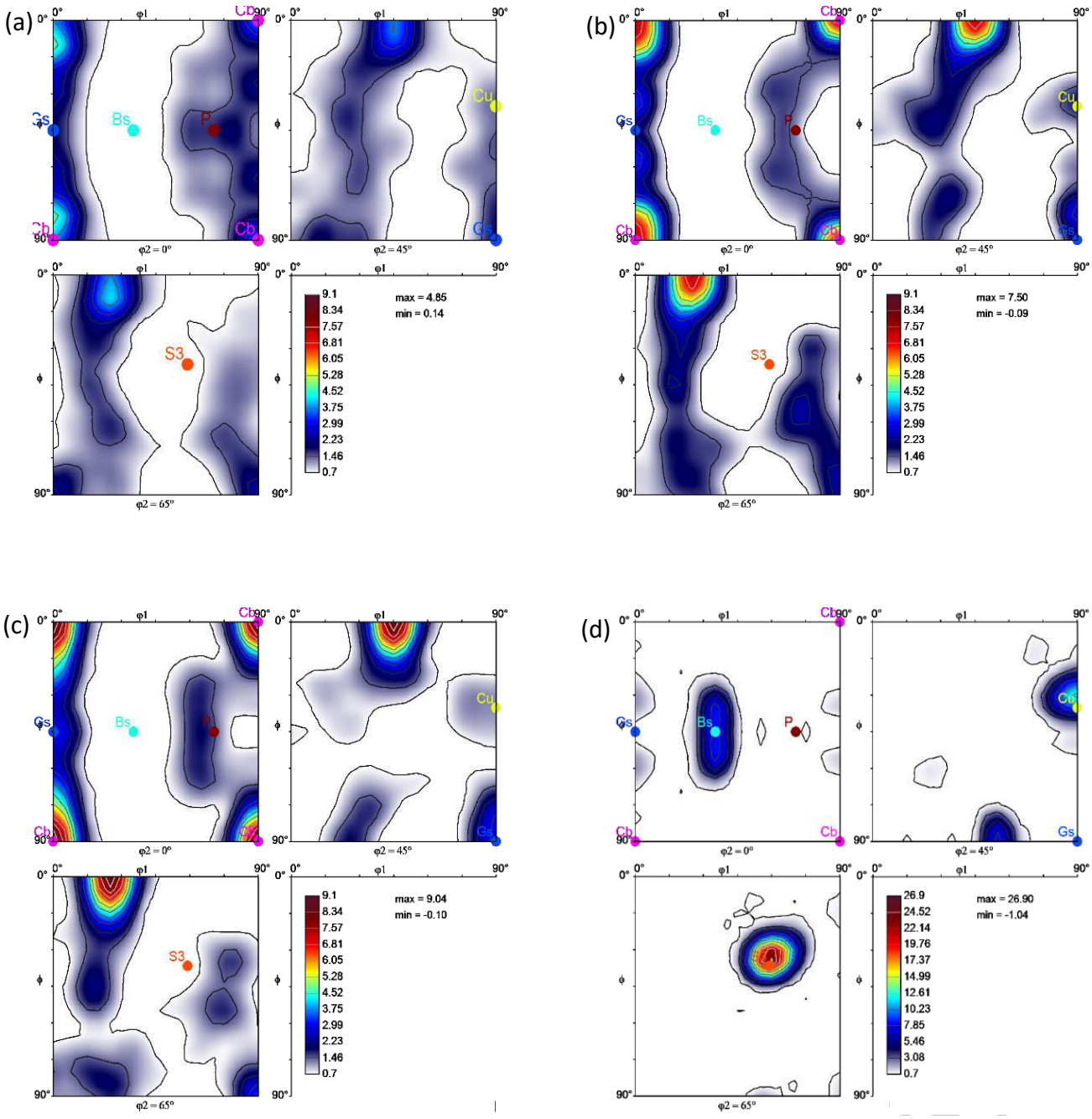

Figure 4.22. Representative ODF sections of samples after PSC and recrystallisation annealing for (a) Homogenisation 1 (b) Homogenisation 2 (c) Homogenisation 3 (d) As-cast.

4.5 Comparison to samples with industry transfer bar prior to PSC testing

A series of tests were performed previously at the Centre for Materials Engineering at UCT using the same 3-pass finish rolling simulation protocol on the Gleeble 3800 that was used in tthis current study. The results are presented in the MSc thesis by Candice Mias [77].

The starting material for the Mias investigation was transfer bar (i.e material after rough rolling) supplied by industry. The industrial homogenisation protocol for the material prior to rough rolling was identical to the parameters used for Homogenisation 2 (560°C-520°C) in this work. The results generated in the Mias work can therefore be compared to the post finish rolling simulated samples for Homog. 2, where the work from Mias represents source material with the same source material generated by industry, while the results from this work represent a full through process "laboratory scale" simulation of the same process history. The schematic in Figure 4.23 summarises the process history of material and their basis for comparison.

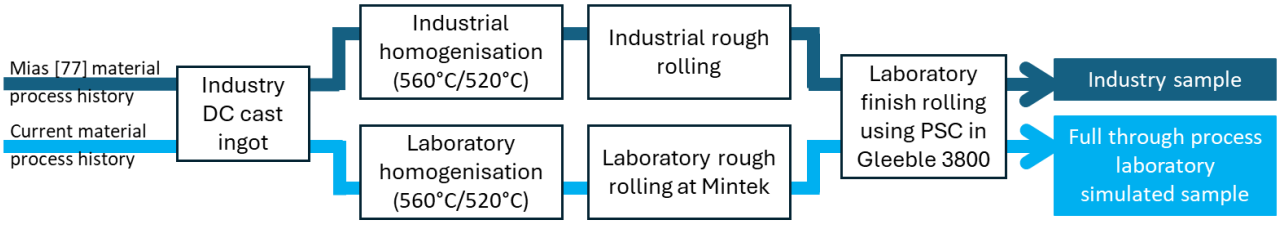

Figure 4.23: Schematic to illustrate "industrially processed" history from the work by Mias [77] and the "laboratory simulated" history in the current investigation.

In order to evaluate whether the results obtained in the current investigation are comparable to results that would be obtained from industrially produced sample material, the results are evaluated against the Mias [77] "industry sample". By comparing the recrystallised grain sizes within the microstructure and cube texture intensity, as well as the flow stress for each of the three passes in the PSC testing in Mias to those presented in the previous Chapters for the current work, we can ascertain whether the results from this current work, where the intention was to simulate the full through process production of the material from homogenisation, through hot rough rolling, to finish rolling on a lab scale, are indeed representative of industrially processed material.

When comparing the grain sizes within the recrystallised microstructures of the work of Mias, with industrial homogenisation and rough rolling, followed by lab scale finish rolling and a subsequent recrystallisation anneal (which represents the "Industry sample") and the Homogenisation 2 sample with lab scale homogenisation, rough rolling and finish rolling and a subsequent recrystallisation

anneal (which represents the “Laboratory simulated sample”,, as shown in Figure 4.24 (a) and (b) respectively, it can be seen that there is a correlation in the grain sizes within the structures. While the indexing and step sizes for the maps are not identical (owing to advancements in the EBSD acquisition system currently in use), the EBSD Grain Size maps have been created with the same colour range for grain size. There are similar numbers of “red”, “orange”, “yellow” and “cyan” grains distributed in the maps in Figure 4.24.

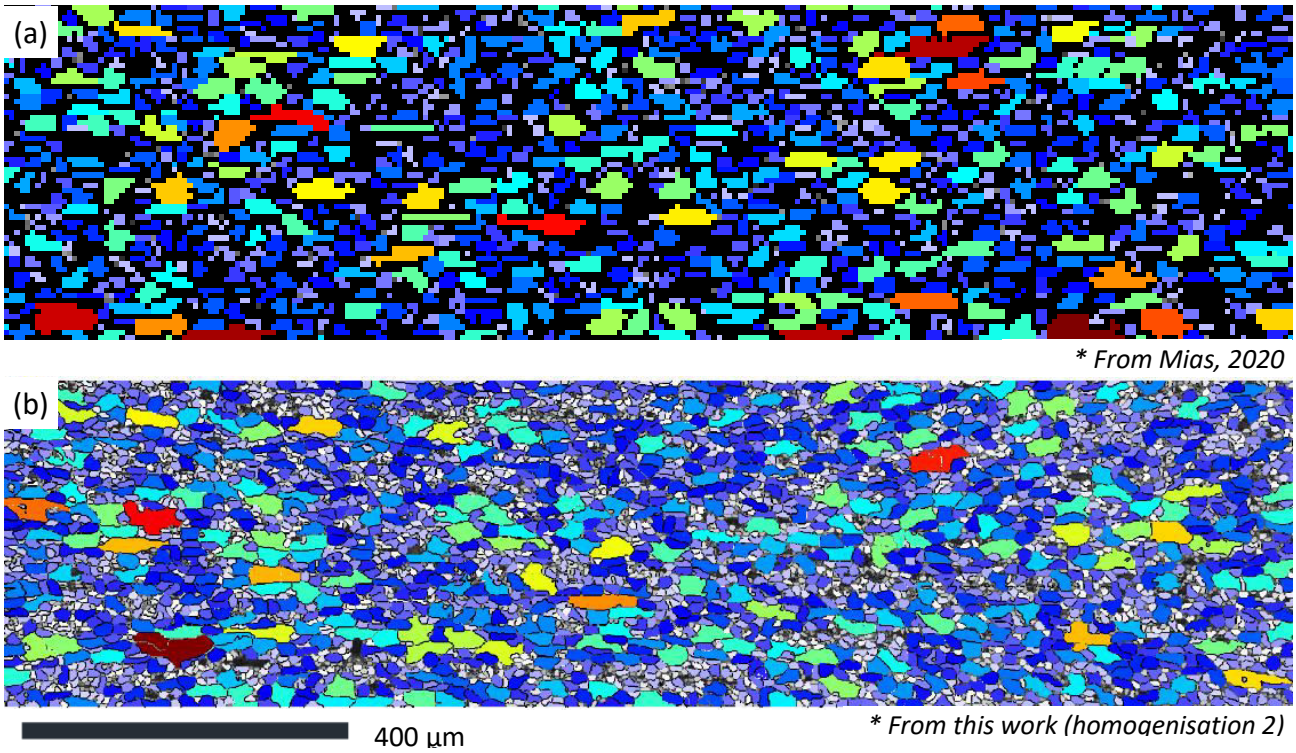

Figure 4.24. (a) EBSD (Euler) map of Mias sample, with industrial homogenisation and rough rolling, followed by lab scale finish rolling and recrystallisation anneal and (b) EBSD (grain size) map of Homogenisation 2 sample with lab scale homogenisation, rough rolling and finish rolling after a recrystallisation anneal. (micron marker for both maps).

The cube texture intensity of the homogenisation 2 (i.e. “Laboratory simulated sample”) samples for this work are reported as 7.49, and the cube texture intensity from Mias is reported at 8.17. While there is a difference between the actual intensity, these results are within an acceptable range for correlation, it must be noted that the EBSD maps from Mias have the cube and grain sizes calculated from maps with relatively low indexing compared to the maps from this work. The correction and smoothing of the data for the grain size EBSD maps would have added some error in fine grain sizes in the Mias samples, the error in the larger grains would be reduced, and therefore are considered comparable. When comparing texture component intensities using ODF maps, the

micro texture intensities are not dependent on step size, but rather on the number of grains indexed, and therefore the intensities are expected to have have little error [78].

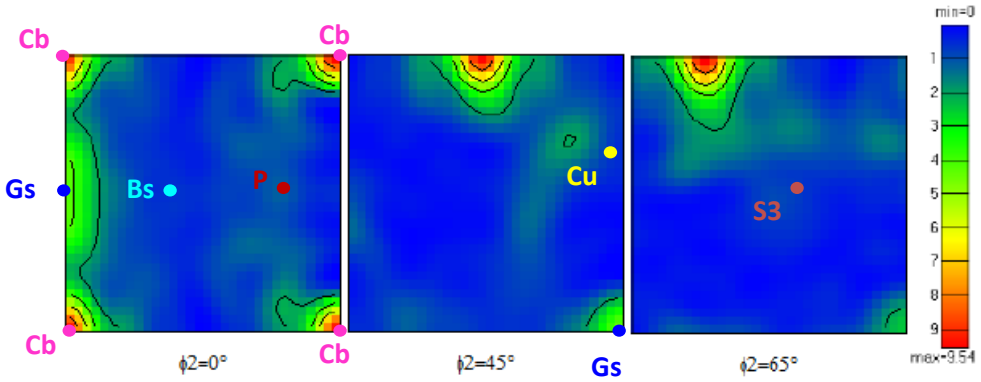

Figure 4.25. ODF sections from Mias sample. Results show a cube texture intensity of 8.17.

While the qualification of the full laboratory scale simulation for this work still requires further testing and evaluation, initial results are promising. The texture intensity and observations of recrystallised grain size between the ”Industry sample” from Mias and the full through process “laboratory simulated sample” from this work are in agreement, where the process histories were were equivalent (as shown in Figure 4.23).

5. Summary discussion

The microstructural analysis of the samples reveals significant differences in dispersoid formation under various homogenisation conditions. The as-cast sample had no dispersoids, which is consistent with the principle that their creation requires high homogenisation temperatures and soaking time at that temperature for Mn diffusion. The sample homogenised at 600°C/520°C exhibited relatively large and coarse dispersoids, some of which had elongated forms. In comparison, the 560°C/520°C sample included finer and more uniformly dispersed dispersoids. The 520°C sample produced the smallest dispersoids with minimum coarsening.

The 520°C homogenisation resulted in the maximum dispersoid density (55.92 particles/μm²), surpassing the 560°C/520°C (19.85 particles/μm²) and 600°C/520°C (8.93 particles/μm²) samples. The 520°C sample had the smallest average dispersoid size (0.056 μm), followed by the 560°C/520°C sample (0.104 μm), and the 600°C/520°C sample showed the biggest dispersoids (0.127 μm). This owes to dispersoids precipitating from supersaturated solid solution, formed during solidification, at elevated and the dispersoids rely on the diffusion of the Mn which is temperature dependent.

The characterisation of IMPs emphasises the importance of homogenisation temperature. The as-cast sample had IMPs that were elongated, irregular, and extensively interconnected formed as a eutectic phase on solidification. The 600°C/520°C sample demonstrated partial spheroidization, coarsening, and fragmentation of large intermetallic phases, resulting in improved dispersion. The 560°C/520°C sample showed refined, isolated particles with low interconnection, but the 520°C sample showed even lower clustering, significant refinement, and limited spheroidization.

Elemental composition investigation of IMPs using EDS mapping showed that as-cast samples included little Si with Mg in solid solution. The 600°C/520°C sample included Si, whereas the 560°C/520°C and 520°C samples showed increasing Si content within the IMPs. While the quantification of the fragmentation through the rough rolling and finish rolling was not investigated in this work, it will form part of the future work planned for this project.

Plane strain compression (PSC) testing indicated different deformation patterns among the samples. The stress-strain graphs demonstrated plastic deformation phases, with the first hit stress ranging from 136 to 148 MPa, the second from 201 to 210 MPa, and the third from 337 to 358 MPa. Homogenization practice 3, with small dispersoids and minor β-to-α phase transformation and morphology changes to the IMPs when compared to the as-cast samples, consistently shows the lowest flow stress. The as-cast sample, with minimal differences in IMP structure and no dispersoids within its structure, has slightly higher values in passes 2 and 3 than Homogenisation 3, but shows similarly low flow stresses, suggesting that the dispersoids themselves provide little to no

strengthening during high-temperature deformation. In contrast, homogenization practices 1 and 2, where IMP structures change more significantly, show higher strain accumulation and strengthening after pass 3. If dispersoids contribute little to strengthening, IMP topology (morphology and distribution) is the primary factor.

For homogenisation temperature influence on recrystallised grain sizes, the 600°C/520°C homogenisation showed the smallest recrystallised grains, which are attributed to coarse dispersoids, that are broadly scattered can accelerate recrystallisation and results in finer recrystallised grain sizes [79], whereas the 560°C/520°C homogenisation showed the largest grains, which are connected with fine, closely spaced dispersoids. While the 520°C homogenisation contained the finest precipitates, the EBSD maps showed a fully recrystallised structure, albeit with smaller grains than the 560°C/520°C samples, which was not expected. This is based on the predictions from the graph in Figure 5.1 where the finer dispersoids will result in larger grains when nucleation limited kinetics are in effect [80]. At a particular volume fraction and dispersoid size ratio, where the dispersoids are very small and closely distributed, there will be no recrystallisation. In the case of the 520°C sample, the dispersoids were still sufficiently large so as not to have generated enough pinning pressure so as to retard recrystallisation However, owing to limited changes in the IMP structures because of the low temperature homogenisation, there may have been an effect on the recrystallisation kinetics associated with a difference in the PSN related recrystallisation processes, thus affecting the overall recrystallisation kinetics.

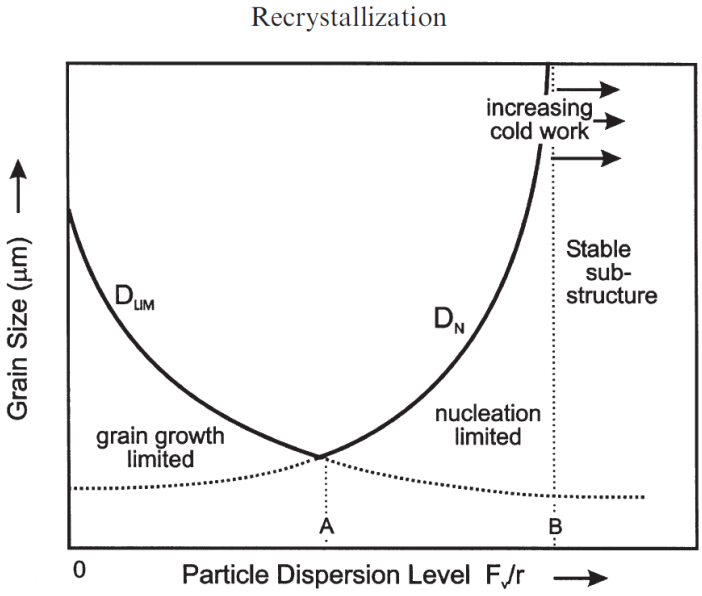

Figure 5.1. The effect of the particle parameters on the recrystallized grain size [80].

The texture evaluation shows an increasing cube texture intensity with a decreasing dispersoid size. There are also random texture components that are attributed to PSN. The as-cast sample, with no dispersoids, exhibited no recrystallisation texture component, but still retained a high proportion of its deformation texture components. This indicates that the dispersoids play an essential role in the final cube texture development during the sheet fabrication process of AA3104 CBS.

6. Conclusions

This study successfully investigated the effect of various homogenisation protocols on the evolution of IMPs and dispersoid structures, along with their subsequent impact on the mechanical performance of the AA3104 aluminium alloy during hot deformation. The experimental approach utilised a fully laboratory scale approach for the simulation of all steps from the homogenisation heat treatments, the hot rough rolling, through to the hot finish rolling. The study's primary findings are highlighted below.

6.1 Effect of Homogenisation on IMPs and Dispersoids.

The size, distribution, and shape of intermetallic particles and dispersoids were all significantly influenced by the homogenisation parameters. Higher homogenisation temperatures (600°C/520°C) resulted in coarser dispersoids and partial spheroidization of IMPs, while lower temperatures (520°C) resulted in finer, well-dispersed dispersoids and a significant reduction in IMP clustering and interconnectedness.

- The 600°C/520°C homogenisation produced coarse dispersoids (127 nm) at a low number density (8.93 particles/μm^2). There was a partial spheroidization of IMPs and little clustering after homogenisation.
- The 520°C homogenisation produced fine, closely spaced dispersoids (56 nm) at a high number density (55.92 particles/μm^2). There was a significant reduction in IMP clustering and interconnectedness after homogenisation.
- The 560°C/520°C homogenisation produced fine, intermediate dispersoid sizes (104 nm) at an improved number density (19.85 particles/μm^2). There was a balance between IMP fragmentation and reduction in interconnectivity between IMPs after homogenisation.

6.2 Microstructural feature development

- The 600°C/520°C homogenisation showed the smallest recrystallised grains, which are attributed to coarse dispersoids that act to accelerate recrystallisation.
- The 560°C/520°C homogenisation showed the largest grains, which are connected with fine, closely spaced dispersoids.

- The 520°C homogenisation contained the finest dispersoids, the EBSD maps showed a fully recrystallised structure where the grains were smaller than the 560°C/520°C homogenisation. This is attributed to a combination of insufficient pinning pressure to fully retard recrystallisation as well as IMP effects on PSN, resulting in a smaller grain size than anticipated.
- There was no recrystallisation in the as-cast protocol, demonstrating that the dispersoids play an essential role in recrystallisation.
- None of the high temperature homogenisation practices resulted in sufficiently fine dispersoids to retard recrystallisation.

6.3 Simulation of industrial process on a laboratory scale

One of the intensions of the work was to simulate the full through process production of the hot rolled AA3104 CBS on a laboratory scale. The procedure started with DC cast ingot materials supplied by industry and all steps, from homogenisation, through hot rough rolling, to finish rolling were performed under strict parameter control on a lab scale.

The IMP and dispersoid structures that were generated with 560°C/520°C protocol, which is in line with the industrial homogenisation protocols, were as anticipated. The IMPs exhibited phase transformations from the β-Al_6(Fe,Mn) phase to the harder α-Al_x(Fe,Mn)$_3Si_2$ phase, and fragmentation and a decrease in the connectivity between particles was evident.

The grain size and texture components that developed in the 560°C/520°C protocol samples were compared to samples where only the finish rolling was simulated (on industrially supplied transfer bar after industrial homogenisation and rough rolling). The grain size and cube texture intensity of the homogenisation 2 sample was in line with sample from Mias [77].

This indicates an equivalent thermomechanical processing route to achieve these similar microstructures. This is a successful first step in the validation of a full through process simulation of processing on a laboratory scale.

7. Recommendations

Below are the recommendations to improve the understanding correlation between homogenisation parameters and evolution of microstructural evolution and mechanical characteristics in AA3104 can-body stock. The recommendations are motivated by the limited scope of research and findings made during this dissertation work through:

- Measuring hardness and tensile strength would create a clear link between mechanical characteristics and microstructural development. This strategy would be consistent with Zhao et al.'s work [13], offering a more thorough connection between material performance, dispersoid properties, and processing conditions.
- Du et al. [47] used thermodynamic modelling to confirm phase stability predictions and compositional trends under different temperature conditions. Such modelling would provide more information on the stability of intermetallic phases and how they change during homogenization and subsequent processing stages.
- Further microstructural research employing Transmission Electron Microscopy (TEM) and three-dimensional imaging techniques, as emphasized by Maire et al. [73], will provide a more in-depth examination of particle connection and dispersoid-matrix interactions. These technologies would provide high-resolution structural information to supplement the findings acquired via SEM-EDS.
- To improve the accuracy of the compositional analysis, cross-check the Energy Dispersive Spectroscopy (EDS) line scan data with additional techniques such as X-ray Diffraction (XRD) for phase identification or TEM for high-resolution compositional profiling. This multi-technique strategy would boost confidence in the phase identification and elemental distribution outcomes.

8. List of References

[1] N Anand Balu, 'Integrated Thermo-Mechanical and Microstructure Evolution Model for Hot Rolling', 2014, doi: 10.13140/RG.2.1.2350.8720.

[2] P. Wycliffe, E. Luce, D. J. Lloyd, J. Fitzsimon, and G. Burger, 'Process for producing aluminum alloy can body stock', US5913989A, Jun. 22, 1999 Accessed: Sep. 22, 2023. [Online]. Available: https://patents.google.com/patent/US5913989A/en

[3] Y. Shi, H. Jin, and P. D. Wu, 'Analysis of cup earing for AA3104-H19 aluminum alloy sheet', *European Journal of Mechanics - A/Solids*, vol. 69, pp. 1–11, May 2018, doi: 10.1016/j.euromechsol.2017.11.013.

[4] R. Králík, B. Křivská, L. Bajtošová, and M. Cieslar, 'Zener drag in twin-roll cast AA8079 alloy', presented at the APPLIED PHYSICS OF CONDENSED MATTER (APCOM 2021), Štrbske Pleso, Slovak Republic, 2021, p. 030004. doi: 10.1063/5.0067389.

[5] I. M. S. Team, 'Ductility of Aluminum | Benefits, Alloying, & Heat Treatment', Industrial Metal Service. Accessed: May 29, 2025. [Online]. Available: https://industrialmetalservice.com/metal-university/advantages-and-disadvantages-of-aluminum-ductility/

[6] L. Corner, 'What Are the Properties of Aluminum?', AZoM. Accessed: May 29, 2025. [Online]. Available: https://www.azom.com/article.aspx?ArticleID=1446

[7] J. G. Kaufman, *Introduction to aluminum alloys and tempers*. Materials Park, OH: ASM International, 2000.

[8] 'What Are the Major Properties of Aluminum? - Kloeckner Metals'. Accessed: Jun. 26, 2023. [Online]. Available: https://www.kloecknermetals.com/blog/what-are-the-major-properties-of-aluminum/

[9] G. E. Totten and D. S. MacKenzie, Eds., *Handbook of aluminum*. New York ; Basel: M. Dekker, 2003.

[10] 'Aluminum 3104-H19'. Accessed: Jun. 26, 2023. [Online]. Available: https://www.matweb.com/search/DataSheet.aspx?MatGUID=aaaabe41a20a4ed2b48270f7f2ef1b2d&ckck=1

[11] K. Dehghani, A. Nekahi, and M. A. M. Mirzaie, 'Using response surface methodology to optimize the strain aging response of AA5052', *Materials Science and Engineering: A*, vol. 527, no. 27–28, pp. 7442–7451, Oct. 2010, doi: 10.1016/j.msea.2010.07.088.

[12] 'What is the difference between intermetallics, precipitates and dispersoids?', ResearchGate. Accessed: Sep. 04, 2023. [Online]. Available: https://www.researchgate.net/post/What-is-the-difference-between-intermetallics-precipitates-and-dispersoids

[13] Q. Zhao, B. Holmedal, and Y. Li, 'Influence of dispersoids on microstructure evolution and work hardening of aluminium alloys during tension and cold rolling', *Philosophical Magazine*, vol. 93, no. 22, pp. 2995–3011, Aug. 2013, doi: 10.1080/14786435.2013.794315.

[14] R. M. Miri, 'Effect of Manganese (Mn) Content and Homogenization Treatment on Hot Deformation of AA3xxx Aluminum Alloys'.

[15] H. D. Merchant, J. Crane, and E. H. Chia, 'Homogenization and annealing of aluminum and copper alloys : proceedings of a symposium sponsored by the Non-Ferrous Metals Committee of the Metallurgical Society and the Annealing and Recovery Committee of MSD/ASM

International, Cincinnati, Ohio, October 12-13, 1987', 1988. [Online]. Available: https://api.semanticscholar.org/CorpusID:107225383
[16] D. T. L. Alexander and A. L. Greer, 'Particle break-up during heat treatment of 3000 series aluminium alloys', *Materials Science and Technology*, vol. 21, no. 8, pp. 955–960, Aug. 2005, doi: 10.1179/174328405X16270.
[17] 'Effect of chemical composition on AA3xxx alloys – Projet de fin d'etudes'. Accessed: Jul. 02, 2023. [Online]. Available: https://www.rapport-gratuit.com/effect-of-chemical-composition-on-aa3xxx-alloys/#respond
[18] Y. J. Li, A. M. F. Muggerud, A. Olsen, and T. Furu, 'Precipitation of partially coherent α-Al(Mn,Fe)Si dispersoids and their strengthening effect in AA 3003 alloy', *Acta Materialia*, vol. 60, no. 3, pp. 1004–1014, Feb. 2012, doi: 10.1016/j.actamat.2011.11.003.
[19] D. T. L. Alexander and A. L. Greer, 'Solid-state intermetallic phase tranformations in 3XXX aluminium alloys', *Acta Materialia*, vol. 50, no. 10, pp. 2571–2583, Jun. 2002, doi: 10.1016/S1359-6454(02)00085-X.
[20] S. L. George and L. Magidi-Chicuba, 'Intermetallic and dispersoid structures in AA3104 aluminium alloy during two-step homogenisation', *Sci Rep*, vol. 14, no. 1, p. 2958, Feb. 2024, doi: 10.1038/s41598-024-51890-2.
[21] L. Lodgaard and N. Ryum, 'Precipitation of dispersoids containing Mn and/or Cr in Al–Mg–Si alloys', *Materials Science and Engineering: A*, vol. 283, no. 1–2, pp. 144–152, May 2000, doi: 10.1016/S0921-5093(00)00734-6.
[22] Y. J. Li and L. Arnberg, 'Quantitative study on the precipitation behavior of dispersoids in DC-cast AA3003 alloy during heating and homogenization', *Acta Materialia*, vol. 51, no. 12, pp. 3415–3428, Jul. 2003, doi: 10.1016/S1359-6454(03)00160-5.
[23] H.-W. Huang and B.-L. Ou, 'Evolution of precipitation during different homogenization treatments in a 3003 aluminum alloy', *Materials & Design*, vol. 30, no. 7, pp. 2685–2692, Aug. 2009, doi: 10.1016/j.matdes.2008.10.012.
[24] J. Rams, 'Wrought Aluminum Alloys', in *Encyclopedia of Materials: Metals and Alloys*, F. G. Caballero, Ed., Oxford: Elsevier, 2022, pp. 132–140. doi: 10.1016/B978-0-12-819726-4.00083-1.
[25] X. Qian, N. Parson, and X.-G. Chen, 'Effects of Mn addition and related Mn-containing dispersoids on the hot deformation behavior of 6082 aluminum alloys', *Materials Science and Engineering: A*, vol. 764, p. 138253, Sep. 2019, doi: 10.1016/j.msea.2019.138253.
[26] C. Gandhi and B. Tech, 'EFFECT OF HOMOGENIZATION ON THE MICROSTRUCTURAL DEVELOPMENT IN A D.C. CAST AA3104 ALUMINUM ALLOY USED FOR CANBODY STOCK'.
[27] J. Hatch, *Aluminum: Properties and physical metallurgy*. 1996.
[28] Z. Li, Z. Zhang, and X.-G. Chen, 'Effect of Metastable Mg2Si and Dislocations on α-Al(MnFe)Si Dispersoid Formation in Al-Mn-Mg 3xxx Alloys', *Metall Mater Trans A*, vol. 49, no. 11, pp. 5799–5814, Nov. 2018, doi: 10.1007/s11661-018-4852-4.
[29] Z. Li, Z. ZHANG, and X.-G. CHEN, 'Effect of magnesium on dispersoid strengthening of Al—Mn—Mg—Si (3xxx) alloys', *Transactions of Nonferrous Metals Society of China*, vol. 26, pp. 2793–2799, Nov. 2016, doi: 10.1016/S1003-6326(16)64407-2.
[30] B. Callegari, T. N. Lima, and R. S. Coelho, 'The Influence of Alloying Elements on the Microstructure and Properties of Al-Si-Based Casting Alloys: A Review', *Metals*, vol. 13, no. 7, p. 1174, Jun. 2023, doi: 10.3390/met13071174.
[31] M. van der Winden, 'Laboratory simulation and modelling of the break-down rolling of AA3104', 1999. [Online]. Available: https://api.semanticscholar.org/CorpusID:114809849

[32] ‘Effect of chemical composition on AA3xxx alloys – Projet de fin d’etudes’. Accessed: Sep. 04, 2023. [Online]. Available: https://www.rapport-gratuit.com/effect-of-chemical-composition-on-aa3xxx-alloys/
[33] E. A. Marquis and D. N. Seidman, ‘Nanoscale structural evolution of Al3Sc precipitates in Al(Sc) alloys’, *Acta Materialia*, vol. 49, no. 11, pp. 1909–1919, Jun. 2001, doi: 10.1016/S1359-6454(01)00116-1.
[34] Y. Yang, P. Z. Zhao, X. Xiao, and X. B. Zheng, ‘Effect of Cu Content on Ageing Behavior for AA3104-H19 Can Body Sheet’, *MSF*, vol. 993, pp. 358–364, May 2020, doi: 10.4028/www.scientific.net/MSF.993.358.
[35] M. Mikolajčík, L. Kuchariková, E. Tillová, J. M. Sanchez, Z. Šurdová, and M. Chalupová, ‘Influence of Copper Addition on the Mechanical Properties and Corrosion Resistance of Self-Hardening Secondary Aluminium Alloy AlZn10Si8Mg’, *Metals*, vol. 14, no. 7, p. 776, Jun. 2024, doi: 10.3390/met14070776.
[36] K. Surani *et al.*, ‘Effect of copper addition on mechanical properties and microstructures of LM25 cast alloys’, *AIP Advances*, vol. 14, no. 4, p. 045025, Apr. 2024, doi: 10.1063/5.0191897.
[37] L. Chen and S. K. Das, ‘(54) METHOD OF FORMING ALUMINUM ALLOY SHEET’, 1992.
[38] G. S. Rohrer, ‘“Introduction to Grains, Phases, and Interfaces—an Interpretation of Microstructure,” Trans. AIME, 1948, vol. 175, pp. 15–51, by C.S. Smith’, *Metall Mater Trans A*, vol. 41, no. 5, pp. 1063–1100, May 2010, doi: 10.1007/s11661-010-0215-5.
[39] A. R. Eivani, S. Valipour, H. Ahmed, J. Zhou, and J. Duszczyk, ‘Effect of the Size Distribution of Nanoscale Dispersed Particles on the Zener Drag Pressure’, *Metall Mater Trans A*, vol. 42, no. 4, pp. 1109–1116, Apr. 2011, doi: 10.1007/s11661-010-0452-7.
[40] F. J. Humphreys and M. Hatherly, *Recrystallization and related annealing phenomena*, 1st ed., Reprinted with corrections. Oxford: Pergamon, 1996.
[41] M. Kenyon, J. Robson, J. Fellowes, and Z. Liang, ‘Effect of Dispersoids on the Microstructure Evolution in Al – Mg – Si Alloys’, *Adv Eng Mater*, vol. 21, no. 4, p. 1800494, Apr. 2019, doi: 10.1002/adem.201800494.
[42] R. Doherty and J. Martin, ‘The effect of a dispersed second phase on the recrystallization of aluminium-copper alloys’, *1962-3*, vol. 91, pp. 332–338.
[43] H. W. Ånes, A. T. J. Van Helvoort, and K. Marthinsen, ‘Orientation dependent pinning of (sub)grains by dispersoids during recovery and recrystallization in an Al–Mn alloy’, *Acta Materialia*, vol. 248, p. 118761, Apr. 2023, doi: 10.1016/j.actamat.2023.118761.
[44] L. Chen and S. K. Das, ‘METHOD OF FORMING ALUMINUM ALLOY SHEET’.
[45] E. Lee and B. Mishra, ‘Effect of Solidification Cooling Rate on Mechanical Properties and Microstructure of Al-Si-Mn-Mg Alloy’, *Mater. Trans.*, vol. 58, no. 11, pp. 1624–1627, 2017, doi: 10.2320/matertrans.M2017170.
[46] Y. Li and L. Arnberg, ‘Precipitation of Dispersoids in DC-Cast AA3103 Alloy during Heat Treatment’, in *Essential Readings in Light Metals*, J. F. Grandfield and D. G. Eskin, Eds., Cham: Springer International Publishing, 2016, pp. 1021–1027. doi: 10.1007/978-3-319-48228-6_129.
[47] Q. Du, W. J. Poole, M. A. Wells, and N. C. Parson, ‘Microstructure evolution during homogenization of Al–Mn–Fe–Si alloys: Modeling and experimental results’, *Acta Materialia*, vol. 61, no. 13, pp. 4961–4973, Aug. 2013, doi: 10.1016/j.actamat.2013.04.050.
[48] R. W. Hertzberg, R. P. Vinci, J. L. Hertzberg, and R. P. Vinci, *Deformation and fracture mechanics of engineering materials*, 5. ed. Hoboken, NJ: Wiley, 2013.
[49] W. D. Callister, *Materials Science and Engineering*. New York: Wiley, 2019.

[50] K. V. Werner *et al.*, 'Reconciling experimental and theoretical stacking fault energies in face-centered cubic materials with the experimental twinning stress', *Materialia*, vol. 27, p. 101708, Mar. 2023, doi: 10.1016/j.mtla.2023.101708.
[51] C. K. Hyde, 'Critical analysis of simulated thermomechanical processing of aluminium can body stock', 2015, [Online]. Available: http://hdl.handle.net/11427/15749
[52] E. Tochigi, A. Nakamura, N. Shibata, and Y. Ikuhara, 'Dislocation Structures in Low-Angle Grain Boundaries of α-Al2O3', *Crystals*, vol. 8, no. 3, p. 133, Mar. 2018, doi: 10.3390/cryst8030133.
[53] D. Raabe, 'Recovery and Recrystallization: Phenomena, Physics, Models, Simulation', in *Physical Metallurgy*, Elsevier, 2014, pp. 2291–2397. doi: 10.1016/B978-0-444-53770-6.00023-X.
[54] S. P. Bellier and R. D. Doherty, 'The structure of deformed aluminium and its recrystallization—investigations with transmission Kossel diffraction', *Acta Metallurgica*, vol. 25, no. 5, pp. 521–538, May 1977, doi: 10.1016/0001-6160(77)90192-4.
[55] R. D. Doherty *et al.*, 'Current issues in recrystallization: a review', *Materials Science and Engineering: A*, vol. 238, no. 2, pp. 219–274, Nov. 1997, doi: 10.1016/S0921-5093(97)00424-3.
[56] S. Suwas and N. P. Gurao, 'Crystallographic texture in Materials', vol. 88, 2008.
[57] J. Hirsch, P. Wagner, and H. Schmiedel, 'Earing and Texture Evolution in Al Can-Sheet', *MSF*, vol. 217–222, pp. 641–646, May 1996, doi: 10.4028/www.scientific.net/MSF.217-222.641.
[58] M. Benke *et al.*, 'A simple correlation between texture and earing', *IOP Conf. Ser.: Mater. Sci. Eng.*, vol. 426, p. 012003, Oct. 2018, doi: 10.1088/1757-899X/426/1/012003.
[59] R. L. Higginson, M. Aindow, and P. S. Bate, 'The effect of finely dispersed particles on primary recrystallisation textures in AlMnSi alloys', *Materials Science and Engineering: A*, vol. 225, no. 1–2, pp. 9–21, Apr. 1997, doi: 10.1016/S0921-5093(96)10571-2.
[60] E28 Committee, *Test Method for Plastic Strain Ratio r for Sheet Metal*. doi: 10.1520/E0517-00R10.
[61] G. D. Thomas, 'A yield function to simulate earing in the deep drawing of aluminium', 1996, [Online]. Available: http://hdl.handle.net/11427/9494
[62] O. Engler, 'Control of texture and earing in aluminium alloy AA 3105 sheet for packaging applications', *Materials Science and Engineering: A*, vol. 538, pp. 69–80, Mar. 2012, doi: 10.1016/j.msea.2012.01.015.
[63] J. H. Driver and O. Engler, 'Design of Aluminum Rolling Processes for Foil, Sheet, and Plate', in *Encyclopedia of Aluminum and Its Alloys*, 1st ed., Boca Raton: CRC Press, 2019. doi: 10.1201/9781351045636-140000401.
[64] H.-W. Huang, B.-L. Ou, and C.-T. Tsai, 'Effect of Homogenization on Recrystallization and Precipitation Behavior of 3003 Aluminum Alloy', *Mater. Trans.*, vol. 49, no. 2, pp. 250–259, 2008, doi: 10.2320/matertrans.MRA2007615.
[65] R. G. Kamat, 'AA3104 can-body stock ingot: Characterization and homogenization', *JOM*, vol. 48, no. 6, pp. 34–38, Jun. 1996, doi: 10.1007/BF03222964.
[66] J. Hirsch and T. Al-Samman, 'Superior light metals by texture engineering: Optimized aluminum and magnesium alloys for automotive applications', *Acta Materialia*, vol. 61, no. 3, pp. 818–843, Feb. 2013, doi: 10.1016/j.actamat.2012.10.044.
[67] M. S. Loveday *et al.*, 'Measurement of flow stress in hot plane strain compression tests', *Materials at High Temperatures*, vol. 23, no. 2, pp. 85–118, Jan. 2006, doi: 10.1179/mht.2006.006.

[68] E. Orowan, ‘The Calculation of Roll Pressure in Hot and Cold Flat Rolling’, *Proceedings of the Institution of Mechanical Engineers*, vol. 150, no. 1, pp. 140–167, Jun. 1943, doi: 10.1243/PIME_PROC_1943_150_025_02.
[69] ‘Handbook Of Workability And Process Design [PDF|TXT]’. Accessed: Oct. 18, 2023. [Online]. Available: https://pdfcookie.com/documents/handbook-of-workability-and-process-design-0nvoxmkn49v8
[70] K. Drozd, J. Horsinka, J. Kliber, M. Černý, and D. Ostroushko, ‘STUDY OF DEVELOPMENT OF STRAIN IN PLANE STRAIN COMPRESSION TEST’, 2011.
[71] A. J. Lacey, M. S. Loveday, G. J. Mahon, B. Roebuck, and C. M. Sellars, ‘Measuring Flow Stress in Hot Plane Strain Compression Tests’.
[72] L. A. Dobrzański, W. Borek, M. Czaja, and J. Mazurkiewicz, ‘Structure of X11MnSiAl17-1-3 steel after hot-rolling and Gleeble simulations’, *Archives of Materials Science and Engineering*, vol. 61, no. 1, 2013.
[73] E. Maire, J. Grenier, D. Daniel, A. Baldacci, H. Klocker, and A. Bigot, ‘Quantitative 3D characterization of intermetallic phases in an Al–Mg industrial alloy by X-ray microtomography’, *Scripta Materialia*, vol. 55, no. 2, pp. 123–126, Jul. 2006, doi: 10.1016/j.scriptamat.2006.03.066.
[74] dan-slater, *dan-slater/paramaterial*. (Jul. 04, 2024). Python. Accessed: Feb. 04, 2025. [Online]. Available: https://github.com/dan-slater/paramaterial
[75] J. Hirsch, ‘TEXTURE EVOLUTION DURING ROLLING OF ALUMINIUM ALLOYS’.
[76] P. Ratchev, B. Verlinden, and P. Van Houtte, ‘Effect of preheat temperature on the orientation relationship of (Mn,Fe)Al6 precipitates in an AA 5182 Aluminium—Magnesium alloy’, *Acta Metallurgica et Materialia*, vol. 43, no. 2, pp. 621–629, Feb. 1995, doi: 10.1016/0956-7151(94)00261-F.
[77] C. Mias, ‘Effect of processing parameters on microstructure and cube texture evolution during hot rolling of AA3104’, MSc Thesis, University of Cape Town, Cape Town, South Africa, 2020.
[78] F. J. Humphreys and M. Hatherly, *Recrystallization and Related Annealing Phenomena*. Jordan Hill: Elsevier Science, 2012.
[79] P. R. Rios, F. Siciliano Jr, H. R. Z. Sandim, R. L. Plaut, and A. F. Padilha, ‘Nucleation and growth during recrystallization’, *Mat. Res.*, vol. 8, no. 3, pp. 225–238, Sep. 2005, doi: 10.1590/S1516-14392005000300002.
[80] F. J. Humphreys and M. Hatherly, ‘GRAIN GROWTH FOLLOWING RECRYSTALLIZATION’, in *Recrystallization and Related Annealing Phenomena*, Elsevier, 1995, pp. 281–325. doi: 10.1016/B978-0-08-041884-1.50016-7.

Appendix A.

8.1 SEM-EDS of intermetallic particles (As-cast)

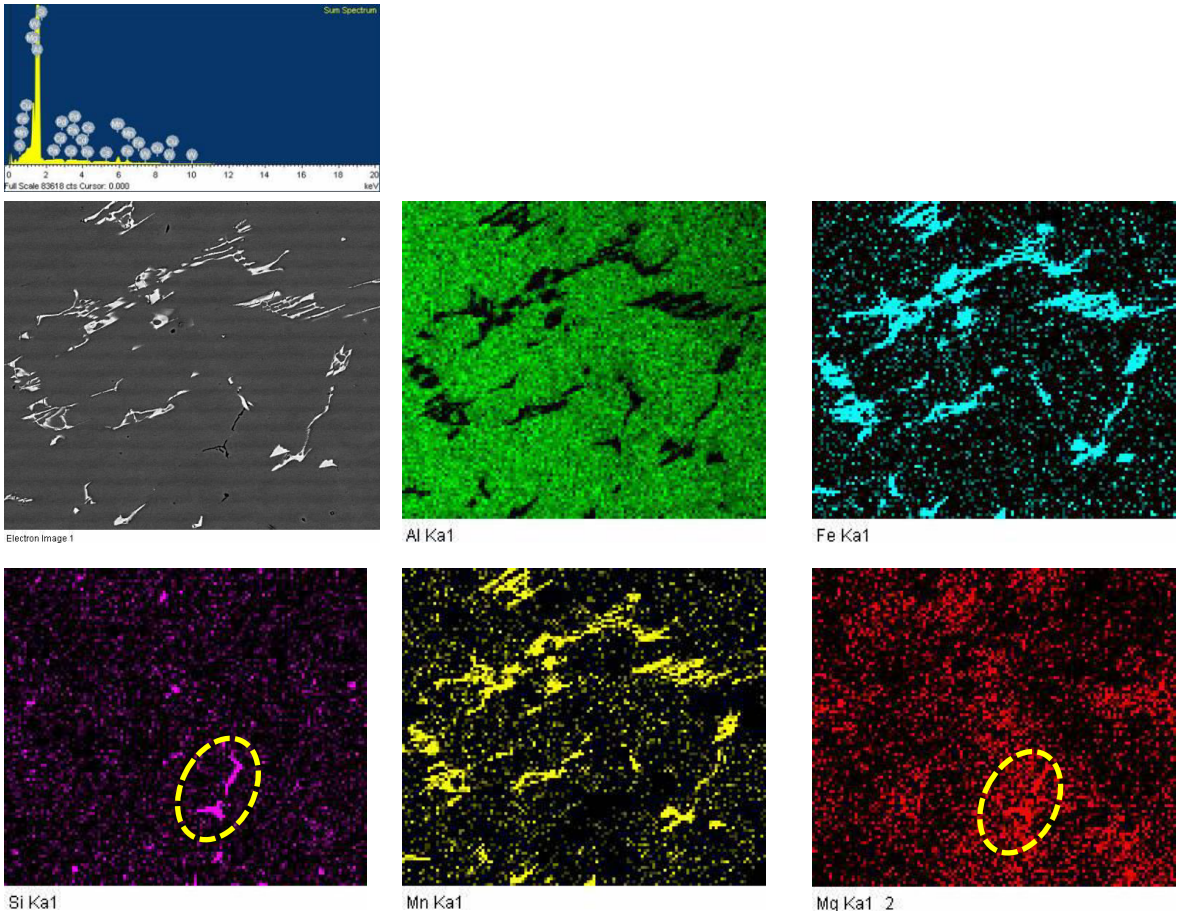

The yellow highlighted shown the Mg_2Si intermetallic compound within the as-cast samples.

8.2 SEM-EDS of intermetallic particles (Homogenisation 1)

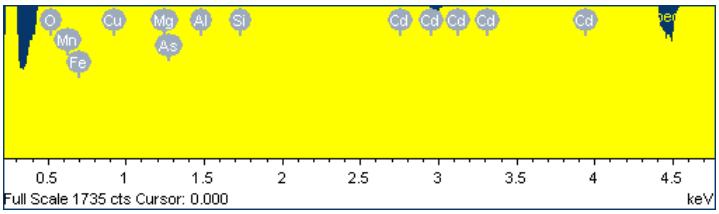

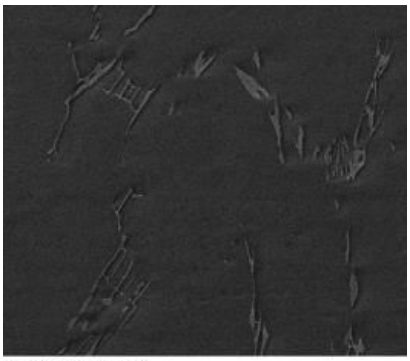

Electron Image 1

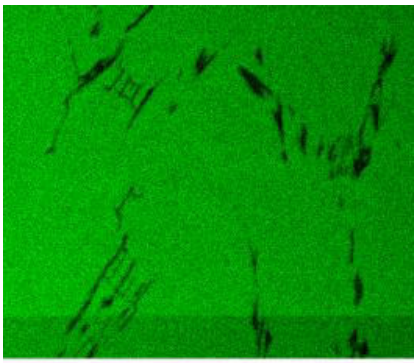

Al Ka1

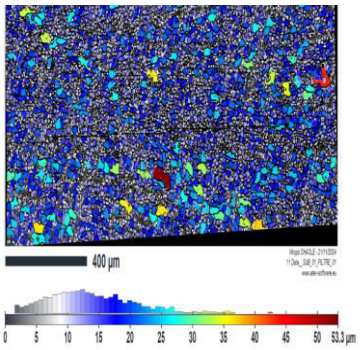

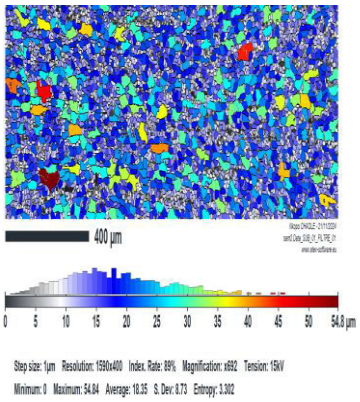

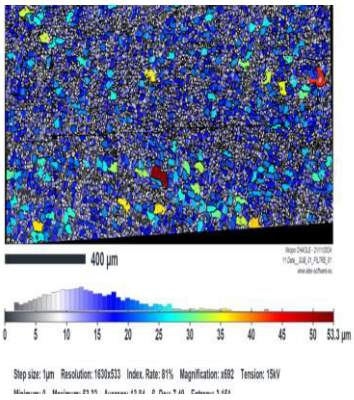

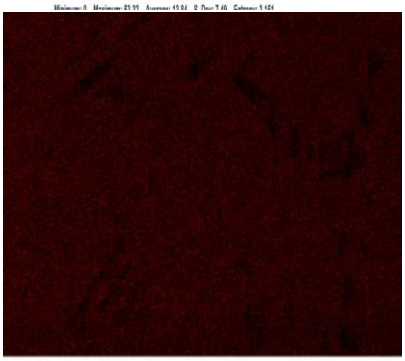

Mg Ka1_2

8.3 SEM-EDS of intermetallic particles (Homogenisation 2)

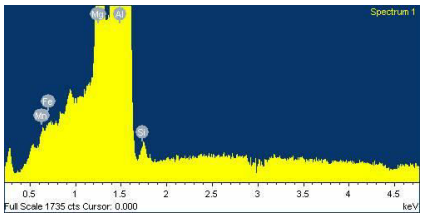

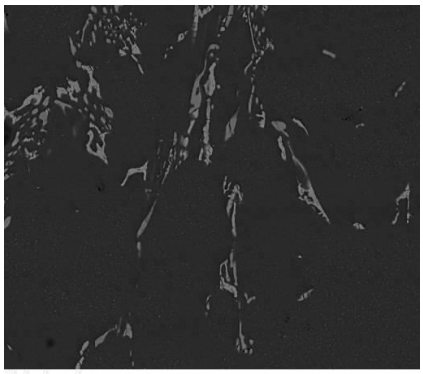
Electron Image 1

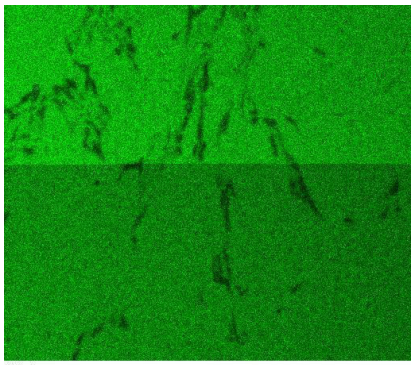
Al Ka1

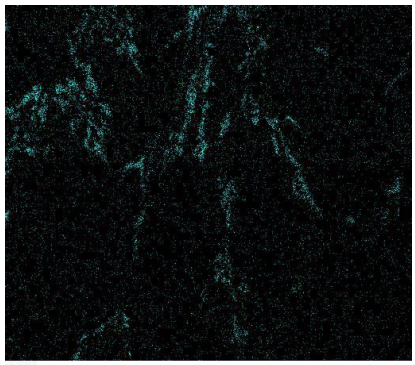
Fe Ka1

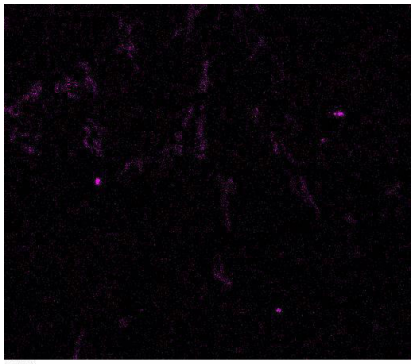
Si Ka1

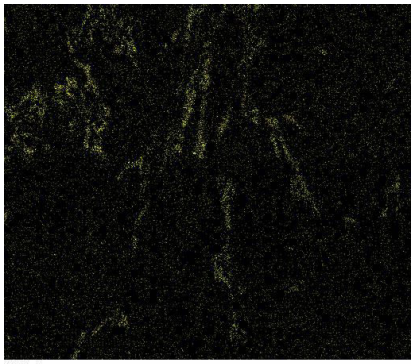
Mn Ka1

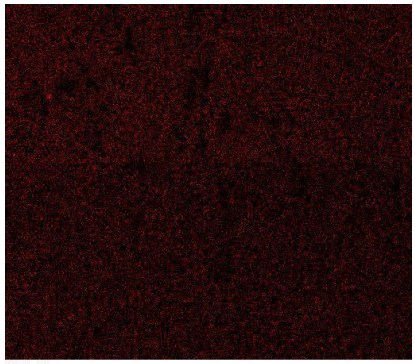
Mg Ka1_2

8.4 SEM-EDS of intermetallic particles (Homogenisation 3)

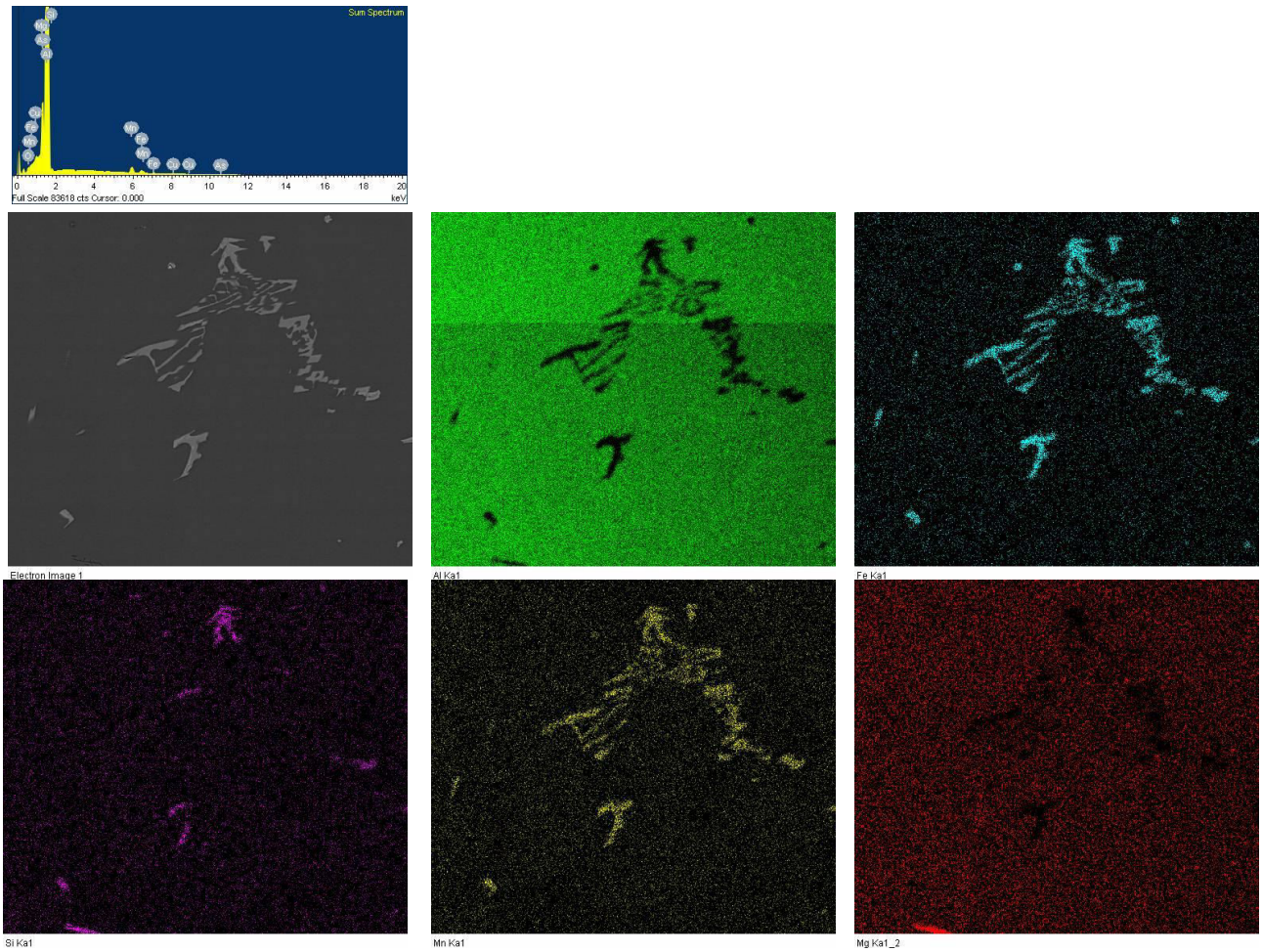

Appendix B.

8.5 As-cast samples PSC temperature profiles

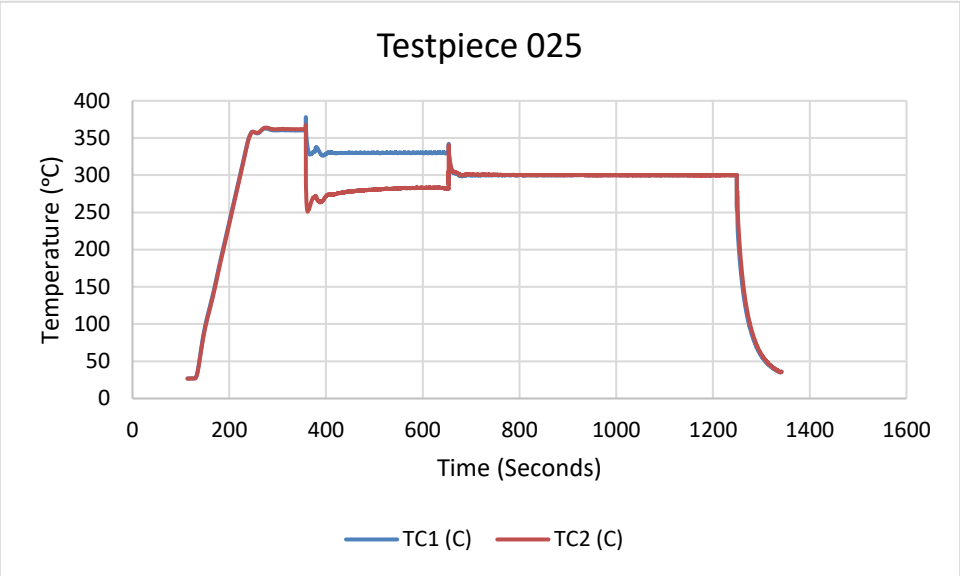

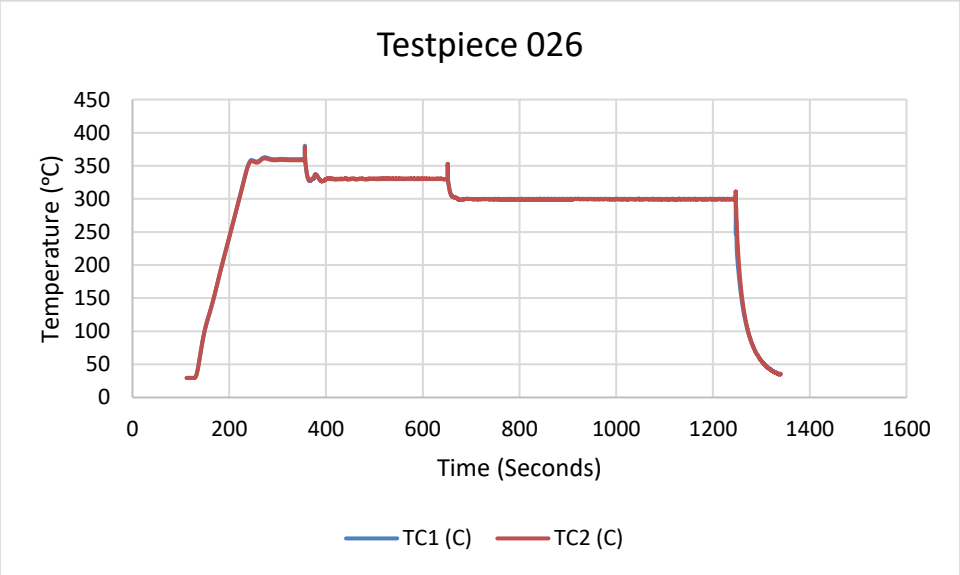

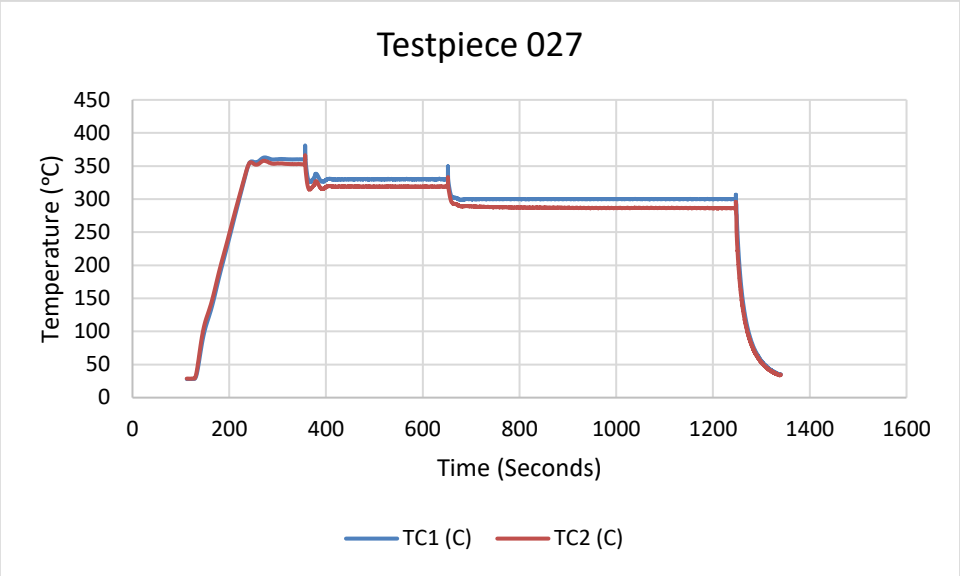

8.6 Homogenisation 1 samples PSC temperature profiles

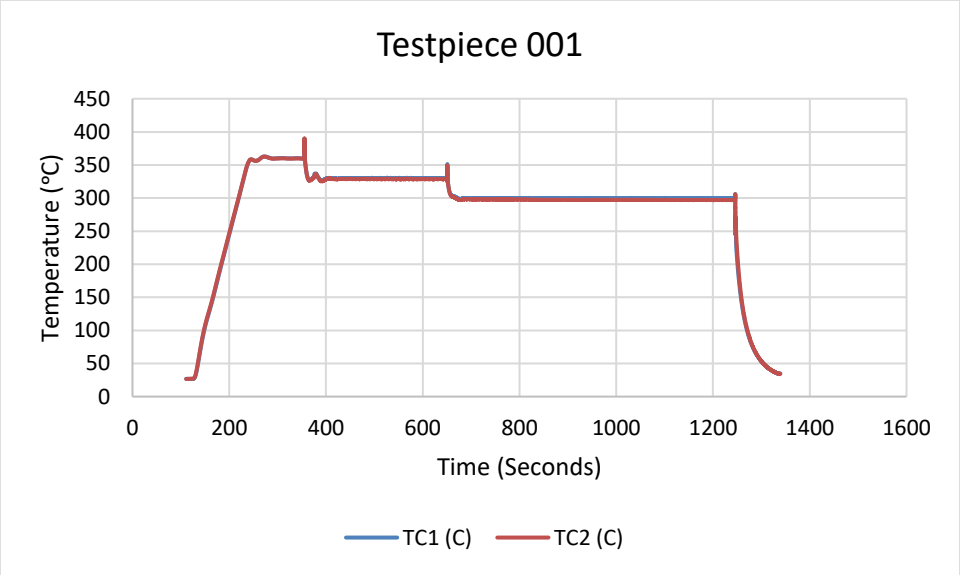

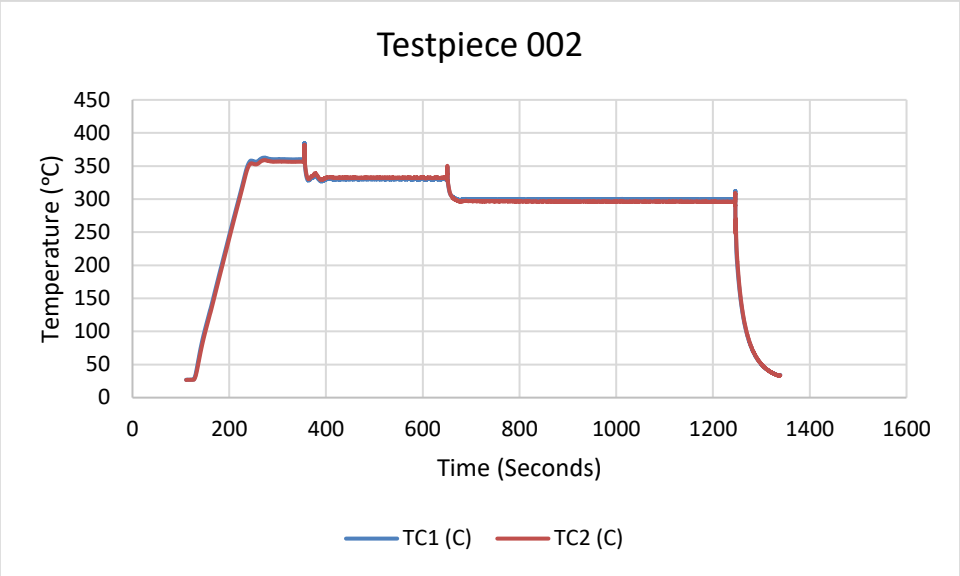
Testpiece 002
Temperature (°C)
450
400
350
300
250
200
150
100
50
0
0
200
400
600
800
1000
1200
1400
1600
Time (Seconds)
TC1 (C)
TC2 (C)

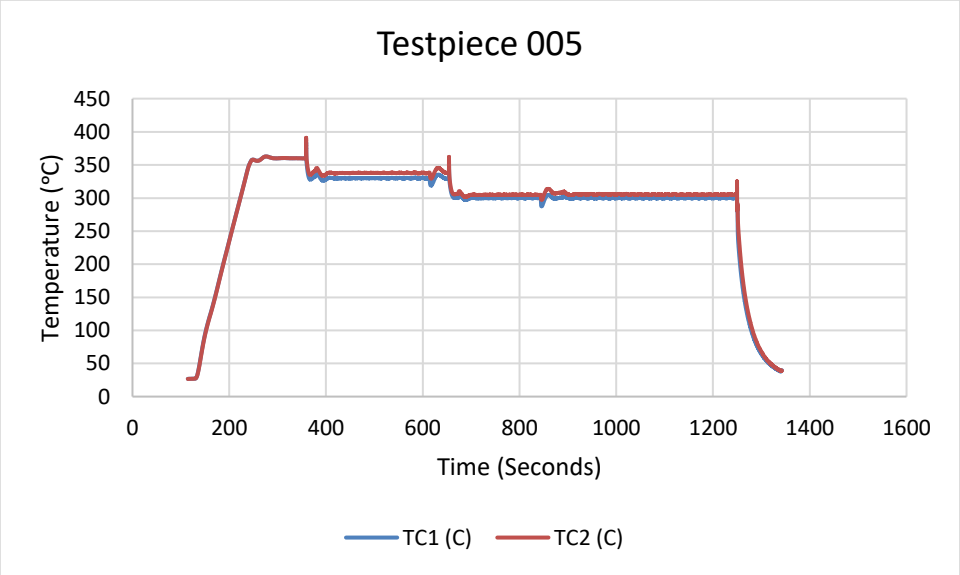
Testpiece 005
Temperature (°C)
450
400
350
300
250
200
150
100
50
0
0
200
400
600
800
1000
1200
1400
1600
Time (Seconds)
TC1 (C)
TC2 (C)

8.7 Homogenisation 2 samples PSC temperature profiles

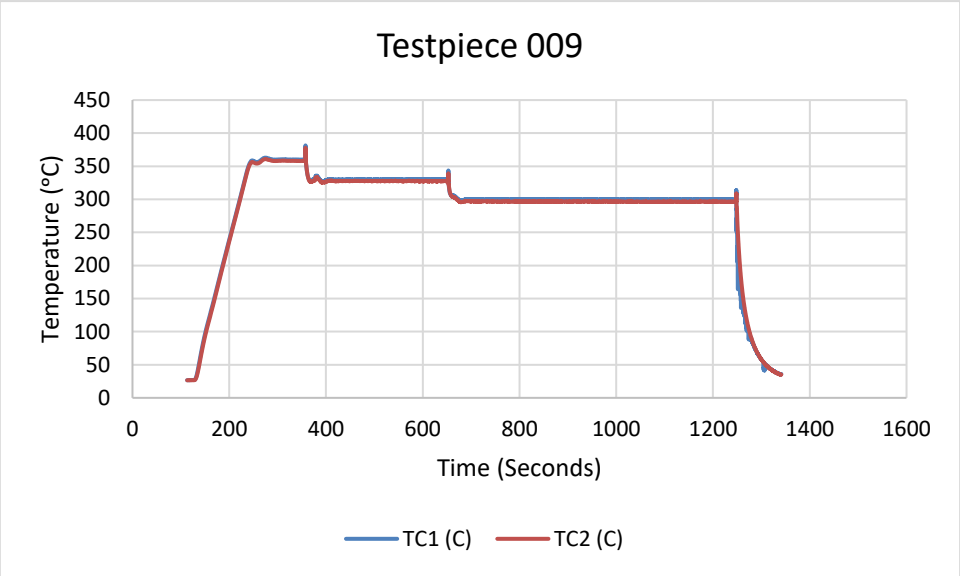

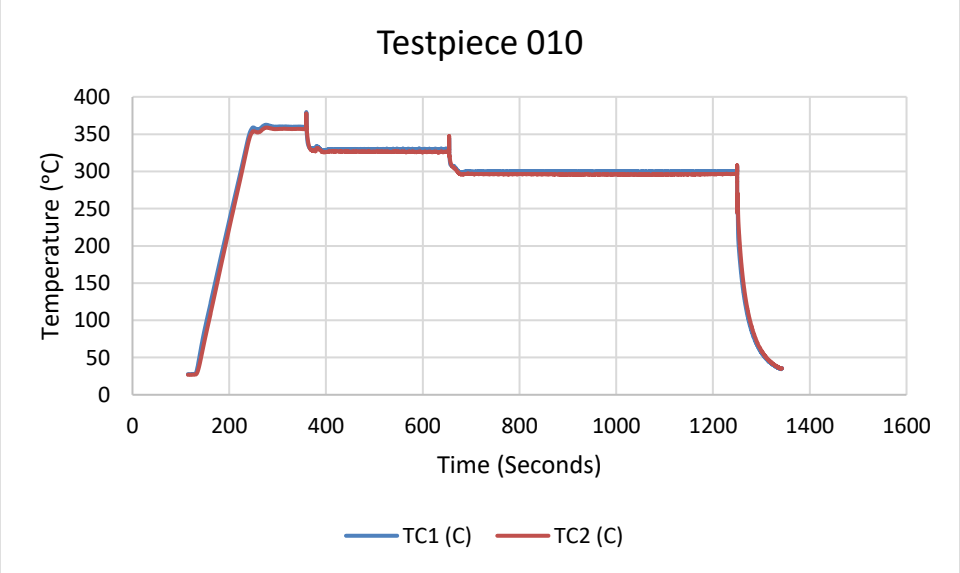

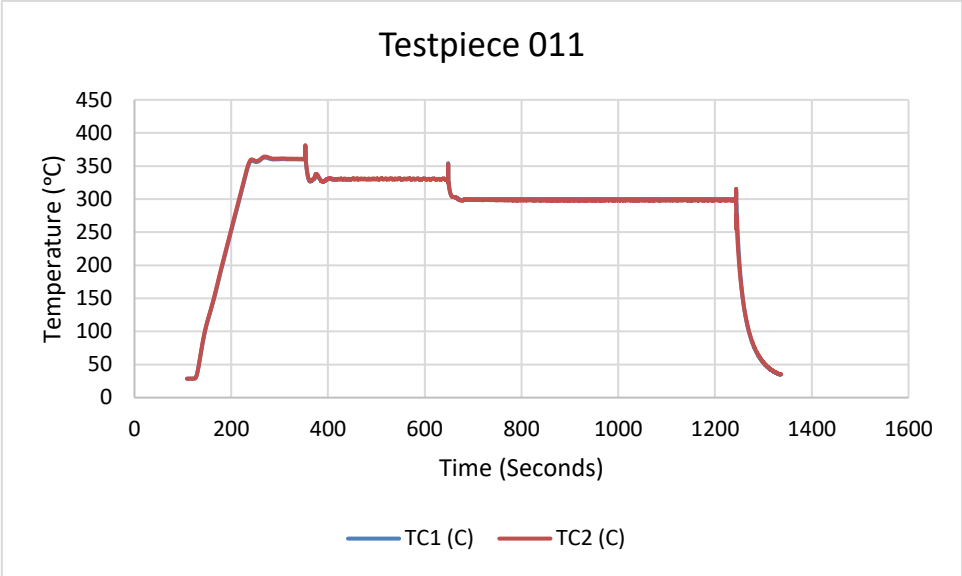

8.8 Homogenisation 2 samples PSC temperature profiles

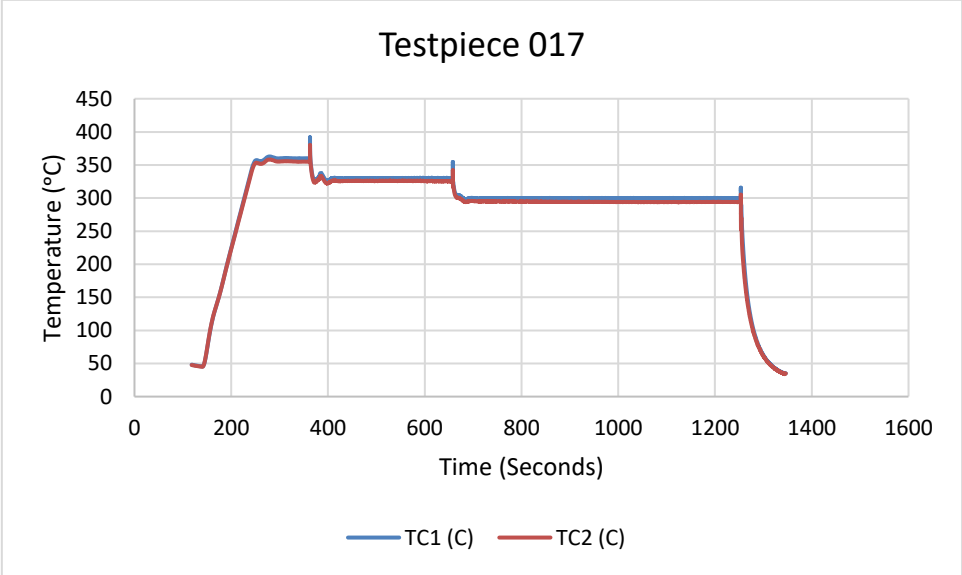

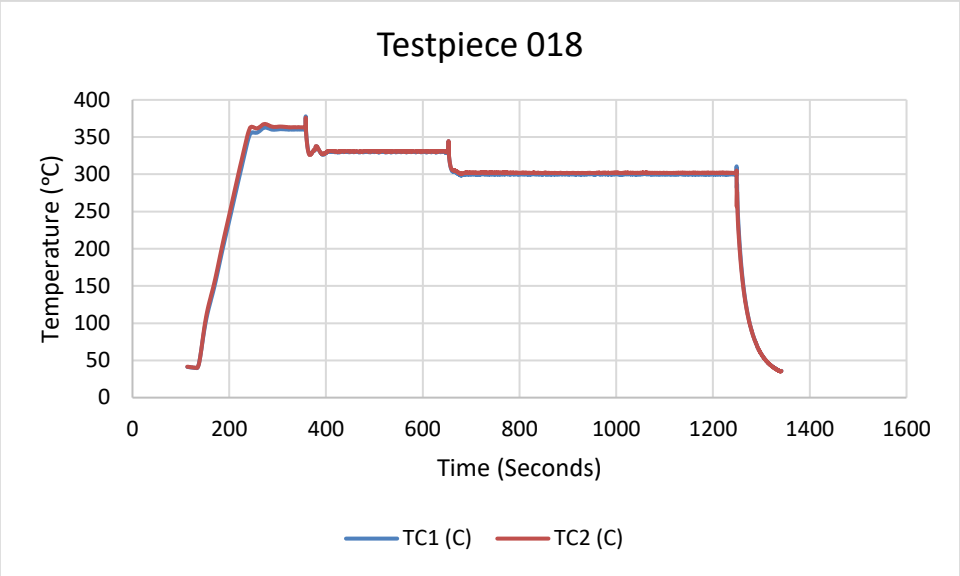
Testpiece 018
Temperature (°C)
400
350
300
250
200
150
100
50
0
0
200
400
600
800
1000
1200
1400
1600
Time (Seconds)
TC1 (C)
TC2 (C)

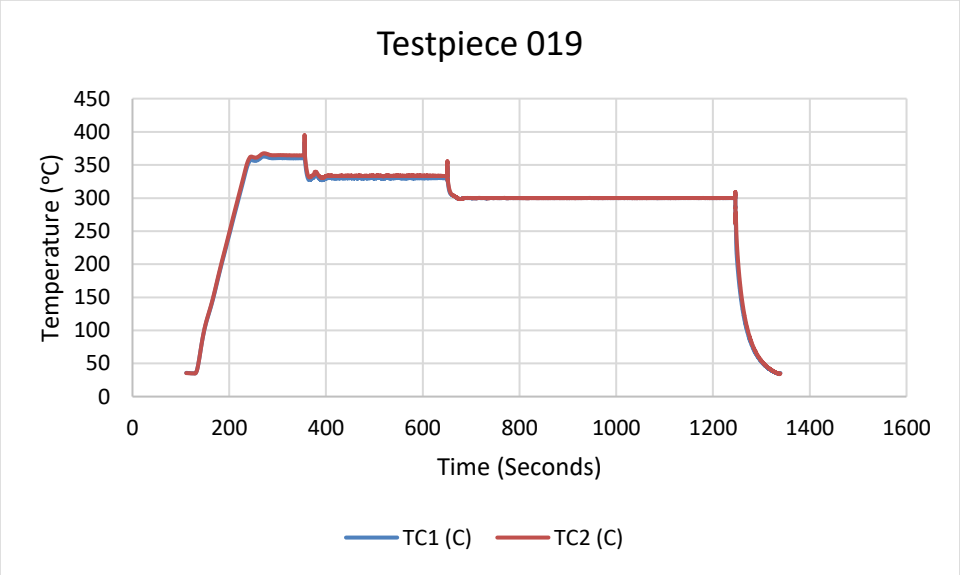
Testpiece 019
Temperature (°C)
450
400
350
300
250
200
150
100
50
0
0
200
400
600
800
1000
1200
1400
1600
Time (Seconds)
TC1 (C)
TC2 (C)

Appendix C.

Colour key
Likely consistent across all testpiece reports
Consistent across test type
Inputed before testing
Inputed after testing
Automatically calculated

8.9 As-cast testpieces geometry

Testpiece Geometry 025				
Dimension	Breadth (mm)		Heigth (mm)	
Initial	b1	20	h1 (centre)	11.085
	b2	20	h2 (edge)	11.084
	b3	20	h3 (edge)	11.083
	-	Note: Cant measure precicely due to paint	h4 (edge)	11.088
	-	-	h5 (edge)	11.087
Average Initial	b_o	20	$h_{o\text{-measured}}$	11.085
Std Dev Initial	S_{b0}	0	S_{h0}	0.001854724
True initial (after Tx compression)	-	-	h_0	**11.085**
Dimensional coeficients	-	-	C_{h0} (No standard for C_{h0})	1.673E-04
Final	B_f		h6 (centre)	2.066
	-	-	h7 (edge)	2.091
	-	-	h8 (edge)	2.073
	-	-	h9 (edge)	2.054
	-	-	h10 (edge)	2.057
Average Final	-	-	h_f	2.068
Std Dev Final	-	-	S_{hf}	0.014788509
Dimensional coeficients	-	-	C_{hf} =(C_{hf} < 0.04)	0.007

Testpiece Geometry 026		
Dimension	Breadth (mm)	Heigth (mm)

Initial	b1	20	h1 (centre)	11.075
	b2	20	h2 (edge)	11.076
	b3	20	h3 (edge)	11.07
	-	Note: Cant measure precicely due to paint	h4 (edge)	11.076
	-	-	h5 (edge)	11.076
Average Initial	b_o	20	$h_{o\text{-measured}}$	11.075
Std Dev Initial	S_{b0}	0	S_{h0}	0.002332381
True initial (after Tx compression)	-	-	h_0	**11.075**
Dimensional coeficients	-	-	C_{h0} (No standard for C_{h0})	2.106E-04
Final	B_f		h6 (centre)	2.076
	-	-	h7 (edge)	2.082
	-	-	h8 (edge)	2.076
	-	-	h9 (edge)	2.054
	-	-	h10 (edge)	2.057
Average Final	-	-	h_f	2.069
Std Dev Final	-	-	S_{hf}	0.01260952
Dimensional coeficients	-	-	C_{hf} =(C_{hf} < 0.04)	0.006

Testpiece Geometry 027				
Dimension	Breadth (mm)		Heigth (mm)	
Initial	b1	20	h1 (centre)	11.075
	b2	20	h2 (edge)	11.079
	b3	20	h3 (edge)	11.075
	-	Note: Cant measure precicely due to paint	h4 (edge)	11.076
	-	-	h5 (edge)	11.078
Average Initial	b_o	20	$h_{o\text{-measured}}$	11.077
Std Dev Initial	S_{b0}	0	S_{h0}	0.001624808
True initial (after Tx compression)	-	-	h_0	**11.077**
Dimensional coeficients	-	-	C_{h0} (No standard for C_{h0})	1.467E-04
Final	B_f		h6 (centre)	2.07
	-	-	h7 (edge)	2.076
	-	-	h8 (edge)	2.076
	-	-	h9 (edge)	2.068
	-	-	h10 (edge)	2.061

Average Final	-	-	h_f	2.070
Std Dev Final	-	-	S_{hf}	0.00626099
Dimensional coeficients	-	-	C_{hf} =(C_{hf} < 0.04)	0.003

8.10 Homogenisation 1 testpieces geometry

Testpiece Geometry 001				
Dimension	Breadth (mm)		Heigth (mm)	
Initial	b1	20	h1 (centre)	11.081
	b2	20	h2 (edge)	11.079
	b3	20	h3 (edge)	11.078
	-	Note: Cant measure precicely due to paint	h4 (edge)	11.076
	-	-	h5 (edge)	11.079
Average Initial	b_o	20	$h_{o\text{-measured}}$	11.079
Std Dev Initial	S_{b0}	0	S_{h0}	0.00162480 8
True initial (after Tx compression)	-	-	h_0	**11.079**
Dimensional coeficients	-	-	C_{h0} (No standard for C_{h0})	1.467E-04
Final	B_f		h6 (centre)	2.069
	-	-	h7 (edge)	2.074
	-	-	h8 (edge)	2.074
	-	-	h9 (edge)	2.068
	-	-	h10 (edge)	2.068
Average Final	-	-	h_f	2.071
Std Dev Final	-	-	S_{hf}	0.00313049 5
Dimensional coeficients	-	-	C_{hf} =(C_{hf} < 0.04)	0.002

Testpiece Geometry 002				
Dimension	Breadth (mm)		Heigth (mm)	
Initial	b1	20	h1 (centre)	11.086
	b2	20	h2 (edge)	11.078
	b3	20	h3 (edge)	11.079
	-	Note: Cant measure precicely due to paint	h4 (edge)	11.078

	-	-	h5 (edge)	11.079
Average Initial	b_o	20	$h_{o\text{-measured}}$	11.080
Std Dev Initial	S_{b0}	0	S_{h0}	0.00303315
True initial (after Tx compression)	-	-	h_0	**11.080**
Dimensional coeficients	-	-	C_{h0} (No standard for C_{h0})	2.738E-04
Final	B_f		h6 (centre)	2.071
	-	-	h7 (edge)	2.072
	-	-	h8 (edge)	2.073
	-	-	h9 (edge)	2.071
	-	-	h10 (edge)	2.071
Average Final	-	-	h_f	2.072
Std Dev Final	-	-	S_{hf}	0.000894427
Dimensional coeficients	-	-	C_{hf} =(C_{hf} < 0.04)	0.000

Testpiece Geometry 005				
Dimension	Breadth (mm)		Heigth (mm)	
Initial	b1	20	h1 (centre)	11.078
	b2	20	h2 (edge)	11.078
	b3	20	h3 (edge)	11.079
	-	Note: Cant measure precicely due to paint	h4 (edge)	11.078
	-	-	h5 (edge)	11.079
Average Initial	b_o	20	$h_{o\text{-measured}}$	11.078
Std Dev Initial	S_{b0}	0	S_{h0}	0.000489898
True initial (after Tx compression)	-	-	h_0	**11.078**
Dimensional coeficients	-	-	C_{h0} (No standard for C_{h0})	4.422E-05
Final	B_f		h6 (centre)	2.072
	-	-	h7 (edge)	2.075
	-	-	h8 (edge)	2.074
	-	-	h9 (edge)	2.076
	-	-	h10 (edge)	2.075
Average Final	-	-	h_f	2.074
Std Dev Final	-	-	S_{hf}	0.001516575
Dimensional coeficients	-	-	C_{hf} =(C_{hf} < 0.04)	0.001

8.11 Homogenisation 2 testpieces geometry

Testpiece Geometry 009				
Dimension	Breadth (mm)		Heigth (mm)	
Initial	b1	20	h1 (centre)	11.082
	b2	20	h2 (edge)	11.079
	b3	20	h3 (edge)	11.079
	-	Note: Cant measure precicely due to paint	h4 (edge)	11.08
	-	-	h5 (edge)	11.081
Average Initial	b_o	20	$h_{o\text{-measured}}$	11.080
Std Dev Initial	S_{b0}	0	S_{h0}	0.00116619
True initial (after Tx compression)	-	-	h_0	**11.080**
Dimensional coeficients	-	-	C_{h0} (No standard for C_{h0})	1.052E-04
Final	B_f		h6 (centre)	2.068
	-	-	h7 (edge)	2.071
	-	-	h8 (edge)	2.068
	-	-	h9 (edge)	2.072
	-	-	h10 (edge)	2.074
Average Final	-	-	h_f	2.071
Std Dev Final	-	-	S_{hf}	0.00260768 1
Dimensional coeficients	-	-	C_{hf} =(C_{hf} < 0.04)	0.001

Testpiece Geometry 010				
Dimension	Breadth (mm)		Heigth (mm)	
Initial	b1	20	h1 (centre)	11.072
	b2	20	h2 (edge)	11.075
	b3	20	h3 (edge)	11.074
	-	Note: Cant measure precicely due to paint	h4 (edge)	11.073
	-	-	h5 (edge)	11.072
Average Initial	b_o	20	$h_{o\text{-measured}}$	11.073
Std Dev Initial	S_{b0}	0	S_{h0}	0.00116619

True initial (after Tx compression)	-	-	h_0	**11.073**
Dimensional coeficients	-	-	C_{h0} (No standard for C_{h0})	1.053E-04
Final	B_f		h6 (centre)	2.076
	-	-	h7 (edge)	2.071
	-	-	h8 (edge)	2.075
	-	-	h9 (edge)	2.073
	-	-	h10 (edge)	2.075
Average Final	-	-	h_f	2.074
Std Dev Final	-	-	S_{hf}	0.002
Dimensional coeficients	-	-	C_{hf} =(C_{hf} < 0.04)	0.001

Testpiece Geometry 011				
Dimension	Breadth (mm)		Heigth (mm)	
Initial	b1	20	h1 (centre)	11.076
	b2	20	h2 (edge)	11.073
	b3	20	h3 (edge)	11.072
	-	Note: Cant measure precicely due to paint	h4 (edge)	11.073
	-	-	h5 (edge)	11.074
Average Initial	b_o	20	$h_{o\text{-measured}}$	11.074
Std Dev Initial	S_{b0}	0	S_{h0}	0.001356466
True initial (after Tx compression)	-	-	h_0	**11.074**
Dimensional coeficients	-	-	C_{h0} (No standard for C_{h0})	1.225E-04
Final	B_f		h6 (centre)	2.074
	-	-	h7 (edge)	2.072
	-	-	h8 (edge)	2.074
	-	-	h9 (edge)	2.074
	-	-	h10 (edge)	2.073
Average Final	-	-	h_f	2.073
Std Dev Final	-	-	S_{hf}	0.000894427
Dimensional coeficients	-	-	C_{hf} =(C_{hf} < 0.04)	0.000

8.12 Homogenisation 3 testpieces geometry

Testpiece Geometry 017				
Dimension	Breadth (mm)		Heigth (mm)	
Initial	b1	20	h1 (centre)	11.082
	b2	20	h2 (edge)	11.079
	b3	20	h3 (edge)	11.078
	-	Note: Cant measure precicely due to paint	h4 (edge)	11.079
	-	-	h5 (edge)	11.079
Average Initial	b_o	20	$h_{o\text{-measured}}$	11.079
Std Dev Initial	S_{b0}	0	S_{h0}	0.001356466
True initial (after Tx compression)	-	-	h_0	**11.079**
Dimensional coeficients	-	-	C_{h0} (No standard for C_{h0})	1.224E-04
Final	B_f		h6 (centre)	2.078
	-	-	h7 (edge)	2.077
	-	-	h8 (edge)	2.077
	-	-	h9 (edge)	2.078
	-	-	h10 (edge)	2.078
Average Final	-	-	h_f	2.078
Std Dev Final	-	-	S_{hf}	0.000547723
Dimensional coeficients	-	-	C_{hf} =(C_{hf} < 0.04)	0.000

Testpiece Geometry 018				
Dimension	Breadth (mm)		Heigth (mm)	
Initial	b1	20	h1 (centre)	11.081
	b2	20	h2 (edge)	11.078
	b3	20	h3 (edge)	11.078
	-	Note: Cant measure precicely due to paint	h4 (edge)	11.08
	-	-	h5 (edge)	11.079
Average Initial	b_o	20	$h_{o\text{-measured}}$	11.079
Std Dev Initial	S_{b0}	0	S_{h0}	0.00116619
True initial (after Tx compression)	-	-	h_0	**11.079**
Dimensional coeficients	-	-	C_{h0} (No standard for C_{h0})	1.053E-04

Final	B_f		h6 (centre)	2.08
	-	-	h7 (edge)	2.081
	-	-	h8 (edge)	2.082
	-	-	h9 (edge)	2.081
	-	-	h10 (edge)	2.081
Average Final	-	-	h_f	2.081
Std Dev Final	-	-	S_{hf}	0.000707107
Dimensional coeficients	-	-	C_{hf} =(C_{hf} < 0.04)	0.000

Testpiece Geometry 019				
Dimension	Breadth (mm)		Heigth (mm)	
Initial	b1	20	h1 (centre)	11.082
	b2	20	h2 (edge)	11.079
	b3	20	h3 (edge)	11.078
	-	Note: Cant measure precicely due to paint	h4 (edge)	11.081
	-	-	h5 (edge)	11.081
Average Initial	b_o	20	$h_{o\text{-measured}}$	11.080
Std Dev Initial	S_{b0}	0	S_{h0}	0.001469694
True initial (after Tx compression)	-	-	h_0	**11.080**
Dimensional coeficients	-	-	C_{h0} (No standard for C_{h0})	1.326E-04
Final	B_f		h6 (centre)	2.082
	-	-	h7 (edge)	2.08
	-	-	h8 (edge)	2.08
	-	-	h9 (edge)	2.08
	-	-	h10 (edge)	2.082
Average Final	-	-	h_f	2.081
Std Dev Final	-	-	S_{hf}	0.001095445
Dimensional coeficients	-	-	C_{hf} =(C_{hf} < 0.04)	0.001